LBL-9706 c.2

Lawrence Berkeley Laboratory
UNIVERSITY OF CALIFORNIA

NUCLEAR REACTIONS PRODUCING ^{2}He AND EXCITED STATES OF ^{4}He AS UNBOUND OUTGOING SYSTEMS

Dieter Paul Stahel
(Ph. D. thesis)

RECEIVED
LAWRENCE
BERKELEY LABORATORY

NOV 16 1979

LIBRARY AND
DOCUMENTS SECTION

September 1979

TWO-WEEK LOAN COPY

This is a Library Circulating Copy
which may be borrowed for two weeks.
For a personal retention copy, call
Tech. Info. Division, Ext. 6782

Prepared for the U.S. Department of Energy under Contract W-7405-ENG-48

LBL-9706 c.2

Table of Contents

Abstract v

I. Introduction. 1

II. Theory. 4

A. Three-Body Kinematics. 4

1. Definitions 4

2. Kinematic relations 5

3. Projected energy spectra. 10

B. Direct-Reaction Theory 14

1. Definition of cross section 14

2. Distorted-wave theory 17

3. Final-state interaction theory. 24

III. Experimental Technique

A. Cyclotron, Beam Transport System, Scatter Chamber. . . 27

B. Targets. 29

1. Solid targets 29

2. Gas targets 30

C. Detection System 30

E. Electronics, Data Acquisition. 34

F. Data Analysis. 38

IV. Experimental Results and Discussion. 42

A. Reactions Producing ^{2}He. 42

1. Characterization of ^{2}He 42

2. Projected energy spectra. 45

3. The (^{3}He,^{2}He) reaction. 49

4. The $(\alpha,{}^{2}He)$ reaction 61

5. The $(d,{}^{2}He)$ reaction 96

B. Reactions Producing ${}^{4}He^{*}$. 113

1. Structure of ${}^{4}He^{*}$ states below 25 MeV. 115

2. The (α,α^{*}) reaction. 116

3. The $({}^{3}He,\alpha^{*})$ reaction. 123

V. Summary and Conclusions 137

Appendix. 140

Acknowledgements. 145

References. 147

NUCLEAR REACTIONS PRODUCING ^{2}He AND EXCITED STATES OF ^{4}He AS UNBOUND OUTGOING SYSTEMS

Dieter Paul Stahel

Lawrence Berkeley Laboratory
University of California
Berkeley, CA 94720

ABSTRACT

A system has been developed to detect the unbound outgoing reaction products ^{2}He ($^1S_0$ state of the pp system) and α^* (excited states of ^{4}He below E_x = 25 MeV) by way of a kinematically complete coincidence measurement of the breakup particles p + p and p + t, respectively.

Projected proton energy spectra from three different reactions producing ^{2}He showed the characteristic enhancement of the cross section over the phase space distribution, which is caused by the final-state interaction between the two protons in the $^1S_0$ state of ^{2}He and is well accounted for by the theory of Watson and Migdal. Energy spectra from the (^{3}He,^{2}He) reaction were taken at $E_{^3He}$ = 60 MeV on targets of ^{6}Li, ^{7}Li, ^{9}Be, ^{12}C, and ^{13}C. Angular distributions were measured for the ^{12}C and ^{13}C targets at $E_{^3He}$ = 50 MeV and were found to be in excellent agreement with exact finite-range (EFR) and zero-range distorted-wave Born-approximation (DWBA) calculations. Energy spectra from the (α,^{2}He) reaction were collected on targets of ^{12}C, ^{13}C, ^{14}N, ^{15}N, ^{16}O, ^{18}O, ^{20}Ne, ^{22}Ne, ^{26}Mg, ^{28}Si, ^{29}Si, ^{32}S, ^{36}Ar, and ^{38}Ar at E_α = 65 MeV and on ^{24}Mg and ^{40}Ca at E_α = 55 MeV. One observed preferential population of 2n states with dominant configurations $(d_{5/2})^2_{4^+}$, $(d_{3/2}f_{7/2})_{5^-}$ and

$(f_{7/2})^2_{6^+}$, many of which were previously unknown. A linear A dependence of the binding energies of the 5^- and 6^+ states was obtained in agreement with the theory of Bansal and French. The $(d,{}^2He)$ reaction was investigated at E_d = 55 MeV. Energy spectra were collected on targets of ^6Li, ^{10}B, and ^{12}C and compared with similar charge-exchange reactions. Angular distributions were measured for the ^{10}B and ^{12}C targets and were found to be in reasonable agreement with microscopic DWBA calculations.

Energy spectra and angular distributions were measured for the (α,α^*) reaction on a target of ^{12}C at E_α = 65 MeV. Projected proton energy spectra showed that only the natural parity, 0^+, state at 20.1 MeV in α^* was populated indicating a direct inelastic scattering process. This was corroborated by the fact that the angular distribution for the transition that left the target nucleus undisturbed was well reproduced by predictions of microscopic DWBA calculations. Energy spectra from the $({}^3He,\alpha^*)$ reaction were collected at $E_{{}^3He}$ = 60 MeV on targets of ^9Be, ^{12}C, and ^{13}C. Projected proton energy spectra indicated that the reaction proceeded through all known α^* states. The energy spectra were compared with those from the $({}^3He,\alpha)$ reaction which was measured concurrently. Both reactions were found to populate the same states in the residual nuclei but with different relative strengths owing to the Q-value dependence of the cross section. Angular distributions from the $({}^3He,\alpha)$ and $({}^3He,\alpha^*(20.1,0^+))$ reactions on ^{13}C at $E_{{}^3He}$ = 50 MeV were analyzed with EFR DWBA to extract spectroscopic information on the $\alpha^*(20.1,0^+)$ state.

I. Introduction

Studies of reactions that produce outgoing particles in unbound states have in the past primarily been focused on processes that form ^{8}Be in its ground state, which is unstable with respect to breakup into two α particles. Although such experiments are somewhat complicated, because they require a coincidence measurement of the two breakup particles, they offer a unique opportunity to investigate processes that cannot easily be studied with reactions that produce stable outgoing particles. For instance, owing to the simple structure and the large α-spectroscopic amplitude of the ^{8}Be g.s., the (α,^{8}Be) reactions has been shown (Wo76) to be an attractive means to study α-pickup processes which are important for the understanding of a α-clustering in nuclei. Furthermore, it has been demonstrated (St77) that the (^{9}Be,^{8}Be) reaction allows one to investigate a heavy-ion induced neutron transfer reaction with a projectile in which the transferred neutron is very loosely bound since ^{9}Be possesses the smallest single-neutron separation energy of all known possible projectiles.

The experimental method used in the detection of ^{8}Be can be extended to the measurement of other unbound particles in states that do not lie too far above the breakup threshold. Two of these candidates have been studied here in detail: ^{2}He and α^* (excited states of ^{4}He below E_x = 25 MeV).

Detection of ^{2}He as an outgoing system via a p-p coincidence measurement has been prompted by the fact that the (α,^{2}He) reaction

might be a potential spectroscopic tool to investigate high-spin 2n states in nuclei, similar to the (α,d) reaction which has long been known to populate preferentially high-spin np-states in the residual nuclei. Such studies are necessary because only a few high-spin 2n-states are known in light nuclei. The reason for this is that the only other light-ion induced 2n-transfer reaction, the (t,p) reaction, mainly populates the low-spin states due to the fact that triton beams are currently limited to energies below about 25 MeV and the Q values are quite positive. Other reaction processes can also be investigated if one succeeds in detecting ^{2}He. Of particular interest is the charge exchange reaction (d,^{2}He) which should complement the (n,p) and (t,^{3}He) reactions. Whereas the latter two reactions are limited in their general application because of difficulties associated with the production of (neutral) neutron and (radioactive) triton beams, no such limitation exists for the (d,^{2}He) reaction since there are no major problems in the acceleration of deuterons to high energies.

Detection of α particles in excited states, all of which are unbound, is possible by way of a coincidence measurement of two of the breakup products p and t, which can be done with the same detection system that is used to observe ^{2}He. Although many reactions producing α^{*} states can be investigated with this technique, the (α,α^{*}) and (^{3}He,α^{*}) reactions are particularly interesting from the point of view of their reaction mechanism as well as their spectroscopic application.

Section II presents some aspects of the three-body kinematics and the direct-reaction theory that are most relevant in the analysis and interpretation of the experimental data. In Sec. III the experimental technique is described and Sec. IV presents the results and discussion of the measurements of the (^{3}He,^{2}He), (α,^{2}He),(d,^{2}He), (α,α^*) and (^{3}He,α^*) reactions.

II. Theory

A. Three-Body Kinematics

1. Definitions

A nuclear reaction induced by a projectile P on a stationary target T producing three final particles 1, 2, and 3 is most conveniently treated with three-body kinematics. If energies and emission angles of particles 1 and 2 are measured in coincidence, as in the experiments discussed here, then sufficient information is obtained to define all the kinematic variables of the reaction. Such experiments are therefore referred to as kinematically complete.

There are several ways in which such a three-body reaction can proceed. The three final particles may be produced simultaneously

$$P + T \rightarrow 1 + 2 + 3 \qquad \text{(II-1)}$$

or the reaction can go through an intermediate unbound state (denoted with an asterisk) which subsequently decays into two particles

$$P + T \rightarrow \left\{ \begin{array}{l} (1 + 2)^* + 3 \\ 1 + (2 + 3)^* \\ (1 + 3)^* + 2 \end{array} \right\} \rightarrow 1 + 2 + 3 \qquad \begin{array}{r} \text{(II-2)} \\ \text{(II-3)} \\ \text{(II-4)} \end{array}$$

All these mechanisms must be considered and in general it is impossible to isolate completely the different contributions to the data. However, it is just an advantage of kinematically complete

experiments that they allow one to select a region of phase space in which one of the above mechanisms dominates. As will be shown below, all experiments discussed here have been designed such that (II-2) accounts for the major part of the cross section. All other reaction paths are then neglected in the following discussion which simplifies considerably the analysis and interpretation of the data.

In order to compare the experimental data, which are measured in the laboratory frame, with theoretical calculations, which are always performed in the center-of-mass (c.m.) system, it is necessary to specify a suitable c.m. system (Oh65). For the case (II-1), the total c.m. system c is appropriate whereas in dealing with mechanisms (II-2) to (II-4) the most suitable c.m. systems are the sequential decay relative coordinate systems c'(i) where i is the first emitted particle (Oh65). Since this work focusses on processes of the type (II-2), the c'(3) is the primary reference system used here.

2. Kinematic relations

From energy and momentum conservation, the following equation relating the lab energies E_1 and E_2 can be derived (Oh65)

$$\frac{1}{m_3}\Big[E_1(m_1+m_3) + E_2(m_2+m_3) - 2(m_P m_1 E_P E_1)^{1/2}\cos\theta_1$$

$$- 2(m_P m_2 E_P E_2)^{1/2}\cos\theta_2 + 2(m_1 m_2 E_1 E_2)^{1/2}\cos\theta_{12}\Big] \qquad \text{(II-5)}$$

$$= Q + E_P\,(1-m_P/m_3)$$

where m, E_p, and Q denote the nuclear mass, projectile lab energy and reaction Q-value, respectively, and

$$\cos\theta_{12} = \cos\theta_1\cos\theta_2 + \sin\theta_1\sin\theta_2\cos(\phi_1-\phi_2) \qquad \text{(II-6)}$$

where θ_{12} is the angle between the directions of particles 1 and 2, and θ_1, ϕ_1, θ_2, and ϕ_2 are spherical polar angles, all defined in the lab system.

It is apparent that an infinite number of combinations of E_1 and E_2 satisfy (II-5), keeping all other variables constant. This is a result of the fact that the recoiling nucleus 3 is unobserved. Each combination of E_1 and E_2 corresponds to a different energy E_3 and emission angle θ_3. Furthermore, the solution of (II-5) is in general double-valued giving rise to two values of E_2 for a given value of E_1 (upper and lower branch). Thus, in the E_1, E_2 space, (II-5) describes a closed curve. (In the $E_1^{1/2}$, $E_2^{1/2}$ space it is an ellipse). Such a curve is called a kinematic locus.

As an example which is typical for the reactions discussed here, Fig. II-1 shows a two-dimensional spectrum of E_{p_1} vs. E_{p_2} from the reaction 65 MeV $\alpha + {}^{12}C \rightarrow p + p + {}^{14}C$ in which the two protons were measured at $\theta_1 = \theta_2 = 15.8^o$ and $\Delta\phi = \phi_1-\phi_2 = 37.4^o$ ($\theta_{12} = 10^o$). (Sec. III will give the experimental details of such measurements.) The solid curves represent the kinematic loci for the reactions leaving the unobserved ${}^{14}C$ nucleus in its ground state (g.s.), 6.73-MeV and 10.72-MeV states and were calculated with the three-body kinematics program of Ohlsen (Oh65).

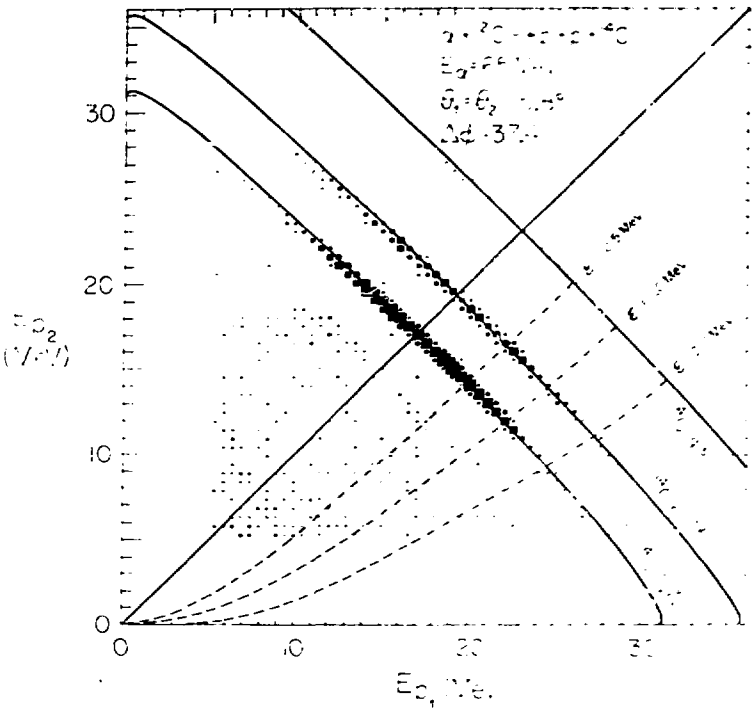

Fig. II-1. Two-dimensional proton energy spectrum from the $^{12}C(\alpha,pp)^{14}C$ reaction at E_α = 65 MeV. See text.

As can be seen, for this reaction (II-5) is single valued except near the maximum values of E_1 and E_2 because $m_1+m_2 \ll m_3$ and the incident energy is high, as is true for all other reactions investigated here. Within the experimentally observable region, however, the lower branch of the kinematical solution does not exist and will therefore not be considered here.

Any structure on these kinematic loci can be associated with intermediate states formed in the reaction. In order to identify these states, it is useful to calculate for each point of a kinematic locus the relative energies E_{1-2}, E_{2-3}, and E_{1-3}, which can be related to the excitation energies of the intermediate states $(1+2)^*$, $(2+3)^*$, and $(1+3)^*$ above the threshold for breakup into the particles 1 and 2, 2 and 3, and 1 and 3, respectively. The relative energy E_{1-2}, which will subsequently be denoted by ε, can readily be derived from a velocity vector diagram and is given by

$$\varepsilon = \frac{1}{m_1+m_2}\left(m_2E_1 + m_1E_2 - 2(m_1m_2E_1E_2)^{1/2}\cos\theta_{12}\right) \quad . \qquad \text{(II-7)}$$

According to this equation, a small value of ε is associated with a small angle θ_{12}. Since the present experiments deal with reactions that form an intermediate system $(1+2)^*$ in a resonance or resonance-like state near threshold and therefore require the detection of particles 1 and 2 with small relative energies, the angle θ_{12}, which corresponds to the angular separation between the two counters, was chosen to be small. Under these conditions, the relative energies

E_{2-3} and E_{1-3} and thus the excitation energies of the respective intermediate systems are large because particle 3 is emitted in the c.m. system in the opposite direction from particles 1 and 2. Since only rarely are there strong resonances at these high excitation energies, the cross section for the production of such intermediate states is normally negligibly small. Therefore, the structure on the kinematic loci observed in these reactions can entirely be associated with intermediate states of the $(1+2)^*$ system. The dashed lines in Fig. II-1 represent all points of E_{p_1} and E_{p_2} for which ϵ has a constant value. They were calculated for ϵ = 0.5, 1.0, and 2.0 MeV and are shown only on one side of the diagonal line $E_{p_1} = E_{p_2}$, since for the special case of $m_1 = m_2$ and $\theta_1 = \theta_2$ the spectrum is symmetrical about this line. This means that on a given locus there are two points for a given value of , one with $E_{p_1} < E_{p_2}$ and another one with $E_{p_1} > E_{p_2}$. It is important to note that these two cases correspond to two different types of events. For this particular reaction and detector setup they represent events in which $(1+2)^*$ is emitted below and above the horizontal reaction plane, respectively, with the same energy. However, in the more general case of $\theta_1 \neq \theta_2$ and/or $m_1 \neq m_2$, both energy and angle at which $(1+2)^*$ emerges differ for the two cases. In the present experiments, these differences are quite small and, therefore, neglected.

Whereas for a given locus the lower limit to ε is a function of θ_{12}, the upper one is determined in these experiments by the energy cut-offs of the counters. As can be seen in Fig. II-1, for the ^{14}C g.s. and 6.73-MeV state it is the upper cut-off, whereas for the 10.72-MeV state it is the lower cut-off that determines the maximum observable value of ε.

3. Projected energy spectra

In analyzing data obtained from a kinematically complete measurement of a three-body reaction and shown in the most general form as a two-dimensional spectrum (Fig. II-1), it is convenient to generate one-dimensional spectra by projecting i) a given kinematic locus onto the E_1 axis and ii) the entire two-dimensional spectrum onto the line $E_1 = E_2$.

A projected energy spectrum $d^3\sigma/d\Omega_1\, d\Omega_2 dE_1$ of a given kinematic locus onto the E_1 axis is useful in determining what intermediate stated a reaction goes through because it exhibits the structure of the kinematic locus more clearly than the two-dimensional spectrum. Figure II-2a shows such a projection of the locus corresponding to the ^{14}C, 10.72-MeV state in Fig. II-1. Note that the inserted ε-scale is non-linear as a function of E_{p_1}. As will be shown in Sec. IV.A.2, the structure of this spectrum can be associated with a definite state in the intermediate $(1+2)^*$ system, namely the $^1S_0$ state of ^2He.

In order to compare such projected spectra with theoretical calculations it is necessary to convert the lab cross sections to the c.m.

system in which the calculations are performed, or alternatively to convert the theoretical cross sections to the lab system, as is sometimes done. Since in the present experiments one assumes that the reactions proceed through some intermediate state $(1+2)^*$, the appropriate c.m. system is the sequential decay system c'(3). The relation between the lab and the c'(3) coordinate system can be found from the theory of Jacobian coordinate transformations and is given by

$$\frac{d^3\sigma}{d\Omega_1 d\Omega_2 dE_1} = J_{12}\,\frac{d^3\sigma}{d\Omega_{3-12}\,d\Omega_{1-2}\,dE} \qquad \text{(II-8)}$$

where the Jacobian J_{12} is given by (Bu72, Ja76c, Oh65)

$$J_{12} = \frac{\partial(\Omega_{3-12},\Omega_{1-2},E)}{\partial(\Omega_1,\Omega_2,E_1)} = \frac{1}{p_{3-12}p_{3-12}p_{1-2}p_{1-2}}\;\frac{m_1 m_2 m_3 p_1 p_2}{\left|\,m_2+m_3+\dfrac{m_2(\vec{p}_1-\vec{p})\vec{p}_2}{\vec{p}_2}\,\right|}\,. \qquad \text{(II-9)}$$

These projected energy spectra not only help identify intermediate states, but also allow one to extract the c.m. cross section $d\sigma/d\Omega_{3-12}$ for the production of $(1+2)^*$. If particles 1 and 2 are in a relative S-state, then the distribution of the breakup products is isotropic in their own c.m. system and (II-8) can be integrated over $d\Omega_{1-2}$ and one obtains

$$\frac{d^2\sigma}{d\Omega_{3-12}\,dE} = \frac{4\pi}{J_{12}}\,\frac{d^3\sigma}{d\Omega_1 d\Omega_2 dE_1}\,. \qquad \text{(II-10)}$$

Integration over $d\varepsilon$ then yields the c.m. differential cross section for relative enegies between ε_ℓ and ε_u

$$\frac{d\sigma}{d\Omega_{3-12}} = \int_{\varepsilon_\ell}^{\varepsilon_u} \frac{4\pi}{J_{12}} \left(\frac{d^3\sigma}{d\Omega_1 d\Omega_2 dE_1}\right) d\varepsilon \qquad \text{(II-11)}$$

An appropriate choice of ε_ℓ and ε_u must be made. If the intermediate state is a narrow Breit-Wigner type resonance state (e.g., ^{8}Be g.s.), the integration limits should contain the entire peak. If, however, the state is so broad that only part of it is included in the data, given the experimental limits to the observable relative energies, then ε_ℓ and ε_u must be chosen accordingly and specified explicitly. Integration of a projected energy spectrum, as the one shown in Fig. II-2a, should extend over only half of it since the two parts of the spectrum correspond to two different types of events as discussed in the previous section. Furthermore, the resulting cross section $d\sigma/d\Omega_{3-12}$ must be divided by 2 if particles 1 and 2 are identical in order to correct for double counting of coincidence events which results from the indistinguishability of the two particles.

Whereas spectra projected onto the E_1 axis can indicate what intermediate state a given reaction goes through, spectra generated by projecting the entire two-dimensional spectrum onto the line $E_1 = E_2$ allow one to determine what states are populated in the residual nucleus. (It is assumed here that neither particle 1 nor particle 2 possess excited states). Figure II-2b displays such a

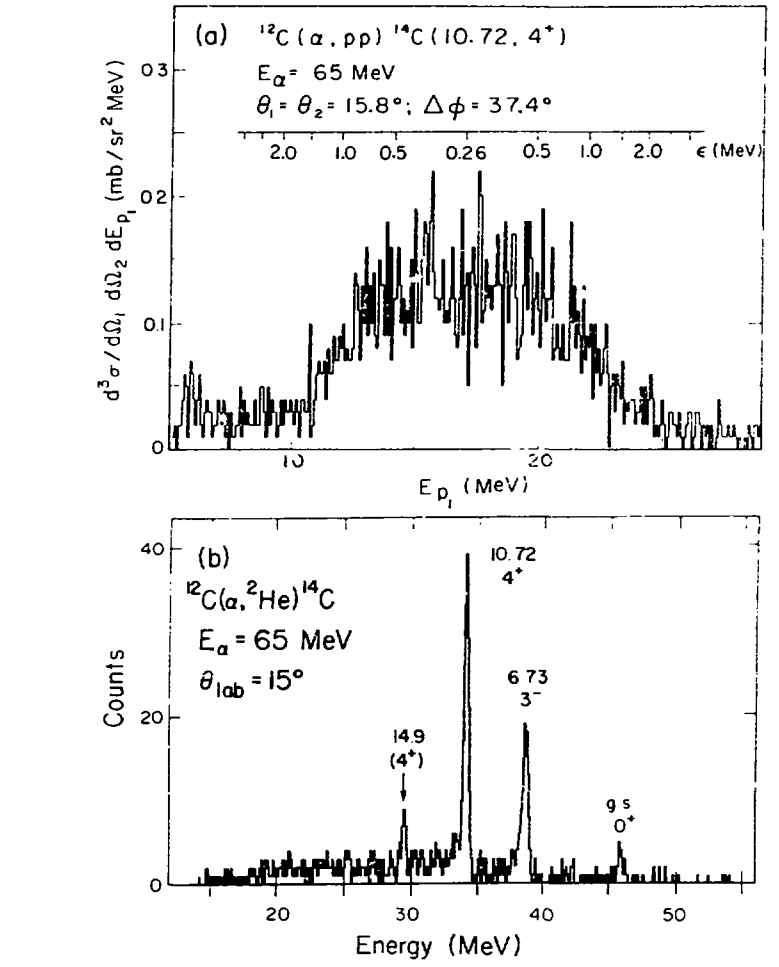

Fig. II-2. Energy spectra from the $^{12}C(\alpha,pp)^{14}C$ reaction at E_α = 65 MeV obtained by a) projecting the kinematic locus of the 10.72-MeV,4^+ state in ^{14}C onto the E_{p1}-axis and b) projecting the entire two-dimensional spectrum (Fig. II-1) onto the line $E_{p_1} = E_{p_2}$.

projected spectrum $d^3\sigma/d\Omega_1 d\Omega_2 d(E_1+E_2)$ obtained from the data shown in Fig. II-1. Since the reactions investigated here proceed through a definite intermediate state in the $(1+2)^*$ system, such projected energy spectra will be referred to in a way common for two-body reactions, in this particular case as "^{2}He energy spectrum from the $^{12}C(\alpha,{}^2He)^{14}C$ reaction". The width of the peaks observed in these spectra is hardly affected by the curvature of the kinematic loci, since the latter are almost straight lines in these reactions; (the width is primarily a result of the kinematic broadening introduced by the finite size of the counter solid angles, as noted below).

B. Direct-Reaction Theory

1. Definition of cross section

Every nuclear reaction represents a transition of a given system from an initial to a final state. According to Fermi's Golden Rule No. 2, the quantum mechanical expression for the transition probability per unit time for such a change of a system is given by

$$W_{fi} = \frac{2\pi}{\hbar}|T_{fi}|^2 \rho \qquad \text{(II-12)}$$

where $T_{fi} = \langle f|V|i\rangle$ is the matrix element of the perturbation operator V that causes the transition and ρ is the (momentum) phase space factor which represents the number of final states per energy interval.

In reaction theory it is more customary instead of dealing with transition probabilities W_{fi} to define the concept of the reaction

cross section as a ratio of the transition probability to the incident particle current density

$$j_i = \hbar k_i/\mu_i = v_i \quad , \tag{II-13}$$

$$d\sigma = W_{fi}/v_i \quad . \tag{II-14}$$

Substitution of (II-12) into (II-14) yields then the central formula for the differential cross section

$$d\sigma = \frac{2\pi}{\hbar}\frac{\mu_i}{p_i}\,|T_{fi}|^2\,\rho \tag{II-15}$$

If a reaction produces only two final particles (P+T → 1+2), the phase space factor ρ in the c.m. system is given by

$$\rho = \frac{d\vec{p}_f}{dE_f(2\pi\hbar)^3} = p_f\mu_f d\Omega_f/(2\pi\hbar)^3 \tag{II-16}$$

and one obtains for the differential cross section

$$\frac{d\sigma}{d\Omega_f} = \frac{\mu_i\mu_f}{(2\pi\hbar^2)^2}\frac{k_f}{k_i}\,|T_{fi}^{(2)}|^2 \quad . \tag{II-17}$$

The superscript in the transition matrix element denotes the fact that T_{fi} is calculated for only two final particles.

For reactions in which three final particles are produced by way of an intermediate state $(P+T \rightarrow (1+2)^{*}+3 \rightarrow 1+2+3)$ the phase space factor in the c'(3) system is given by

$$= \frac{d\vec{p}_{3-12}\, d\vec{p}_{1-2}}{dE_{3-12}\,(2\pi\hbar)^6}$$

$$= (p_{3-12}\mu_{3-12}p_{1-2}\mu_{1-2}d\Omega_{3-12}d\Omega_{1-2}d\varepsilon)/(2\pi\hbar)^6 \quad . \qquad \text{(II-18)}$$

By substituting (II-18) in (II-15) one obtains for the triple differential cross section

$$\frac{d^3\sigma}{d\Omega_{3-12}d\Omega_{1-2}d\varepsilon} = \frac{\mu_i\mu_{3-12}}{(2\pi\hbar^2)^2}\,\frac{k_{3-12}}{k_i}\,|T^{(3)}_{fi}|^2\,\frac{\mu_{1-2}p_{1-2}}{(2\pi\hbar)^3} \qquad \text{(II-19)}$$

where $T^{(3)}_{fi}$ is computed for three final particles.

If particles 1 and 2 possess no relative angular momentum then (II-19) can be integrated over $d\Omega_{1-2}$:

$$\frac{d^2\sigma}{d\Omega_{3-12}d\varepsilon} = 4\pi\,\frac{\mu_i\mu_{3-12}}{(2\pi\hbar^2)^2}\,\frac{k_{3-12}}{k_i}\,|T^{(3)}_{fi}|^2\,\frac{\mu_{1-2}p_{1-2}}{(2\pi\hbar)^3} \quad . \qquad \text{(II-20)}$$

Furthermore, integration over $d\varepsilon$ yields

$$\frac{d\sigma}{d\Omega_{3-12}} = \int_{\varepsilon_\ell}^{\varepsilon_u} 4\pi\,\frac{\mu_i\mu_{3-12}}{(2\pi\hbar^2)^2}\,\frac{k_{3-12}}{k_i}\,|T^{(3)}_{fi}|^2\,\frac{\mu_{1-2}p_{1-2}}{(2\pi\hbar)^3}d\varepsilon \qquad \text{(II-21)}$$

where the integration limits should be chosen consistent with those used in calculating the experimental cross section (II-11).

Evaluation of (II-20) and (II-21) requires a computation of the matrix element $T_{fi}^{(3)}$. Since such calculations are quite complicated and cannot be handled by standard reaction models, one is forced to resort to some approximations. In the simplest approximation, $d\sigma/d\Omega_{3-12}$ is set equal to the two-body cross section (II-17) under the assumption that $(1+2)^*$ is bound or at least much longer lived than the typical reaction time for a two-body reaction, which is of the order of 10^{-21} s. It is then possible to employ standard two-body reaction models, such as the distorted-wave method which will be discussed in Sec. 2 The approximations used to interpret the relative energy spectra $d^2\sigma/d\Omega_{3-12}d\varepsilon$ are the subject of the final-state interaction theory and will be presented in Sec. 3.

2. Distorted-wave theory

The standard method of calculating the differential cross section $d\sigma/d\Omega_f$ (II-17) of a direct two-body reaction is the distorted-wave Born-approximation (DWBA). Since this theory has been discussed extensively by Austern (Au70) and Jackson (Ja70), only the most relevant formulas and aspects will be presented here.

In the DWBA theory the transition amplitude for the reaction A(a,b)B with spins J_A, J_B, s_a, and s_b is given by

$$T_{fi} \propto \int d\vec{r}_i \int d\vec{r}_f \chi_f^{(-)*}(\vec{k}_f,\vec{r}_f)\langle B,b|V|A,a\rangle \chi_i^{(+)}(\vec{k}_i,\vec{r}_i) \quad . \qquad \text{(II-22)}$$

The wave functions $\chi_i^{(+)}$ and $\chi_f^{(-)}$ describe the relative motion of the pairs A,a and B,b, respectively, in the presence of distorting effects arising from the Coulomb and nuclear interactions. These distorted waves are in practice generated from an optical model potential (usually of Woods-Saxon form) that describes the elastic scattering in the appropriate channel.

The matrix element $\langle B,b|V|A,a\rangle$ is called the form factor and represents an integral over all coordinates that do not depend on the reaction coordinates $\vec{r}_i$ and $\vec{r}_f$. It plays the role of an effective interaction responsible for the transition between the scattering states $\chi_i^{(+)}$ and $\chi_f^{(-)}$ and contains all the nuclear structure information.

Since the calculation of the form factor, and hence the DWBA cross section depends on the type of reaction, the transfer and inelastic scattering reactions investigated in this work will be discussed separately.

a. Transfer reactions

For a stripping reaction A(a,b)B with B=A+x and a=b+x, where x is the transferred nucleon (or cluster of nucleons) the form factor is given by

$$\langle B,b|V|A,a\rangle = \langle \Psi_B\Phi_b|V_a|\Psi_A\Phi_a\rangle \qquad \text{(II-23)}$$

where V_a represents the effective interaction, here in the "post" approximation (Au70) taken to be the interaction between b and x. In

order to evaluate (II-23) it is convenient to use the fractional-parentage expansion (Ma 60)

$$\Psi_B(J_B T_B) = \sum_{A'} \langle J_B T_B \{| J_{A'} T_{A'}, j \rangle \Psi_{A'}(J_{A'} T_{A'}) \phi_B(j) \qquad \text{(II-24)}$$

and

$$\phi_a(s_a t_a) = \sum_{b'} \langle s_a t_a \{| s_{b'} t_{b'}, s \rangle \phi_{b'}(s_{b'} t_{b'}) \phi_a(s) \qquad \text{(II-25)}$$

where the expression in brackets represents a coefficient of fractional parentage (c.f.p.). Integration of (II-23) over all target and projectile core coordinates then yields

$$\langle B, b | V | A, a \rangle = C_B S_B^{1/2} C_a S_a^{1/2} \psi_B^*(\vec{r}_{Ax}) V_a(\vec{r}_{bx}) \psi_a(\vec{r}_{bx}) \quad . \qquad \text{(II-26)}$$

The (normalized) wave functions ψ_B and ψ_a are called bound state wave functions and describe the motion of the transferred nucleon x in B and a, respectively. They are usually approximated by shell-model eigenfunctions of a Woods-Saxon well with an eigenvalue equal to the nucleon separation energy. S denote the spectroscopic factors which are defined as (Fr60, Ma60)

$$S_B = n_B \langle J_B T_B \{| J_A T_A, j \rangle^2 \qquad \text{(II-27)}$$

and

$$S_a = n_a \langle s_a t_a \{| s_b t_b, s\rangle^2 \tag{II-28}$$

where n is the number of equivalent active nucleons. The factors C in (II-26) are isospin coupling Clebsch-Gordan coefficients.

Using (II-22) and (II-26) one finds for the transition matrix element

$$T_{fi} \propto C_B S_B^{1/2} C_a S_a^{1/2} \int d\vec{r}_i \int d\vec{r}_f \chi_f^{(-)*}(\vec{k}_f, \vec{r}_f) \psi_B^*(\vec{r}_{Ax})$$

$$\times V_a(\vec{r}_{bx}) \psi_a(\vec{r}_{bx}) \chi_i^{(+)}(\vec{k}_i, \vec{r}_i) \quad . \tag{II-29}$$

Computations that carry out this six-dimensional integration are referred to as exact finite-range (EFR) calculations (Au64, De73). Since such calculations require a great deal of computer time, it is often desirable to introduce the zero-range (ZR) approximation by replacing the radial dependence of the interaction potential V_a by a δ-function

$$V_a(\vec{r}_{bx}) \psi_a(\vec{r}_{bx}) = D_0 \delta(\vec{r}_{bx}) \tag{II-30}$$

where

$$D_0 = \int d\vec{r}_{bx} \; V_a(\vec{r}_{bx}) \psi_a(\vec{r}_{bx}) \tag{II-31}$$

which reduces the six-dimensional integral (II-29) to a three-dimensional one

$$T_{fi} \propto C_B S_B^{1/2} C_a S_a^{1/2} D_0 \int d\vec{r}\, \chi_f^{(-)*}(\tfrac{A}{B}\vec{r})\psi_B^*(\vec{r})\chi_i^{(+)}(\vec{r}) \qquad \text{(II-32)}$$

and facilitates the computations considerably. The ZR approximation is most appropriate for light-ion ($a \leq 4$) induced reactions. However, in these cases, the projectile wave function is sometimes treated slightly differently from that of the target. Instead of using the general c.f.p. expansion (II-25), the wave functions of a and b are factored into a spin and space part and only the spin part is expanded in terms of c.f.p.'s. Integration over the internal space coordinates $\vec{\rho}$ is then explicitly carried out using realistic wave functions. Thus, in (II-26), $\psi_a(\vec{r}_{bx})$ is replaced by

$$\psi_a(\vec{r}_{bx}) = \int d\vec{\rho}\, \phi_b^*(\vec{\rho})\phi_a(\vec{r}_{bx},\vec{\rho}) \qquad \text{(II-33)}$$

which is an (unnormalized) single-particle radial wave function, and S_a is calculated with a spin c.f.p. (Fr60).

In evaluating the transition matrix element the interaction is expanded into a series of multipoles, each of which corresponds to the transfer of a definite total angular momentum j, which is composed of a orbital part ℓ and a spin part s and is restricted by the selection rules

$$\vec{j} = \vec{J}_B - \vec{J}_A, \quad \vec{s} = \vec{s}_a - \vec{s}_b, \quad \vec{j} = \vec{\ell} + \vec{s} \quad . \qquad \text{(II-34)}$$

In ZR, but not EFR calculations, the parity change $\Delta\pi = \pi(a)\pi(A)\pi(b)\pi(B)$

where $\pi(i)$ denotes the internal parity of particle i, restricts the possible ℓ values according to $\pi=(-1)^{\ell}$. Contributions from different multipoles are added up incoherently if no spin-orbit interaction is included in the calculation of the distorted waves. Otherwise, only the sum over the different j values is incoherent.

All the DWBA analyses of transfer reactions were performed in this work using the EFR DWBA program LOLA (De73) and the ZR DWBA program DWUCK4 (Ku74). The following gives a summary of the relationships between the experimental cross section and the cross section calculated by these two programs for stripping as well as for pickup reactions.

<u>EFR program LOLA</u>

-stripping reaction A(a,b)B

$$\frac{d\sigma^{\ell}}{d\Omega} = \frac{2J_B+1}{2J_A+1}\, C_B^2 S_B C_a^2 S_a (2\ell+1) W^2 \sigma^{\ell}_{LOLA} \qquad \text{(II-35)}$$

-pickup reaction B(b,a)A

$$\frac{d\sigma^{\ell}}{d\Omega} = \frac{2s_a+1}{2s_b+1}\, C_B^2 S_b C_a^2 S_a (2\ell+1) W^2 \sigma^{\ell}_{LOLA} \qquad \text{(II-36)}$$

<u>ZR program DWUCK4</u>

-stripping reaction A(a,b)B

$$\frac{d\sigma^{\ell}}{d\Omega} = \frac{2J_B+1}{2J_A+1}\, C_B^2 S_B C_a^2 S_a \frac{D_0^2}{10^4} \frac{\sigma^{\ell}_{DWUCK4}}{2j+1} \qquad \text{(II-37)}$$

$$= N \frac{2J_B+1}{2J_A+1} C_B^2 S_B \frac{\sigma^{\ell}_{DWUCK4}}{2j+1}$$

$$N = C_a^2 S_a \frac{D_0^2}{10^4} \tag{II-38}$$

-pickup reaction B(b,a)A

$$\frac{d\sigma}{d\Omega} = \frac{2s_a+1}{2s_b+1} C_B^2 S_B C_a^2 S_a \frac{D_0^2}{10^4} \frac{\sigma^{\ell}_{DWUCK4}}{2j+1} \tag{II-39}$$

$$= N C_B^2 S_B \frac{\sigma^{\ell}_{DWUCK4}}{2j+1}$$

$$N = \frac{2s_a+1}{2s_b+1} C_a^2 S_a \frac{D_0^2}{10^4} \tag{II-40}$$

b. Inelastic scattering

Since in inelastic scattering, which includes charge-exchange scattering, there is no change in the mass number of the projectile, the channel displacement variables become identical ($\vec{r}_i=\vec{r}_f=\vec{r}$) and the transition matrix element reduces to the ZR form

$$T_{fi} \propto \int d\vec{r}\, \chi_f^{(-)*}(\vec{k}_f,\vec{r}) \langle \psi_B \phi_b | V | \psi_A \phi_a \rangle \chi_i^{(+)}(\vec{k}_i,\vec{r}) \tag{II-41}$$

where the effective interaction V in th microscopic description of inelastic scattering is given by (Ma66, Au70, Ma75)

$$V = \sum_{i=1}^{A} v_{0i}(\vec{r}_{0i},\vec{\sigma}_0,\vec{\tau}_i,\vec{\tau}_0,\vec{\tau}_i) \tag{II-42}$$

The two-body interaction v_{0i} between a projectile nucleon and a target nucleon i is usually taken to be a product of a shape function $g(r_{0i})$ and a linear combination of exchange operators:

$$v_{0i} = -\left[V_{00} + V_{01}(\vec{\tau}_0 \cdot \vec{\tau}_i) + V_{10}(\vec{\sigma}_0 \cdot \vec{\sigma}_i) + V_{11}(\vec{\sigma}_0 \cdot \vec{\sigma}_i)(\vec{\tau}_0 \cdot \vec{\tau}_i)\right] g(r_{0i}) \quad \text{(II-43)}$$

It is most convenient to express the spectroscopic amplitudes $S(JJ_iJ_f;TT_iT_f;j_1j_2)$ in terms of a reduced matrix element of the operator A_{JT} for the destruction of a nucleon with spin j_1 and a creation of a nucleon with spin j_2 by

$$S(JJ_iJ_f;TT_iT_f;j_1j_2) = \frac{1}{(2J+1)^{1/2}(2T+1)^{1/2}} \langle \Psi_B(J_fT_f) \| A_{JT} \| \Psi_A(J_iT_i) \rangle \quad \text{(II-44)}$$

In the calculation of the DWBA cross section, the contributions from the different interactions in (II-43) along with all the possible spectroscopic amplitudes are added up. If the projectile is a composite nucleus, the interaction strength must be modified to account for the finite size of the projectile (Ma66). The calculated cross section can then directly be compared with the experimental data.

3. Final-state interaction theory

Theoretical prediction of the shapes of the projected energy spectra $d^2\sigma/d\Omega_{3-12}dE$ is usually done within the framework of the final-state interaction (FSI) theories (Gi64, Sl71). If there is a strong interaction between the final particles 1 and 2, but only a weak one between these two particles and the third one then the transition matrix element may be factored as follows

$$|T_{fi}^{(3)}|^2 \approx |T_{fi}^{(3')}|^2 F(k_{1-2}) \tag{II-45}$$

where $T_{fi}^{(3')}$ is the matrix element for the production of three (uncorrelated) final particles and $F(k_{1-2})$ is an enhancement function arising from the FSI between particles 1 and 2. In this approximation, (II-20) can be written as

$$\frac{d^2\sigma}{d\vec{k}_{3-12}d\varepsilon} \propto k_{1-2}k_{3-12}|T_{fi}^{(3')}|^2 F(k_{1-2}) \tag{II-46}$$

Assuming that $k_{3-12}|T_{fi}^{(3')}|^2$ is constant, one finds after conversion to the lab system

$$\frac{d^3\sigma}{d\vec{k}_1 d\vec{k}_2 dE_1} \propto J_{12}k_{1-2}F(k_{1-2}) \quad . \tag{II-47}$$

In the absence of a FSI between particles 1 and 2, $F(k_{1-2}) = 1$ and (II-47) reduces to a simple phase space distribution.

The enhancement function $F(k_{1-2})$ can be obtained from the Jost function theory (Gi64). A calculation of the appropriate Jost function is in some cases very difficult, (e.g., in the presence of the Coulomb interaction,) and $F(k_{1-2})$ is approximated by

$$F(k_{1-2}) \approx |\phi(k_{1-2}, r=b)|^2 \tag{II-48}$$

where $\phi(k_{1-2}, r)$ is a scattering wave function and as such the solution of the radial Schrödinger equation for the motion of two

mutually interacting particles, and b is the boundary radius between the inner and outer wave functions. For particles with no relative angular momentum, the outer wave function that includes Coulomb interaction is given by

$$\phi(k_{1-2},r) = \frac{e^{-i\delta_0}\left[F_0(k_{1-2},r)\cos\delta_0 + G_0(k_{1-2},r)\sin\delta_0\right]}{k_{1-2}r} \qquad \text{(II-49)}$$

where F_0 and G_0 are the regular and irregular Coulomb wave functions, and δ_0 the nuclear S-wave phase shift in the presence of the Coulomb interaction.

Although $|\phi(k_{1-2},b)|^2$ gives a reasonable k_{1-2} dependence of the FSI effects, it is not a true enhancement function because it does not go to unity for large values of k_{1-2}.

III. Experimental Technique

A. Cyclotron, Beam Transport System, Scatter Chamber

All experiments discussed here have been performed using various beams from the variable energy, azimuthally-varying field, spiralridge sector focused 86-inch cyclotron. This machine is capable of accelerating positive ions with mass A (amu) and charge state q to a maximum kinetic energy $E_{max} = 140q^2/A$ (MeV), except for protons and $^3He^{2+}$, for which E_{max} = 55 and 170 MeV, respectively. The experiments were carried out using the external beam facilities of Cave 2 as shown in Fig. III-1. Beam extracted from the cyclotron by an electrostatic deflector was first defined by a 2.54 cm wide horizontal collimator, then radially focused with a quadrupole doublet, deflected by 39.5° with a switching dipole magnet and radially focused again. The beam then passed through a 1.5 mm wide vertical energy analyzing slit and was focused with two quadrupole doublets onto the target. Typical beam spot sizes of about 2×2 mm^2 were obtained. Energy resolution of the beam defined by the switching magnet and analyzing slit was about 0.14%.

The scatter chamber measured 51 cm in diameter and was kept at a pressure of about 2×10^{-5} Torr by a turbomolecular pump which was equipped with a liquid nitrogen cooled trap to reduce contamination of the vacuum with pump oil. The detectors were mounted on a remotely moveable platform and partially enclosed in a shielding made from tantalum and aluminum. Strong permanent magnets were placed in front of the detector telescopes to deflect electrons that were knocked out

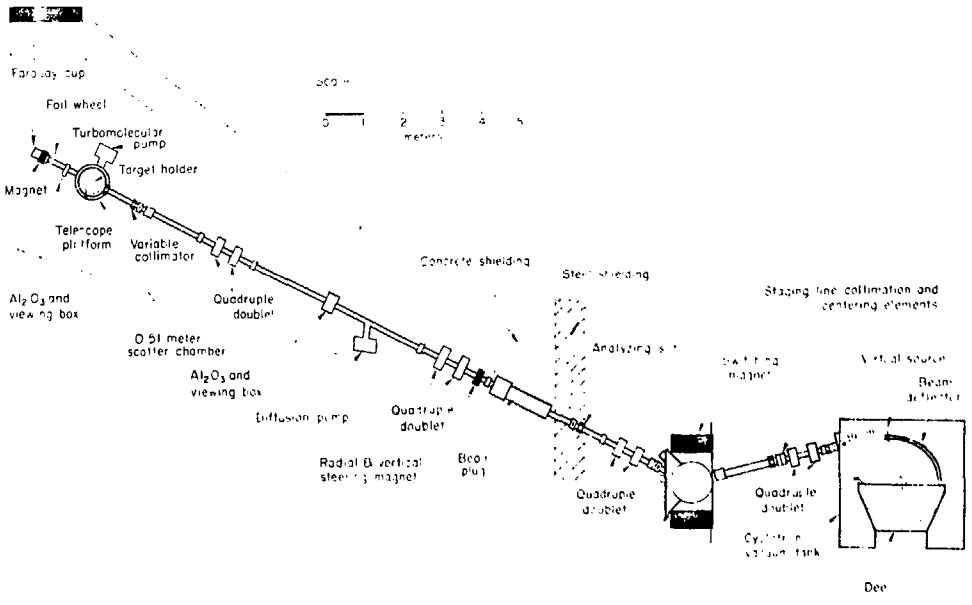

Fig. III-1. Cyclotron and beam transport system to the 0.51 m scatter chamber in Cave 2.

of the targets. In the center of the scatter chamber, a target ladder was located which was capable of holding seven solid targets and could be remotely lowered, raised and rotated.

B. Targets

Since a great variety of solid and gaseous targets was utilized, their exact composition will be quoted in the section that discusses the results of the experiments.

1. Solid targets

Foils of the target material, typically a few hundred $\mu g/cm^2$ thick and with an area of about 2 cm^2, were mounted on 4.45×3.81 cm^2 target holders. Targets that oxydized easily were kept under vacuum; before an experiment they were put into the scatter chamber which had been let up to atmospheric pressure with argon. Target thicknesses were determined after an experiment from a measurement of the energy loss of 8.78 and 6.06 MeV α particles (from a $^{212}Po/^{212}Bi$ α-source) passing through the targets. Thicknesses obtained in this way are estimated to be accurate to about $\pm 10\%$.

When targets with a low melting point were used, it was necessary to continuously check for possible evaporation of target material. This was done by employing a monitor counter which was mounted at a fixed angle in the scatter chamber and which allowed one to measure the number of counts in the elastic scattering peak per μC of beam particles.

2. Gas targets

A cylindrical gas cell with a radius of 3.18 cm and a height of 3.5 cm was utilized in these experiments along with a recovery system that permitted gas recycling when rare isotopes were used. The window of the gas cell consisted of a 2.5 μm thick foil made from Havar (46% Co, 21% Cr, 19% Fe, 14% Ni) and subtended continuously about 300°. In order to define the target thickness, a 3 mm wide collimating slit was placed between the gas cell and the front collimator of the detection system at a distance of 3.88 cm from the center of the gas cell. Typical cell pressures were about 0.25 atm.

C. Detection System

In designing the geometry of a detection system for a kinematically complete measurement of the two breakup products from the decay of an unbound particle, four main factors have to be considered: 1. range of relative energies to be detected, 2. energy resolution, 3. true coincidence rate and 4. ratio of true to random coincidences.

As for factor 1, it was pointed out in Sec. II.A.2 that the minimum relative energy that can be observed depends on θ_{12}, the angular separation between the two counters. Since in the present experiments small relative energies are to be measured, the counters were separated by a distance of only 1 cm. Factors 2 to 4 cannot be independently optimized. On the one hand, energy resolution mandates small solid angles $d\Omega_1$ and $d\Omega_2$, but on the other hand big solid angles are necessary in order to achieve large values for both the true coincidence rate and the ratio of true to random coincidences,

since both of them are approximately proportional to $d\Omega_1$ for a given singles count rate and $d\Omega_1 = d\Omega_2$.

A good compromise between these factors has been obtained in the design of a detection system that is shown schematically in Fig. III-2 for the detection of ^{2}He. It consists of two identical ΔE-E counter telescopes arranged symmetrically above and below the horizontal reaction plane. Not shown are the E_{rej} counters which were placed behind each E counter to reject events that traversed the ΔE-E system.

Three different geometries have been utilized and are summarized in Table III-1. Geometry A possesses the largest solid angle and thus good coincidence efficiency, but its horizontal acceptance angle is 4.2° which gives rise to kinematic broadening of the peaks observed in the energy spectra. This effect provides the main component determining the energy resolution which was observed to be between about 400 and 500 keV full width at half maximum (FWHM) depending on the type of reaction. In order to improve the resolution, in some experiments the widths of the collimators were somewhat reduced (geometry B). However, in both geometries, A and B, the angle θ_{12} is rather ill defined ($5^{\circ} < \theta_{12} < 15^{\circ}$) because of the large height of the collimators. Since in three-body kinematics calculations a knowledge of θ_{12} is necessary, an average value was taken for θ_{12} and thus also for θ_1, ϕ_1, θ_2, and ϕ_2 by using the angles associated with the center of each collimator. In some experiments, the heights of both collimator were substantially reduced

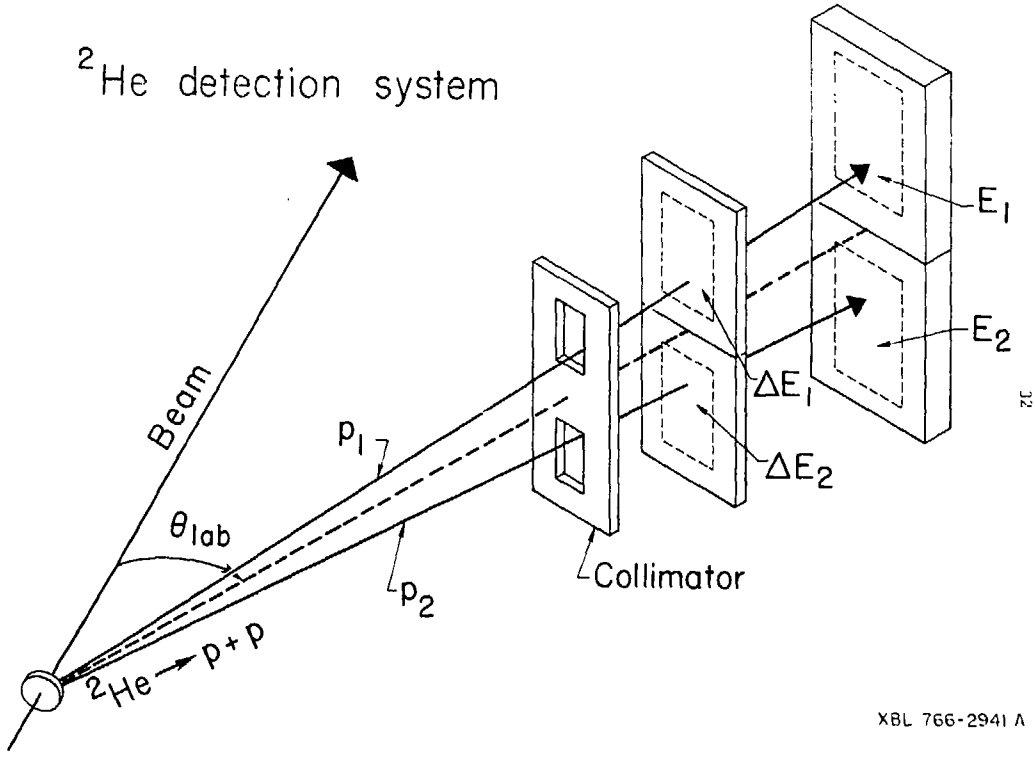

Fig. III-2. Schematic diagram of the ^{2}He detection system.

Table III-1. Detection system geometries.

	Collimator					Distance	
	Telescope 1		Telescope 2			from	Ave
	Width (cm)	Height (cm)	Width (cm)	Height (cm)	Separation (cm)	target (cm)	θ_{12} (deg)
A	0.8	1.0	0.8	1.0	1.0	11.0	10.4
B	0.6	1.0	0.6	1.0	1.0	11.0	10.4
C	0.6	0.085	0.6	0.085	1.0	11.0	5.6

(geometry C), which significantly decreased the efficiency, but resulted in a smaller and better defined average value of θ_{12}.

D. Counters

In these experiments, large area (10×14 mm^2) silicon solid-state detectors were employed, all of which were fabricated at LBL. The ΔE transmission counters consisted of phosphorus-diffused silicon with thicknesses between 180 and 380 μm, and the E and E_{rej} detectors were made from lithium-drifted silicon (Si(Li)), all 5 mm thick. In order to minimize charge collection time, the counters were biased with the highest possible voltage which was between 400 and 600 V for the transmission detectors and between 1000 and 1300 V for the E detectors. A thermoelectric cooling device with a water cooled heat sink kept the temperature of the counters at about -10°C. This helped improve the resolution of the counters by reducing the thermal motion of the electrons and the associated noise and leakage current.

The combined thicknesses of the ΔE and E counters permitted measurements of protons, deuterons, and tritons with energies up to 32, 43, and 50 MeV, respectively.

E. Electronics, Data Acquisition

Figure III-3 shows a slightly simplified schematic diagram of the electronic setup employed in the counting area. The heavy lines represent the paths of analog signals. All other lines indicate logical signals.

Each counter was connected through a short (25 cm) 50Ω cable to a charge-sensitive preamplifier whose slow output was transmitted by

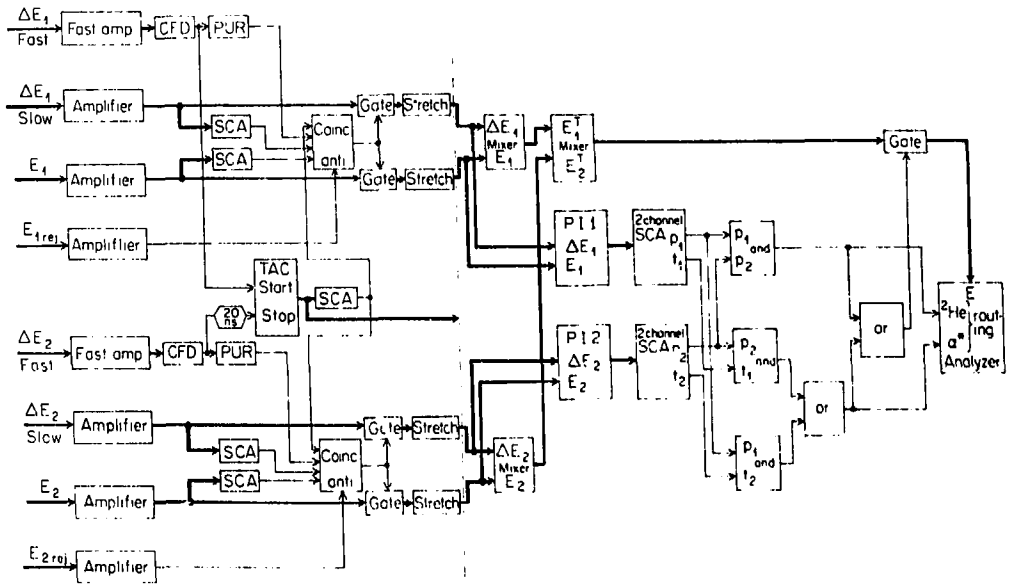

Fig. III-3. Electronic block diagram. The heavy lines distinguish the paths of analog signals from those of logical signals (light lines). In later experiments, only the part on the left side of the vertical dashed line was used.

XBL 787-1274

~50 m of 125Ω cable into a highrate linear amplifier located in the counting area. In addition to the slow analog signal, each ΔE-preamplifier produced a fast pickoff signal for timing purposes. In order to minimize degradation of the signal rise time, which affects the time resolution, these fast signals were transmitted through 50 m of high-quality low capacitance 50Ω cables to the counting area. After amplification, they were fed into constant-fraction discriminators (CFD) whose outputs served as i) strobe signals for the single-channel analyzers (SCA) that followed the amplifiers of the slow signals, ii) input signals for the fast pile-up rejectors (PUR) and iii) "start" or "stop" signals for the time-to-amplitude converter (TAC). This unit produced an output signal whose amplitude was proportional to the time-of-flight difference (ΔTOF) between two particles that were registered in the ΔE_1 and ΔE_2 detectors. A time resolution of about 400 ps (FWHM) could be achieved in the ΔTOF spectra as measured with a fast rise- time pulser.

In the initial experiments, every time there was a coincidence between i) the output signals from all four energy SCAs, ii) both PURs and iii) the TAC SCA (which was set to discriminate against coincidence events with $|\Delta TOF| > 1$ ns), each combination of ΔE-E signals was sent to a particle-identification (PI) unit which generated an analog signal using the algorithm (Go64)

$$PI = (E + \Delta E)^{1.73} - E^{1.73} \qquad \text{(III-1)}$$

Finally, both ΔE and both E signals were summed and, after gating by the output signals from the PI SCAs, stored in a 4×1024 channel analyzer. Upon completion of a run, these total energy spectra were transmitted to a SCC660 computer and subsequently written on a magnetic tape.

In order to achieve greater flexibility in analyzing the data, in later experiments only the electronics on the left side of the vertical dashed line in Fig. III-3 was used. The four energy signals ($\Delta E_1, E_1, \Delta E_2, E_2$) along with the TAC signal were digitized in a multiplexer and analog-to-digital converter (ADC) system and stored event-by-event in the buffer of a ModCompIV computer. When the buffer was full, its contents were written onto a magnetic tape. Coincidence events between any two particles were accepted with a TAC signal corresponding to a ΔTOF of about 200 ns in order also to obtain events from two sequential beam bursts for random coincidence corrections. During the data acquisition process, PI spectra as well as gated and ungated energy spectra were generated by the computer and displayed on a storage screen.

In order to both monitor the stability of the electronic system and to measure its dead time, pulser signals were injected at each preamplifier and run through the entire system. Triggering of the pulser was done by a signal from the current integrator except when targets with low melting points were used. In this case, the pulser was triggered by the monitor counter. The system dead time, which is primarily a function of the inspection time of the PUR and the count

rate in each ΔE counter, was determined by comparing the number of pulser triggers to the number of pulser signals recorded in the computer. At a count rate of 25,000 /s, the dead time could be kept below 20%. Although the singles count rate was high, the coincidence rate was only around 5 /s and it took typically between two and three hours to collect each spectrum shown in Sec. IV.

F. Data Analysis

In replaying the event-data tapes, total energy spectra and projected energy spectra were generated by setting appropriate gates in the PI and TOF spectra. The width of the TOF gate was determined from the maximum possible TOF between two correlated particles and was usually around 1.5 ns as indicated with vertical arrows in a typical TOF spectrum from the $^{12}C(d,pp)^{12}B(g.s.)$ reaction shown in Fig. III-4. In addition, total energy and projected energy spectra were created by setting a gate of equal width in the TOF spectrum over the peak which arises from coincidence events between one particle and another one from the following beam burst. These random coincidence event spectra were then subtracted from the true+random ones to obtain random corrected true coincidence spectra.

The total energy spectra were analyzed with the interactive peak-fitting program MULTID (Ma71) on a ModCompIV computer or with the program DERTAG (Ma71) on a SCC660 computer. Excitation energies of unknown peaks were determined with the aid of the least-squares fitting program LORNA (Ma71) which also takes into account the energy loss of the beam particles and the reaction products in the target.

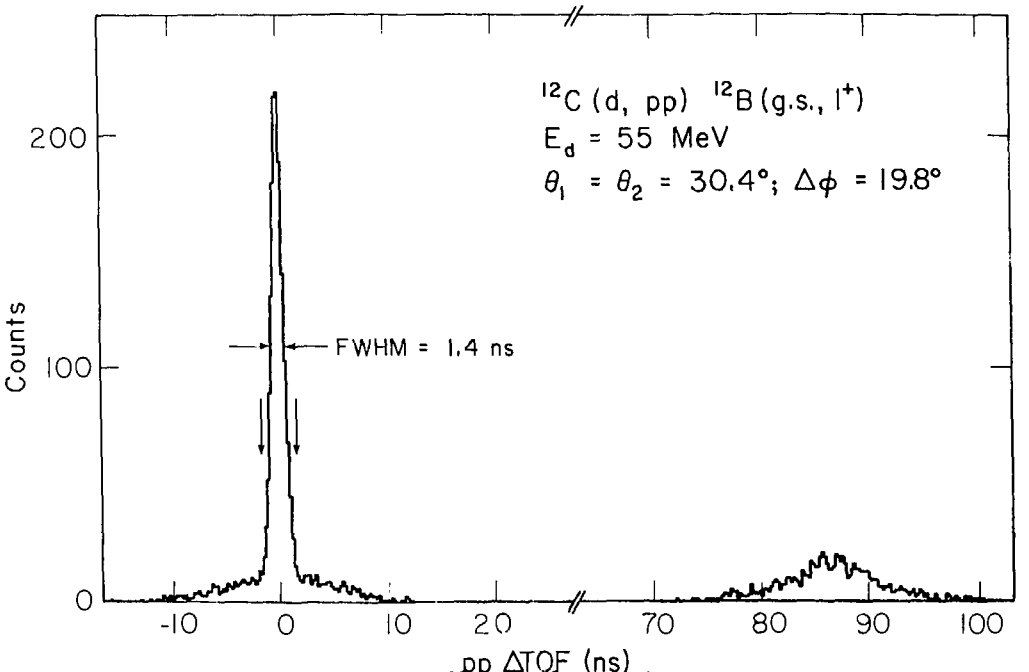

Fig. III-4. ΔTOF spectrum from the $^{12}C(d,pp)^{12}B(g.s.,1^+)$ reaction. The two vertical arrows indicate the gate settings used in generating true+random coincidence spectra.

XBL 781-12679

These calculations as well as the theoretical ones discussed in Sec. II were performed on a CDC 7600 computer.

The projected energy spectra were analyzed with the program WATMIG. This program first calculates the lab triple differential cross section $d^3\sigma/d\Omega_1 d\Omega_2 dE_1$ using the formula

$$\frac{d^3\sigma}{d\Omega_1 d\Omega_2 dE_1} = \frac{N}{\Delta\Omega_1 \Delta\Omega_2 \Delta E_1 \left(\frac{\text{particles}}{\mu\text{C beam}}\right)\left(\frac{\text{target nuclei}}{\text{cm}^2}\right)}$$

$$= \frac{2.66\times10^{-7} N\, z\, A}{\Delta\Omega_1 \Delta\Omega_2 \Delta E_1\, C\, T}\left[\frac{\text{mb}}{\text{sr}^2\text{MeV}}\right] \qquad \text{(III-2)}$$

where N = number of counts within the bin width ΔE_1

z = charge state of beam particles after passage through the target

A = target mass (amu)

$\Delta\Omega_1$ = solid angle (sr) of counter 1

$\Delta\Omega_2$ = solid angle (sr) of counter 2

ΔE_1 = E_1 step size (MeV)

C = integrated beam current (μC)

T = target thickness (mg/cm^2)

The program then converts the lab cross section to the c'(3) system by the Jacobian transformation (II-8) and performs the integration (II-11) over a specified range of ε. The c.m. angle $\theta_{c.m.}$ at which the c.m. of $(1+2)^*$ was emitted is calculated according to

$$\theta_{c.m.} = \sin^{-1}\left[\left(\frac{E_{1+2}}{E^{c}_{1+2}}\right)^{1/2} \sin\theta_{lab}\right] \qquad \text{(III-3)}$$

where

$$E_{1+2} = E_1 + E_2 - \epsilon \qquad \text{(III-4)}$$

$$E^{c}_{1+2} = \frac{m_3}{m_1+m_2+m_3}(E^{c}_{tot} - \epsilon) \qquad \text{(III-5)}$$

$$E^{c}_{tot} = Q + E_p \frac{m_T}{m_p+m_T} \qquad \text{(III-6)}$$

and θ_{lab} is approximated by the lab angle of the center of the detection system. Since $\theta_{c.m.}$ is a function of ϵ, (III-3) is averaged over the integration range.

IV. Experimental Results and Discussion

The present study of reactions producing unbound outgoing particles focuses on two such particles. Section A presents results from reactions involving ^{2}He which is detected by means of its two breakup protons, and Sec. B discusses the results from the experiments producing ^{4}He nuclei in excited states (α^*) which are measured via the breakup particles p and t.

A. Reactions Producing ^{2}He

Although the 2p system does not possess any bound states, there exists a state near threshold which may be identified with the g.s. of ^{2}He as is discussed in detail in Secs. 1 and 2. Section 3 presents the results from the (^{3}He,^{2}He) reaction which is the simplest reaction that forms ^{2}He and therefore important for the study of the mechanism of a reaction with ^{2}He in its final state. In order to evaluate its promise as a spectroscopic tool to investigate high-spin states, the (α,^{2}He) reaction was then studied on many light target nuclei as is discussed in Sec. 4. Finally, a more complicated reaction process will be considered in Sec. 5 where the results from a study of the (d,^{2}He) charge-exchange reaction are presented.

1. Characterization of ^{2}He

It is well known that the deuteron ground state $J^\pi = 1^+$, T = 0, E = -2.224 MeV is the only existing bound state of the two-nucleon system. The first excited state of the deuteron (d^*) with $^{2S+1}L_J = {}^1S_0$ and T = 1 and also its isobaric analog states, the nn (di-neutron) g.s. and the pp (di-proton) g.s. barely fall short

of forming bound states, even if in the latter case allowance is made for the Coulomb repulsion between the two protons. The reason for the unbound nature of these states is the fact that the nuclear force in the $^1S_0$ state is not strong enough to form a bound state.

Although no bound states of the pp system exist, in many experiments such as the ^{3}He(d,t)pp reaction (Co 64), a broad state near the threshold with quantum numbers $^1S_0$, T=1 has been observed, which will henceforth be referred to as the ^{2}He g.s. or just ^{2}He. In describing this rather special type of state, it is convenient to use the unified description of states as poles of the S-matrix (Nu59, Ta72). In this theory, bound states are poles on the negative real axis of the first (physical) sheet of the Riemann surface associated with the complex energy plane. The singlet two-nucleon states are then singularities also on the negative real energy axis but on the second (unphysical) sheet of the Riemann surface and are called antibound states (Nu 59). From the effective range theory, the pole position of the d^* state is found to be at -68 keV. For the ^{2}He state, the exact pole position is more difficult to determine because of the Coulomb force. If the latter is properly accounted for, the pole is calculated to lie at about -120 keV. Antibound states exist only for L = 0 states close to the origin. So far, the $^1S_0$ state of the di-nucleon system is the only case of this type known.

In contrast to antibound states, Breit-Wigner type resonances are poles at positive real and negative imaginary energies, but also on the second sheet. The difference between antibound states and Breit-Wigner resonances is most conspicuous in the behavior of the phase

shifts δ associated with these states. Whereas for Breit-Wigner resonances δ passes through $\pi/2$ at the resonance energy, no such behavior is found for antibound states. Therefore, the phase shifts of antibound states are not characterized with resonance energies and widths, but are usually parameterized in the effective-range approximation with scattering lengths a and effective ranges r_{eff}. From low energy pp scattering data, it has been found that the nuclear S-wave phase shift δ_0 in the presence of the Coulomb interaction as a function of the relative momentum k can be described by (S171)

$$C^2 k \cot \delta_0 = -(1/a) - h(\eta)/R + \frac{1}{2} r_{eff} k^2 \qquad \text{(IV-1)}$$

where

$$\eta = 1/(2kR) \qquad \text{(IV-2)}$$

$$R = \hbar^2/(2\mu Z_1 Z_2 e^2) \qquad \text{(IV-3)}$$

$$C^2 = 2\pi\eta/\left[\exp(2\pi\eta)-1\right] \qquad \text{(IV-4)}$$

$$h(\eta) = \eta^2 \sum_{n=1}^{\infty} 1/\left[n(n^2 + \eta^2)\right] - \ln\eta - 0.57722 \qquad \text{(IV-5)}$$

Although values for a and r_{eff} are well known from fitting low energy pp scattering data with (IV-1), no universally accepted values

have been established. In this work the values $a = -7.82$ fm and $r_{eff} = 2.81$ fm have been adopted from a review by Henley (He69).

2. Projected energy spectra

If one is really dealing with the detection of ^{2}He in these experiments, then the shapes of the projected energy spectra $d^3\sigma/d\Omega_1 d\Omega_2 dE_1$ from reactions producing ^{2}He as an outgoing particle should be accounted for by FSI calculations. As discus n Sec. II.B.3, the shape of the projected energy spectra can be described by

$$\frac{d^3\sigma}{d\Omega_1 d\Omega_2 dE_1} \propto J_{12}k \quad |\varphi(k,r)|^2 = J_{12}k \left| \frac{e^{-i\delta_0}(F_0\cos\delta_0 + G_0\sin\delta_0)}{kr} \right|^2 \qquad \text{(IV-6)}$$

where δ_0 is given by (IV-1) and $r = 1.4$ fm which is the matching radius for the internal and external wave functions (Ph64). If $kr \ll 1$, $\varphi(k,r)$ together with (IV-1) can be approximated by

$$\varphi(k,r) \propto \frac{e^{-i\delta_0}\sin\delta_0}{Ck} \left(\frac{1}{r} - \frac{1}{a}\right) \qquad \text{(IV-7)}$$

which reduces (IV-6) to the expression first given by Migdal (Mi55) (and by Watson (Wa52) for the case without Coulomb interaction)

$$\frac{d^3\sigma}{d\Omega_1 d\Omega_2 dE_1} \propto \frac{J_{12}k}{C^2k^2 + \frac{1}{C^2}\left(-\frac{1}{a} + \frac{1}{2}r_{eff}k^2 - \frac{h(\eta)}{R}\right)^2} \quad . \qquad \text{(IV-8)}$$

This formula has been used to fit projected energy spectra from three different reactions all producing ^{2}He as an outgoing particle, and the results are shown in Figs. IV-1 and 2. Because of the large cross section of the (^{3}He,^{2}He) reaction it was possible to measure the spectrum from the ^{13}C(^{3}He,^{2}He)^{14}C(6.73 MeV) reaction with the narrow collimator geometry C (Table III-1) which permitted an identification of pp events with relative energies as low as 90 keV. The spectra from the ^{12}C(α,^{2}He)^{14}C(10.72 MeV) and ^{12}C(d,^{2}He) ^{12}B(g.s.) reactions were obtained with the large solid angle collimator geometry B for which the minimum relative energy is 0.26 and 0.29 MeV, respectively. (Of course, events with smaller values of ε are also contained in these spectra, but cannot be resolved from those with larger ones due to the large range of θ_{12}). As can be seen, the calculations and data show a maximum for $\varepsilon \approx 500$ keV. This maximum is caused by the Coulomb repulsion between the two protons which counteracts the attractive nuclear interaction for small relative energies and results in a reduction of the cross section. (In the absence of the Coulomb interaction the spectra would peak at $\varepsilon = 0$ MeV, as is clearly observed in the corresponding spectrum measured in a study of the (^{3}He,d*) reaction (Ja76c)). In general, there is good agreement between the FSI theory and the experimental data. Some deviations at larger relative energies are most likely due to the fact that $T_{fi}^{(3')}$ is not quite independent of ε, but may also indicate a breakdown of the approximation (II-45) itself.

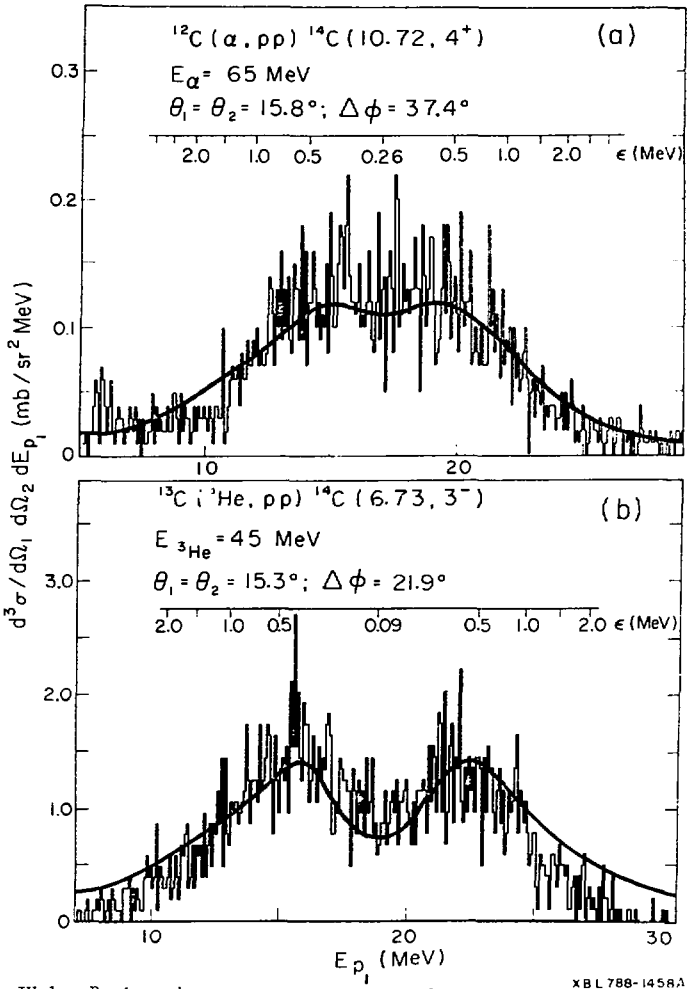

Fig. IV-1. Projected proton energy spectra from a) the $^{12}C(\alpha,pp)^{14}C(10.72,4^+)$ reaction at E_α = 65 MeV and b) the $^{13}C(^3He,pp)^{14}C(6.73,3^-)$ reaction at $E_{^3He}$ = 45 MeV. The solid curves represent the results from FSI calculations.

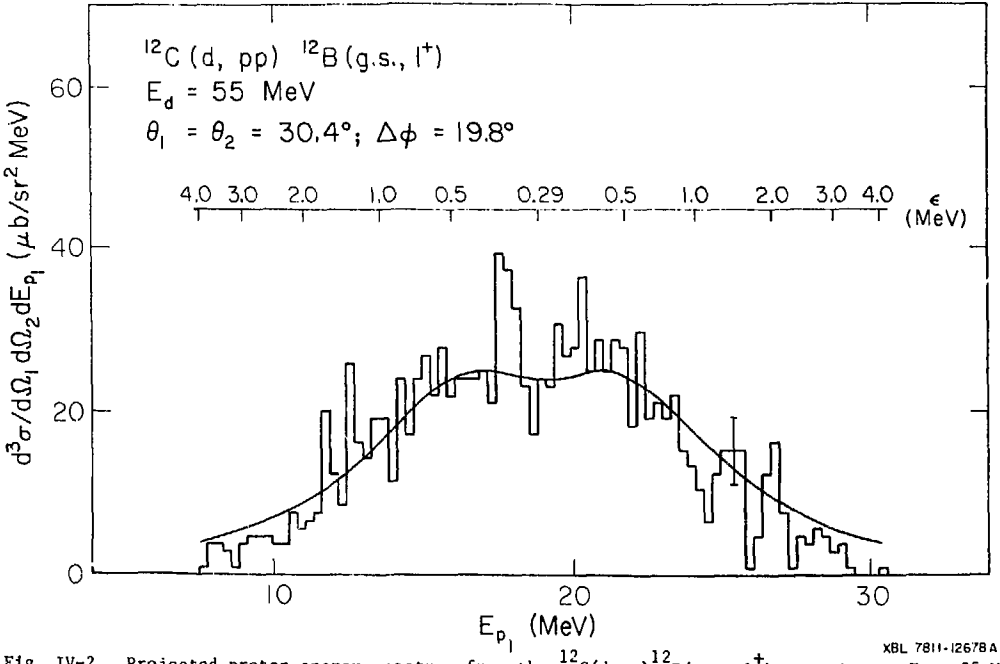

XBL 7811-12678A

Fig. IV-2. Projected proton energy spectrum from the $^{12}C(d,pp)^{12}B(g.s.,1^+)$ reaction at E_d = 55 MeV. The solid line represents the results from FSI calculations.

3. The (^{3}He,^{2}He) reaction

The (^{3}He,^{2}He) reaction has the virtue of being the simplest reaction that produces ^{2}He. Since it is a single-nucleon transfer reaction, it possesses a large cross section and is therefore particularly suited to the study of the mechanism of reactions involving ^{2}He. Although the (^{3}He,^{2}He) reaction is expected to be quite similar to the (d,p) reaction (the g.s. Q-value Q_0(^{3}He,^{2}He) is only 5.5 MeV smaller than Q_0(d,p)), the two reactions differ in that the (^{3}He,^{2}He) reaction can involve isospin transfers T = 1/2 and 3/2 whereas the (d,p) reaction is restricted to T = 1/2. However, since T = 3/2 transitions require target core excitation, the cross section for such two-step processes is drastically reduced (He67). In fact, none of the reactions investigated here provided evidence for such transitions.

a. Energy spectra

Energy spectra from the (^{3}He,^{2}He) reaction were measured at $E_{^3He}$ = 60 MeV on targets of ^{6}Li (99.9% enriched, 340 μg/cm^2), ^{7}Li (99.9% enriched, 400 μg/cm^2), ^{9}Be (800 μg/cm^2), ^{12}C (natural, 360 μg/cm^2), and ^{13}C (80% enriched, 190 μg/cm^2) using the detection system geometry A (Table III-1).

^{6}Li(^{3}He,^{2}He)^{7}Li (Q_0 = -0.468 MeV)

A spectrum from the ^{6}Li(^{3}He,^{2}He)^{7}Li reaction is shown in Fig. IV-3a. Similar to the spectra obtained from the ^{6}Li(d,p)^{7}Li reaction (Ha60, Sch67), strong transitions are observed to the g.s.,

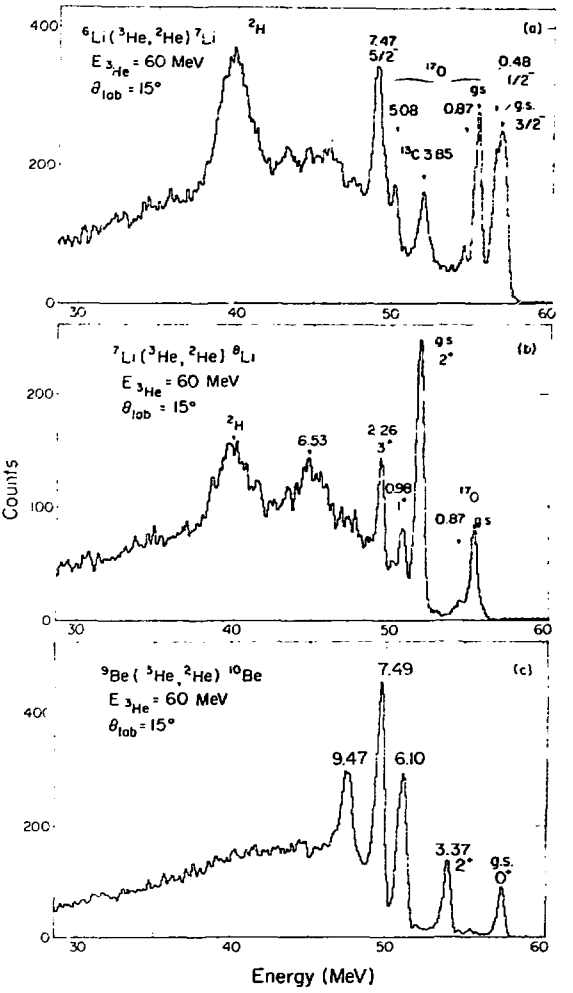

Fig. IV-3. ^{2}He energy spectra from the (^{3}He,^{2}He) reaction at $E_{^3He}$ = 60 MeV and θ_{lab} = 15° on targets of a) ^{6}Li, b) ^{7}Li, and c) ^{9}Be.

$3/2^-$ and the 0.48-MeV, $1/2^-$ state (unresolved doublet) as well as to the 7.47-MeV, $5/2^-$ state. Population of these states is consistent with the large single-particle spectroscopic factors of 0.75, 1.02, and 0.64, respectively, as calculated with intermediate-coupling wave functions (Ha60). The peak observed near the location of the 4.63-MeV, $7/2^-$ state which should not be populated in this reaction (Ha60) is predominantly due to the strong transition to the 3.85-MeV, $5/2^+$ state in ^{13}C which arises from carbon contamination in the target. Contamination by oxygen gave rise to peaks corresponding to transitions to the ^{17}O g.s., $5/2^+$ and the excited states at 0.87 MeV, $1/2^+$ and 5.08 MeV, $3/2^+$.

$\underline{^7Li(^3He,^2He)^8Li}$ (Q_0 = -5.684 MeV)

Figure IV-3b presents a spectrum from the (^3He,^2He) reaction on ^7Li. Strong transitions are observed to the g.s., 2^+, the 0.98-MeV, 1^+ and 2.26-MeV, 3^+ states which are also strongly populated by the (d,p) reaction (Ha60). All these states possess considerable single-particle character; their theoretical spectroscopic factors are 1.1, 0.54, and 0.33, respectively (Ha60). Peaks from target contaminations are also indicated in this spectrum. They do not interfere with the ^8Li spectrum except for a possible peak from the transition to the ^{13}C, 3.85-MeV state which coincides with the ^8Li g.s. peak.

$^{9}Be(^{3}He,^{2}He)^{10}Be$ (Q_0 = -0.906 MeV)

Transitions to the g.s., 0^+ and the 3.37-MeV, 2^+ state of ^{10}Be could be identified in the spectrum from the (^3He,^2He) reaction on ^9Be as shown in Fig. IV-3c. The remaining strong peaks observed at E_x = 6.10, 7.49, and 9.47 ± 0.07 MeV cannot be uniquely identified with known states. Based on results from the (d,p) reaction (An74), the peak at 6.10 MeV is most likely composed of the 5.9583, 2^+; 5.9599-MeV, 1^-; and 6.26-MeV, 2^- states. The peak at 7.49 MeV is an unresolved doublet consisting of the 7.37-MeV, 3^- and 7.54-MeV, 2^+ states. Finally, the somewhat broad peak observed at 9.47 MeV may be identified with the known 9.4-MeV, $(2)^+$ state.

$^{12}C(^{3}He,^{2}He)^{13}C$ (Q_0 = -2.771 MeV)

Figure IV-4a shows a spectrum from the (^3He,^2He) reaction on ^{12}C. The strongest peak in this spectrum arises from the transition to the 3.85-MeV, $5/2^+$ state whose configuration is $\left\{^{12}C(0^+) \otimes d_{5/2}\right\}_{5/2^+}$, with possible contributions from transitions to the unresolved 3.68-MeV, $3/2^-$ state. However, judged by the small cross section to the 3.68-MeV state in the $^{12}C(d,p)^{13}C$ reaction (Mc55), contributions from it can be neglected. In addition to the transition to the g.s., $1/2^-$ with configuration $\left\{^{12}C(0^+) \otimes p_{1/2}\right\}_{1/2}$, peaks are observed at E_x = 7.60, 8.47, 9.65, 11.00, and 12.42 ± 0.07 MeV, which cannot be identified with any known states due to the high density of states in this region.

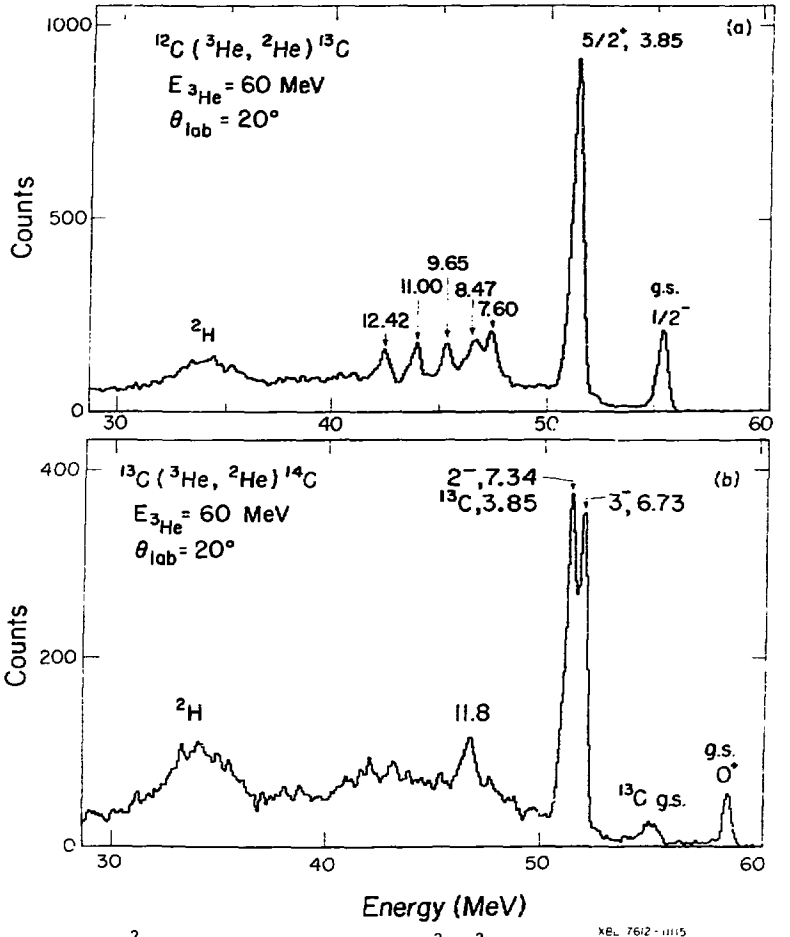

XBL 7612-1115

Fig. IV-4. ^{2}He energy spectra from the (^{3}He,^{2}He) reaction at $E_{^3He}$ = 60 MeV and θ_{lab} = 20° on targets of a) ^{12}C and b) ^{13}C.

$^{13}C(^{3}He,^{2}He)^{14}C$ (Q_0 = 0.459 MeV)

In the spectrum from the ($^{3}He,^{2}He$) reaction on ^{13}C (Fig. IV-4b) the main single-particle transitions observed are the same as are observed on the ^{12}C target. Since the ^{13}C g.s. possesses $J^{\pi} = 1/2^{-}$, the transferred $d_{5/2}$ neutron couples to the target core giving rise to two closely spaced states with $J^{\pi} = 3^{-}$ and 2^{-} with configuration $\left\{^{12}Cp_{1/2} \otimes d_{5/2}\right\}^{3^-,2^-}$ at E_x = 6.73 and 7.34 MeV, respectively. No such splitting is possible for the g.s. transition in which the transferred neutron just closes the neutron p-shell and can couple only to $J^{\pi} = 0^{+}$. A somewhat broad peak is also observed at E_x = 11.66 ± 0.08 MeV which probably corresponds to the 11.9 ± 0.3 MeV state seen in the (d,p) reaction (Aj76), but not yet assigned with spin and parity. Also observed are peaks arising from the reaction on ^{12}C in the target. Whereas the weak transition to the ^{13}C g.s. is well separated from those to ^{14}C, the strong transition to the ^{13}C 3.85-MeV state interferes considerably with that to the ^{14}C 7.34-MeV state.

b. Angular distributions, DWBA analysis

In Fig. IV-5 angular distributions are shown for the ($^{3}He,^{2}He$) reaction on ^{12}C leading to the g.s., $1/2^{-}$ and the 3.85-MeV, $5/2^{+}$ state and on ^{13}C leading to the g.s., 0^{+} and the 6.73-MeV, 3^{-} state measured at a bombarding energy of 50 MeV. Differential cross sections were obtained by integrating the projected energy spectra between ε_{ℓ} = 0.4 MeV and ε_{u} = 1.0 MeV.

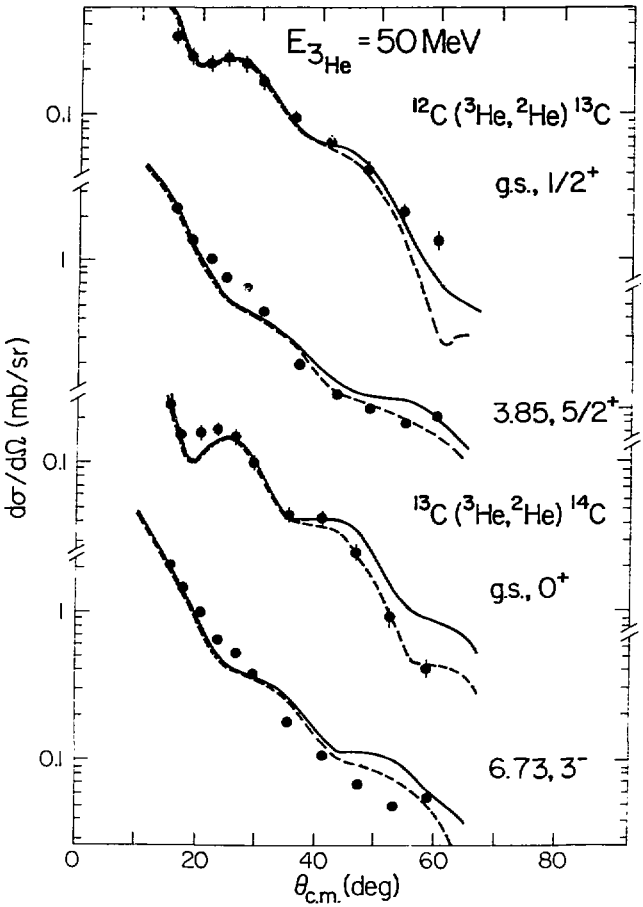

Fig. IV-5. Angular distributions from the (^{3}He,^{2}He) reaction on targets of ^{12}C and ^{13}C at $E_{^3He}$ = 50 MeV leading to the g.s., $1/2^-$ and 3.85-MeV, $5/2^+$ states in ^{13}C and to the g.s., 0^+ and 6.73-MeV, 3^- state in ^{14}C. The solid and dashed curves represent the results from an EFR and ZR DWBA analysis, respectively. XBL 798-2742

Following the discussion in Sec. II.B.1, the reaction mechanism of the (^{3}He,^{2}He) reaction can be simplified by assuming that this three-body reaction proceeds as a sequential two-body reaction. The first step involves the production of ^{2}He which consists in a removal of a bound neutron from ^{3}He and its transfer into a bound state in the final nucleus, and the second step is the breakup of ^{2}He into two protons. A similar assumption has also been made in the analysis of the (^{9}Be,^{8}Be) reaction (St77) at 50 MeV Since ^{8}Be g.s. is relatively long-lived ($\tau \approx 10^{-16}$ s) and thus travels several atomic diameters before it disintegrates, the production and decay of ^{8}Be are clearly separated in space and time. Such a statement is less justified in the case of the (^{3}He,^{2}He) reaction, since the ^{2}He g.s. is quite broad. However, an indication that production and decay of ^{2}He can be separated has already been obtained in the successful treatment of the second step with the FSI theory (Sec.IV.A.2). It is therefore reasonable to try to analyze the first step with conventional DWBA.

The DWBA analysis has been performed in the EFR and ZR approximation under the assumption the ^{2}He is bound, but possesses no internal energy. Figure IV-5 presents the results of the calculations normalized to the experimental data. The solid and dashed curves represent EFR and ZR calculations, respectively.

The optical model parameters for the entrance channel were taken from an analysis of 50 MeV ^{3}He elastic scattering on ^{12}C (Ba69): $V = 160$ MeV, $r_V = 1.4$ fm, $a_V = 0.572$ fm, $W = 20.3$ MeV, $r_W = 1.7$ fm,

a_W = 0.537 fm. For the exit channel, the optical parameters were approximated by those obtained from 52 MeV deuteron elastic scattering on ^{12}C (Hi68) : V = 71.8 MeV, r_V = 1.25 fm, a_V = 0.7 fm, $4W_D$ = 44 MeV, r_W = 1.25 fm, a_W = 0.7 fm. In order to improve the fit to the data, it was necessary to increase the well depth of the surface imaginary potential $4W_D$ from 11 to 44 MeV. Such an adjustment is allowed since elastic scattering of ^2He cannot be measured. It is also justifiable on physical grounds because this more absorptive potential is more likely to be a realistic approximation to the true ^2He optical potential.

The target bound state wave functions were generated in the usual way with a real Woods-Saxon potential with radius $R = 1.25\ A_{tgt}^{1/3}$ and diffuseness a = 0.65 fm. In the EFR DWBA a bound-state wave function for the projectile is also required. It was calculated for a neutron bound by 7.18 MeV in a Woods-Saxon well with radius R = 1.88 fm which corresponds to the experimental charge r.m.s. radius of ^3He (Mc70), and a diffuseness a = 0.65 fm. If D_0 (II-31) is calculated with this potential and wave function, one finds a value of -201.5 MeV $fm^{3/2}$. For comparison purposes, the same bound state potential was used to calculate D_0 for the (t,d) reaction (a neutron bound by 6.26 MeV) and the (^3He,d) reaction (a proton bound by 5.49 MeV) and one found D_0 = -182.6 and -180.1 MeV $fm^{3/2}$, respectively, which is in good agreement with D_0 = -183.6 and -172.8 MeV $fm^{3/2}$ as calculated by Bassel (Ba66). Although the bound state potential approach used here to obtain the radial wave function of the transferred neutron in

^{3}He gives reasonable results, a more sophisticated treatment would employ a realistic interaction potential and a wave function generated by carrying out the integral (II-33). Because of the unbound nature of ^{2}He such calculations are fraught with difficulties and will not be discussed (Ja 76c). However, since the shapes of the calculated distributions are very similar for both the EFR and ZR calculations, it seems that the exact form of the potential and wave function is not very important in determining the shape, but may affect the absolute magnitude of the cross section.

Using $D_0 = -201.5$ MeV fm$^{3/2}$ and $C^2S_{^3He} = 1$, one obtains for the ZR normalization constant (II-38) N = 4.1. A value of N can also be extracted from a comparison between EFR and ZR DWBA calculations. By combining (II-35) and (II-37) one finds

$$N = \frac{C^2S_{^3He}\,(2\ell + 1)W^2\sigma_{LOLA}}{\sigma_{DWUCK4}/(2j + 1)} \qquad \text{(IV-9)}$$

From the four calculated angular distributions, an average value N = 5.40 ± 0.50 was obtained. The difference between these two values of N is most likely due to finite-range effects which are neglected in DWUCK4.

Comparison between the experimental and theoretical absolute magnitude of the cross section must take into account the fact that the data do not contain the entire ^{2}He g.s., but only the part with $0.4 \leq \varepsilon \leq 1.0$ MeV. Assuming the shape of the relative energy spectrum is given by (IV-6), the ratio

$$R = \frac{\int_{\varepsilon_{min}}^{\varepsilon_{max}} k \quad |\phi(k,b)|^2 d\varepsilon}{\int_{0.4}^{1.0} k \quad |\phi(k,b)|^2 d\varepsilon} \qquad \text{(IV-10)}$$

indicates the amount of the cross section that is not included in the data. Evaluating (IV-10) for $\varepsilon_{min} = 0$ and $\varepsilon_{max} = 10$ MeV one finds $R = 10.1$. Since EFR DWBA calculates absolute cross sections provided the S-factors are known, a value of R can also be determined from the relation

$$R = \frac{(d\sigma/d\Omega)^{LOLA}}{(d\sigma/d\Omega)^{exp}_{0.4,\ 1.0}} \quad . \qquad \text{(IV-11)}$$

Table IV-1 gives a summary of these R values calculated with $(d\sigma/d\Omega)^{LOLA}$ using theoretical as well as experimental absolute S-factors quoted in the literature. For ^{13}C g.s. the experimental S-factor (Sch67) is twice as large as the theoretical one (Co65). This is quite consistent with the results obtained from the $^{13}C(^3He,\alpha)^{12}C$ reaction (Sec. IV.B.3). In the case of the ^{14}C g.s., the experimental values (Sch67, Da78) are also larger than the theoretical ones (Co65). No experimental or theoretical S-factors exist for the ^{13}C 3.85-MeV and ^{14}C 6.73-MeV states so S_B was set equal to unity assuming a pure $d_{5/2}$ configuration. From the g.s. transitions using the experimental S-factors, one finds an average value $R = 11.8 \pm 3.1$ which agrees well with that of 10.1 calculated with (IV-10). These results indicate that the "total" cross section

Table IV-1 Theoretical and experimental spectroscopic factors S and ratio R[Eq. (IV-11)] for states in ^{13}C and ^{14}C that are populated in the (^{3}He,^{2}He) reaction.

	E_x	J^{π}	$S_{th.}$	R	S_{exp}	R
^{13}C	g.s.	$1/2^-$	0.61[a]	8.2	1.16[c]	15.4
	3.85	$5/2^+$	1.00[b]	25.8	-	-
^{14}C	g.s.	0^+	1.73[a]	7.9	2.05[c]	9.4
					2.35[d]	10.7
	6.73	3^-	1.00[b]	15.4	-	-

[a] (Co65)

[b] Maximum value expected from jj-coupling model.

[c] (Sch67)

[d] (Da78)

$d\sigma/d\Omega_{^2He}$ may be obtained by multiplying the cross section measured between ε = 0.4 and 1.0 MeV by a factor of about ten. The forward angle cross sections for the strongest transitions are then of the order of 10 mb/sr and thus comparable to those of the (^{3}He,d) reactions.

The excellent agreement between the experimental and calculated shapes of the angular distributions indicates that the reaction mechanism of the (^{3}He,^{2}He) reaction is well described by the DWBA theory. Apparently, the unbound nature of ^{2}He does not affect the reaction process. The results of the calculations also show that the ^{2}He optical potential is well approximated by that of a deuteron of the same energy. Although ^{2}He is very short-lived, the successful treatment of both the ^{2}He angular distributions and the shape of the relative energy spectra seems to justify the assumed separation of production and decay of ^{2}He and makes it possible to treat ^{2}He as quasi-bound nucleus.

4. The (α,^{2}He) reaction

Investigation of the (α,^{2}He) reaction as a potential spectroscopic tool to study 2n states has been prompted by the expected similarity between the (α,^{2}He) and the (α,d) reactions. Studies of the (α,d) reaction on light targets (Ri66) have shown that this reaction selectively populates high-spin np states with simple configurations such as $(1d_{5/2})^2_{5^+}$ and $(1f_{7/2})^2_{7^+}$. This selectivity is caused by several reasons. Typical Q_0 values are around -15 MeV which gives rise to a large value for the angular

momentum mismatch L between the incoming and outgoing channels, which is defined for a surface reaction as

$$\Delta L = |\ell_i - \ell_f| \qquad \text{(IV-12)}$$

where ℓ_i and ℓ_f are the partial waves of the initial and final channels for which the elastic S-matrix equals 0.5. For E_α = 60 MeV and $A_{tgt} < 40$, $L \approx 5$ for g.s. transitions and >5 for transitions to excited states. Optimum cross sections are obtained if

$$\Delta L \approx \ell \qquad \text{(IV-13)}$$

where ℓ is the orbital angular momentum transfer of the reaction. As a result of the large values of ΔL for the (α,d) reactions, transitions that involve little or no ℓ transfers are kinematically inhibited and thus reduced in cross section and appear in the deuteron energy spectra only as small peaks. Another reason why the high-spin states stand out so distinctly in the spectra is the fact that these states possess quite pure configurations since there are very few high-spin states in the neighborhood that could give rise to configuration mixing.

The same arguments hold true for the $(\alpha,{}^2He)$ reactions whose Q_0-values are similar to those of the (α,d) reactions. Thus, one expects to observe in the ${}^2He$ energy spectra transitions to 2n states with configurations such as $(1d_{5/2})^2_{4^+}$ and $(1f_{7/2})^2_{6^+}$. (Coupling of identical particles to higher spin values J is precluded by the Pauli exclusion principle which allows

only J values that satisfy the condition $(-1)^{J}=\pi$). Only a small number of these high-spin states are known in light nuclei: the analogous (t,p) reaction mainly populates the lower spin states because its Q_0 values are about 20 MeV larger than those of the $(\alpha,{}^2He)$ reaction and triton beams are currently only available at moderate energies (<25 MeV) at a few selected laboratories. Furthermore, only a few heavy-ion induced 2n-transfer reactions have been reported (An74a, Ha78). Therefore, the $(\alpha,{}^2He)$ has been studied on targets with A < 40 in the hope of locating some of these high-spin states.

a. Energy spectra

The $(\alpha,{}^2He)$ reaction has been surveyed on solid and gaseous 1p- and 2sld-shell targets whose composition, thickness or gas pressure are summarized in Table IV-2. In the reaction on the p-shell targets, one expects predominant population of states formed by capturing the two stripped neutrons into the $d_{5/2}$ orbital coupled to $J = 4^+$, whereas on the sd-shell targets, configurations involving f orbitals such as $(f_{7/2})^2_{6^+}$ and $(d_{3/2}f_{7/2})_{5^-}$ are expected to be preferentially produced. Spectra from the $(\alpha,{}^2He)$ reaction on ^{12}C, ^{13}C, ^{14}N, ^{15}N, and ^{16}O will first be discussed followed by a presentation of the results from the sd-shell targets ^{40}Ca, ^{38}Ar, ^{36}Ar, ^{32}S, ^{28}Si, ^{26}Mg, ^{29}Si, ^{24}Mg, ^{22}Ne, ^{20}Ne, and ^{18}O. (This order for the sd-shell targets was taken to permit initial discussion of the $(f_{7/2})^2_6$ levels in a well known region).

Table IV-2 Isotopic purities, solid target thicknesses and gas target pressures at 25°C.

Target	Isotopic Purity (%)	Thickness ($\mu g/cm^2$)	Pressure (atm)
^{12}C	98.9	350	
^{13}C	90.0	140	
$^{14}N_2$	99 6		0.20
$^{15}N_2$	99.7		0.20
$^{16}O_2$	99.8		0.20
$^{18}O_2$	97.2		0.19
^{20}Ne	99.95		0.28
^{22}Ne	99.65		0.27
^{24}Mg	99.96	650	
^{26}Mg	99.42	300	
^{28}Si	99.8	410	
^{29}Si	95.0	500	
$Sb_2\ ^{32}S_3$	95.0	750	
^{36}Ar	99.5		0.27
^{38}Ar	95.0		0.29
^{40}Ca	99.97	620	

Because the intention of the present study has been to provide an intitial survey of the properties of the $(\alpha,{}^2He)$ reaction, rather than to obtain and analyze detailed angular distributions, most J^π assigments made from our data must be considered highly probably rather than definitive.

$\underline{{}^{12}C(\alpha,{}^2He){}^{14}C}$ (Q_0 = -15.17 MeV)

Figure IV-6 shows a spectrum from this reaction at θ_{lab} = 12°. Except for weak population of the g.s. and a state at 14.9 ± 0.1 MeV, only the known 3^- state at 6.73 MeV and a state at 10.72 MeV are strongly populated. The 3^- state is known to be of dominant $(p_{1/2}d_{5/2})_3$ character (Tr63), whereas recent studies of the 2n-transfer reactions (t,p) (Mo78), $({}^{10}B,{}^8B)$ (Ha78) and $({}^{12}C,{}^{10}C)$ (An74a) have established the $(d_{5/2})^2_4$ character of the state at 10.72 MeV. This excitation energy for the 4^+ state is in agreement with the previously reported values of 10.736 ± 0.005 MeV (Ma78) and 10.77 ± 0.11 MeV (Ha78). The state at 14.9 MeV was also observed with comparable relative strength in the study of the $({}^{10}B,{}^8B)$ reaction (Ha78).

$\underline{{}^{13}C(\alpha,{}^2He){}^{15}C}$ (Q_0 = -18.90 MeV)

A spectrum from this reaction at θ_{lab} = 12° is shown in Fig. IV-7a. Since the ^{12}C and ^{13}C targets only differ by a $1p_{1/2}$ neutron, one expects the $(\alpha,{}^2He)$ reaction on ^{13}C to populate

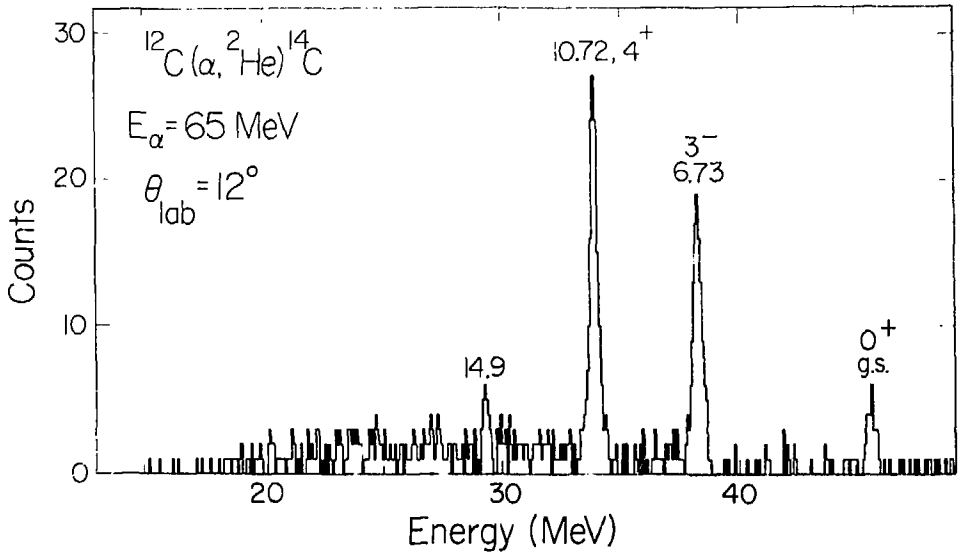

XBL 7711-11341

Fig. IV-6. ^{2}He energy spectrum from the $^{12}C(\alpha, {}^{2}He)\ ^{14}C$ reaction at E_α = 65 MeV and θ_{lab} = 12°.

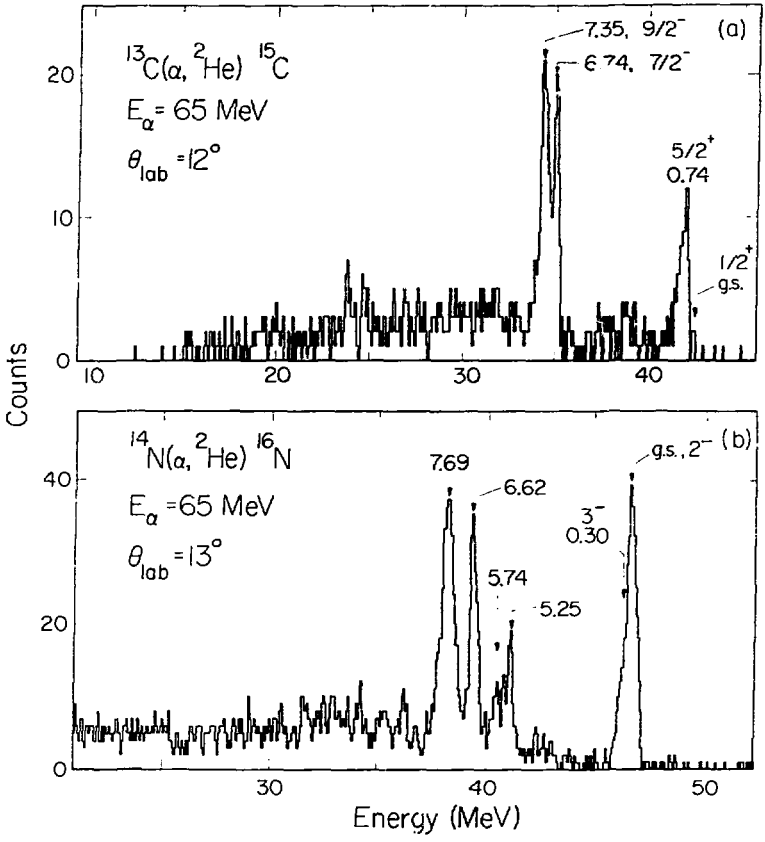

Fig. IV-7. ^{2}He energy spectra from the $(\alpha, {}^{2}He)$ reaction at E_α = 65 MeV on a) ^{13}C at θ_{lab} = 12° and b) ^{14}N at θ_{lab} = 13°.

preferentially states with the same 2n configurations observed in reactions on ^{12}C, but now coupled to the $J^{\pi} = 1/2^{-}$ target core. Thus, the states observed in the $^{12}C(\alpha,{}^{2}He)^{14}C$ spectra should be split (where possible) into two components in the $^{12}C(\alpha,{}^{2}He)^{15}C$ spectra similar to the splitting observed in the analogous (α,d) reactions on ^{12}C and ^{13}C (Ri66). Population of the doublet in ^{15}C observed at 6.74 and 7.35 MeV can be interpreted as transitions to states having predominantly $\left[\{^{12}C(0^{+})p_{1/2}\}_{1/2} \otimes (d_{5/2})^{2}_{4}\right]_{7/2^{-},9/2^{-}}$ character. The ratio of the experimental differential cross sections, over the angular range $\theta_{lab} = 12^{o}$ to 50°, for the transitions to the states at 6.74 and 7.35 MeV is about 4:5 which, applying the (2J+1) rule for the relative population of such states in stripping reactions, leads to the tentative assignments of $J^{\pi}=7/2^{-}$ for the 6.74 MeV state and $J^{\pi} = 9/2^{-}$ for the 7.35-MeV state. This latter result corroborates the tentative assignment of $9/2^{-}$ for the 7.35 MeV state given in (Aj76). Since the $5/2^{+}$ state at 0.74 MeV has a configuration $\left[\{^{12}C(0^{+})p_{1/2}\}_{1/2} \otimes p_{1/2}d_{5/2}\right]_{5/2^{-}}$ and $p_{1/2}$ neutron of ^{13}C and the transferred $p_{1/2}$ neutron must couple to J = 0 and no splitting can arise.

<u>$^{14}N(\alpha,{}^{2}He)^{16}N$</u> ($Q_0$ = -14.97 MeV)

The $J^{\pi} = 1^{+}$, g.s. of ^{14}N can be described as $\left[^{12}C(0^{+})\nu p_{1/2}\pi p_{1/2}\right]_{1^{+}}$; thus, one expects that three states will be populated in the $^{14}N(\alpha,{}^{2}He)^{16}N$ reaction with configurations $\left[(^{14}N(g.s.,1^{+}) \otimes (d_{5/2})^{2}_{4}\right]_{J}$

and with J = 3, 4 or 5. The spectrum of this reaction shown in Fig. IV-7b appears to confirm this expectation. The ^{16}N levels observed at 6.62 and 7.69 MeV (an unresolved doublet) contain the L = 4 strength which has split into three components. Due to the poor energy resolution and the small splitting, relative assignments of the $J^{\pi} = 3^+, 4^+, 5^+$ components to the observed peaks cannot be made. Transitions to the 2^-, g.s. of ^{16}N and the 3^- state at 0.30 MeV, though unresolved, can be interpreted as populating the configurations $\left[^{14}N(1^+) \otimes p_{1/2}d_{5/2}\right]_{2^-,3^-}$, respectively. In addition to these strongly populated states in ^{16}N, transitions to two states at 5.25 and 5.74 MeV are observed with moderate strength.

$\underline{^{15}N(\alpha,{}^2He)^{17}N}$ $(Q_0 = -19.92$ MeV)

Since the neutron 1p-shell is full in ^{15}N, no p orbits can be populated with the $(\alpha,{}^2He)$ reaction on this target. Figure IV-8a shows a spectrum from this reaction at $\theta_{lab} = 13^o$. As can be seen, the only states strongly populated are a doublet at 3.13 and 3.63 MeV. In the simple picture which we are applying to the states populated by the $(\alpha,{}^2He)$ reaction, the configuration of these states is expected to be $\left[^{16}O(0^+)p_{1/2}^{-1} \otimes (d_{5/2})^2_4\right]_{7/2^-,9/2^-}$.
In (Aj77) the state at 3.13 MeV has been assigned as $J^{\pi} = 7/2^-$ and the state at 3.63 MeV has been tentatively assigned as $J^{\pi} = 9/2^-$. The (2J+1) rule applied to the differential cross sections for the transitions to these states suggests the same spin assignments. Furthermore, this agreement for states with known spin and parity

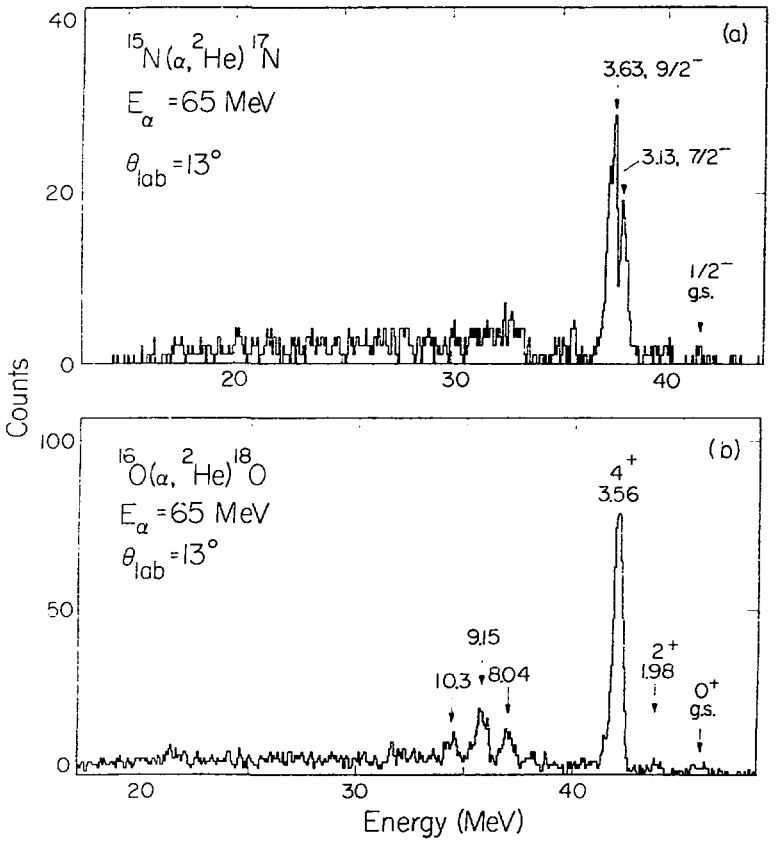

Fig. IV-8. ^{2}He energy spectra from the $(\alpha,{}^{2}He)$ reaction at E_α = 65 MeV and θ_{lab} = 13° on a) ^{15}N and b) ^{16}O.

lends credence to the tentative $J^{\pi} = 7/2^-$ and $9/2^-$ assignments made for the 6.74 and 7.35-MeV levels populated in the $^{13}C(\alpha,{}^2He)$ ^{15}C reaction.

$^{16}O(\alpha,{}^2He)^{18}O$ (Q_0 = -16.11 MeV)

Figure IV-8b shows a spectrum from this reaction at θ_{lab} = 13°. The only strongly populated state in ^{18}O is the well known 4^+ state at 3.56 MeV. The $(d_{5/2})^2_4$ character of this state has been confirmed by shell-model calculations (Ku66, Ka69) as well as by a recent study of the $^{16}O(^{10}B,{}^8B)^{18}O$ reaction (Ha78). It is interesting to note that, although the 0^+, g.s. and the 2^+ state at 1.98 MeV in ^{18}O are also known to have $(d_{5/2})^2$ configurations, the cross sections for the transitions to these states in the $(\alpha,{}^2He)$ reaction are smaller by a factor of about 50 than that to the 4^+, 3.56-MeV state due to the angular momentum mismatch, the angular momentum coupling coefficients and the statistical weighting factor. States with moderate strength are observed at 8.04, 9.15 and 10.3 MeV. The overall resemblance between the ^{18}O spectrum and that from the $^{18}O(\alpha,{}^2He)^{20}O$ reaction (see below) suggests that corresponding transitions involve similar transfers.

$^{40}Ca(\alpha,{}^2He)^{42}Ca$ (Q_0 = -8.46 MeV)

Figure IV-9a presents a spectrum from this reaction at θ_{lab} = 15°. The only strongly populated peak corresponds to transitions to the 6^{+}, 3.19 MeV-state in ^{42}Ca. This state is known to be a 2n state of $(f_{7/2})^{2}_{6}$ character (Ka69). Transitions to the other members of the $(f_{7/2})^{2}$, T = 1 multiplet with $J^{\pi} = 0^{+}$, 2^{+}, and 4^{+} at 0., 1.52 and 2.75 MeV, respectively, were also observed, but with a reduced cross section. Since simple shell-model calculations (see Sec. b) predict a state with an $(f_{7/2}f_{5/2})_{6}$ configuration at 7.23 MeV in ^{42}Ca, the state observed at 7.40 MeV is a candidate for such a state.

$^{38}Ar(\alpha,{}^{2}He)^{40}Ar$ $(Q_{0} = -11.83$ MeV)

Since ^{38}Ar has the same closed shell neutron configuration as ^{40}Ca, the spectra of the $(\alpha,{}^{2}He)$ reaction on this target should be very similar to those observed on the ^{40}Ca target, as is demonstrated in Fig. IV-9b. The excitation energies as well as the observed relative strengths of the transitions to the $J^{\pi} = 6^{+}$, 4^{+}, 2^{+}, 0^{+} members of the $(f_{7/2})^{2}$ multiplet are almost identical to those observed in the $^{40}Ca(\alpha,{}^{2}He)^{42}Ca$ reaction. The 3.47-MeV level in ^{40}Ar has previously been observed in a study of the $^{38}Ar(t,p)^{40}Ar$ reaction (F175) where a tentative $J^{\pi} = 6^{+}$ assignment has been made. Certainly, the analogous ^{42}Ca and ^{40}Ar spectra observed in the present study help establish such an assignment. The state observed at 9.0 ± 0.1 MeV and the broad state (or

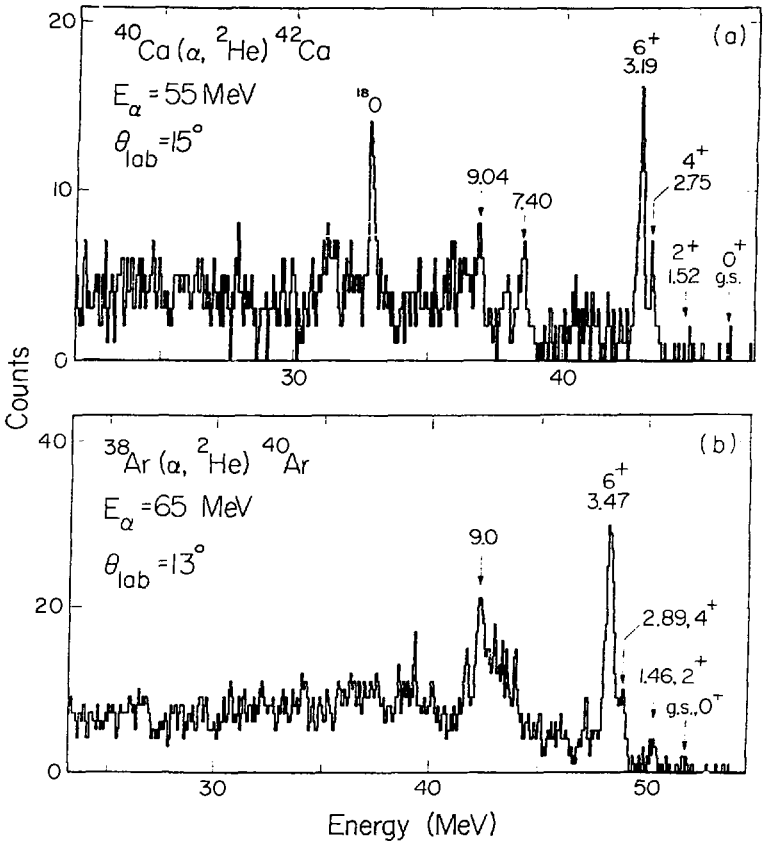

Fig. IV-9. ^{2}He energy spectra from the (α, ^{2}He) reaction on a) ^{40}Ca at E_α = 55 MeV and θ_{lab} = 15° and b) ^{38}Ar at E_α = 65 MeV and θ_{lab} = 13°.

unresolved states) between 7.5 and 9.0 MeV in ^{40}Ar probably correspond to the states observed in ^{42}Ca at 7.40 and 9.04 MeV, respectively.

$^{36}Ar(\alpha,{}^{2}He)^{38}Ar$ (Q_0 = -7.67 MeV)

Figure IV-10 shows a spectrum from this reaction at θ_{lab} = 13°. All observed peaks below 7.5 MeV could be identified with known states of ^{38}Ar (Ko76). Again, the transition to the 6^{+} state has the largest cross section. Although the $J^{\pi} = 6^{+}$ assignment of the 6.41-MeV state has recently been established in a study of the $^{24}Mg(^{16}O,2p\gamma)$ reaction (Dr76), the present experiment confirms its $(f_{7/2})^{2}_{6}$ character. The 5^{-} states at 4.59 and 5.66 MeV are of dominant $(d_{3/2}f_{7/2})_{5}$ character (En69). This splitting of the 5^{-} strength in ^{38}Ar has been successfully described by the shell-model calculations of Engelbertink and Glaudemans (En69). The states observed at higher excitation energies could not definitely be identified as ^{38}Ar states. Their slightly different kinematic behavior indicates that they might originate from an unidentified target contaminant.

$^{32}S(\alpha,{}^{2}He)^{34}S$ (Q_0 = -8.24 MeV)

A spectrum from this reaction on an Sb_2S_3 target is presented in Fig. IV-11. The known 5^{-} state at 5.69 MeV and a previously unknown state in ^{34}S at 8.45 MeV are preferentially populated.

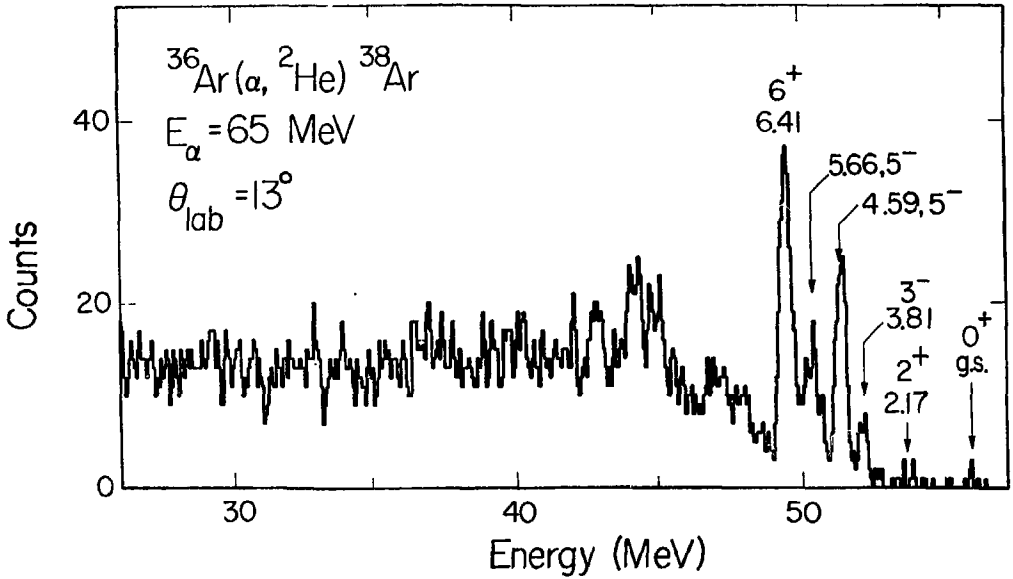

XBL 7711-11346

Fig. IV-10. ^{2}He energy spectrum from the $^{36}Ar(\alpha,{}^{2}He)^{38}Ar$ reaction at E_α = 65 MeV and θ_{lab} = 13°.

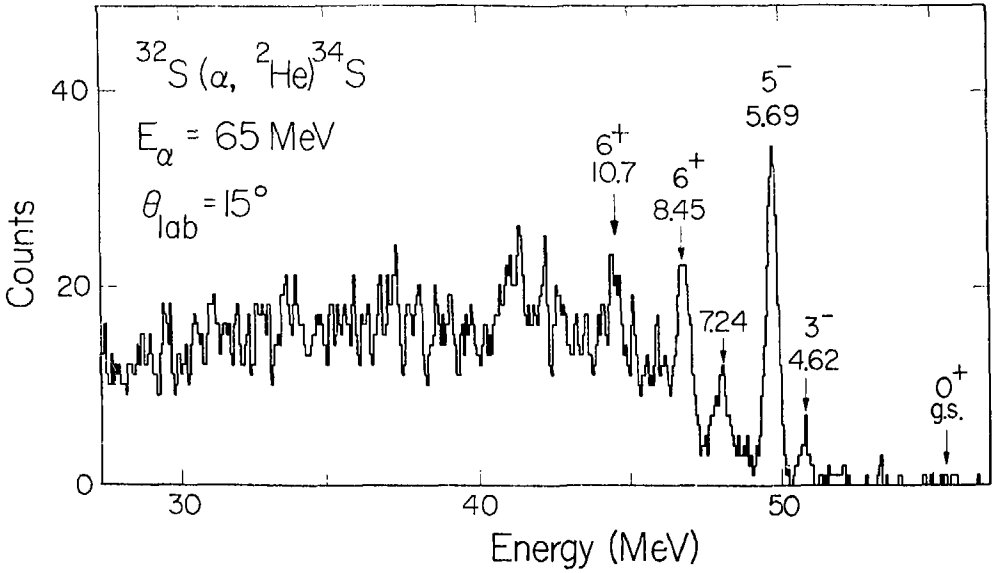

XBL 7711-11349

Fig. IV-11. ^{2}He energy spectrum from the $^{32}S(\alpha,{}^{2}He)^{34}S$ reaction at E_α = 65 MeV and θ_{lab} = 15°.

Furthermore, the known 3^- state at 4.62 MeV and two previously unknown states at 7.24 and 10.7 ± 0.1 MeV are populated with moderate strength. The peaks seen at higher excitation energies could not definitely be identified as transitions to ^{34}S levels.

The 5^- state in ^{34}S is known to be of predominant $(d_{3/2}f_{7/2})$ character, since the (d,p) reaction on ^{33}S (which, in its g.s., has a $\left[^{32}S(0^+) \otimes d_{3/2}\right]_{3/2^+}$ configuration) shows a strong $\ell = 3$ transfer to the 5.69 MeV state. The state at 8.45 MeV is most likely of $(f_{7/2})^2_6$ character which is in agreement with simple shell-model calculations (see Sec. b). It should be noted that in a study of the $^{32}S(t,p)^{34}S$ reaction (Cr73), the $J^\pi = 4^+$, 2^+, and 0^+ members of the $(f_{7/2})^2$ multiplet were identified at 8.42, 7.80 and 5.86 MeV, respectively, though the 6^+ member was not observed. Simple shell-model calculations (see Sec. b) indicate that the state observed at 10.7 MeV could be of $(f_{7/2}f_{5/2})_6$ character, but no definite assignment can be made based on this limited survey.

<u>$^{28}Si(\alpha,{}^2He)^{30}Si$</u> ($Q_0$ = -9.21 MeV)

A spectrum from the $(\alpha,{}^2He)$ reaction at $\theta_{lab} = 12^o$ on this closed $d_{5/2}$ subshell target nucleus is shown in Fig. IV-12a. The known (En78) 3^- and 5^- states at 5.49 and 7.04 MeV, respectively, and two states at 8.95 and 10.67 MeV are substantially populated. Recently, de Meijer et al. (De77) published a study of this reaction at E_α = 65 MeV, and our excitation energies for the observed levels

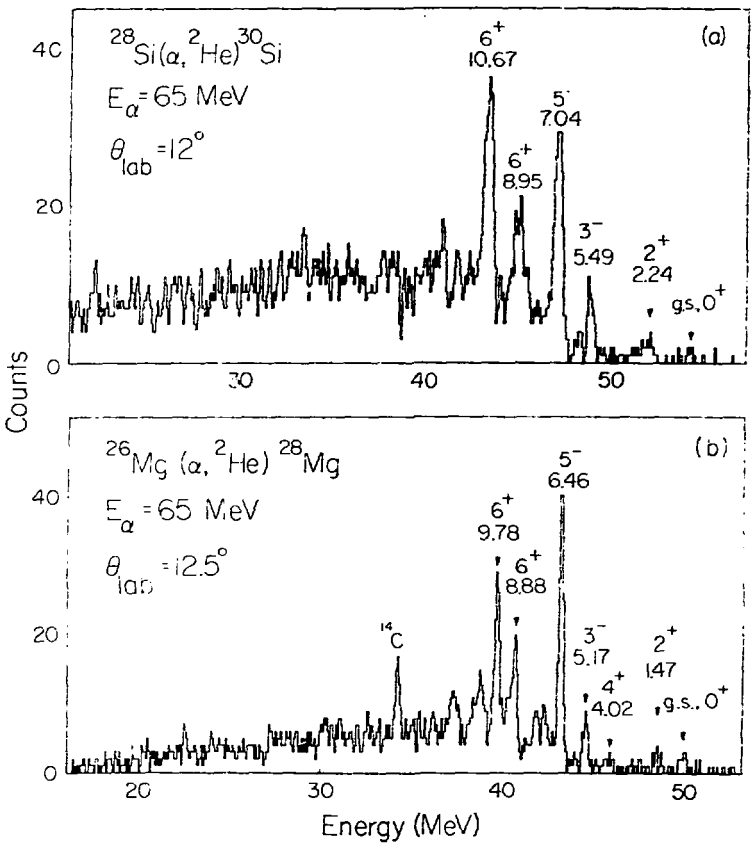

Fig. IV-12. ^{2}He energy spectra from the (α,^{2}He) reaction at E_α = 65 MeV on a) ^{28}Si at θ_{lab} = 12° and b) ^{26}Mg at θ_{lab} = 12.5°.

agree with their values within errors. They obtained detailed angular distributions for the $^{28}Si(\alpha,{}^{2}He)^{30}Si$ reaction which were analyzed with DWBA calculations, using optical model parameters from (α,d) data analysis and taking deuteron parameters for ^{2}He. Their analysis established that the ^{30}Si levels at 5.49, 7.04, 8.95 and 10.67 MeV possess 2n configurations of $(2s_{1/2}f_{7/2})_3$, $(d_{3/2}f_{7/2})_5$, $(f_{7/2})^2_6$, and $(f_{7/2}f_{5/2})_6$ character, respectively. The presence of an $(f_{7/2}f_{5/2})_6$ configuration so close to the $(f_{7/2})^2_6$ configuration in ^{30}Si is somewhat surprising, but can be explained by the fact that the experimental $f_{7/2}$ - $f_{5/2}$ single-particle states in ^{29}Si are only separated by 2.57 MeV, whereas typically those two single-particle energies differ by about 3 to 4 MeV throughout the rest of the sd shell (En78).

$\underline{^{26}Mg(\alpha,{}^{2}He)^{28}Mg}$ $(Q_0 = -13.35$ MeV)

Since ^{26}Mg has the same closed $d_{5/2}$-subshell neutron configuration as ^{28}Si, the $(\alpha,{}^{2}He)$ spectra on these two targets are expected to be very similar. Comparing Figs. IV-12a and b confirms this expectation. The states observed at 6.46, 8.88 and 9.78 MeV were previously unknown. In analogy with the population of known states in ^{30}Si, these states can be preliminarily assigned as being of $(d_{3/2}f_{7/2})_5$, $(f_{7/2})^2_6$ and $(f_{7/2}f_{5/2})_6$ character, respectively.

$^{29}Si(\alpha,{}^2He)^{31}Si$ (Q_0 = -11.10 MeV)

In its g.s., ^{29}Si can be described as $\left[{}^{28}Si(0^+) \otimes 2s_{1/2}\right]_{1/2^+}$ and thus one can expect the $(\alpha,{}^2He)$ reaction on ^{29}Si to populate the same 2n states as on a ^{28}Si (or ^{26}Mg) target, coupled to the $2s_{1/2}$ neutron. A spectrum from the $^{29}Si(\alpha,{}^2He)\,^{31}Si$ reaction is shown in Fig. IV-13. Three previously unknown states in ^{31}Si at 5.00, 5.41 and 8.27 MeV are preferentially populated. The doublet at 5.00 and 5.41 MeV most probably arises from the coupling of the $(d_{3/2}f_{7/2})_5$ configuration to the $s_{1/2}$ neutron of the ^{29}Si core, so that these two states presumably have J^π assignments of $9/2^-$ and $11/2^-$. An assigment via the simple (2J+1) dependence of the cross section could not be made, since at most angles this doublet is unresolved. The state at 8.27 MeV can possibly be explained as an unresolved doublet of either

$$\left[\left\{{}^{28}Si(0^+)2s_{1/2}\right\}_{1/2} \otimes (f_{7/2})^2_6\right]_{11/2^+,13/2^+} \qquad \text{or}$$

$$\left[\left\{{}^{28}Si(0^+)2s_{1/2}\right\}_{1/2} \otimes (f_{7/2}f_{5/2})_6\right]_{11/2^+,\ 13/2^+} \qquad \text{configuration;}$$

the separation in energy of the 8.27-MeV states relative to the centroid of the 5.00 and 5.41 MeV states, when compared to the spectra from the $(\alpha,{}^2He)$ reaction on ^{28}Si and ^{26}Mg, leads to a preference for the latter configuration

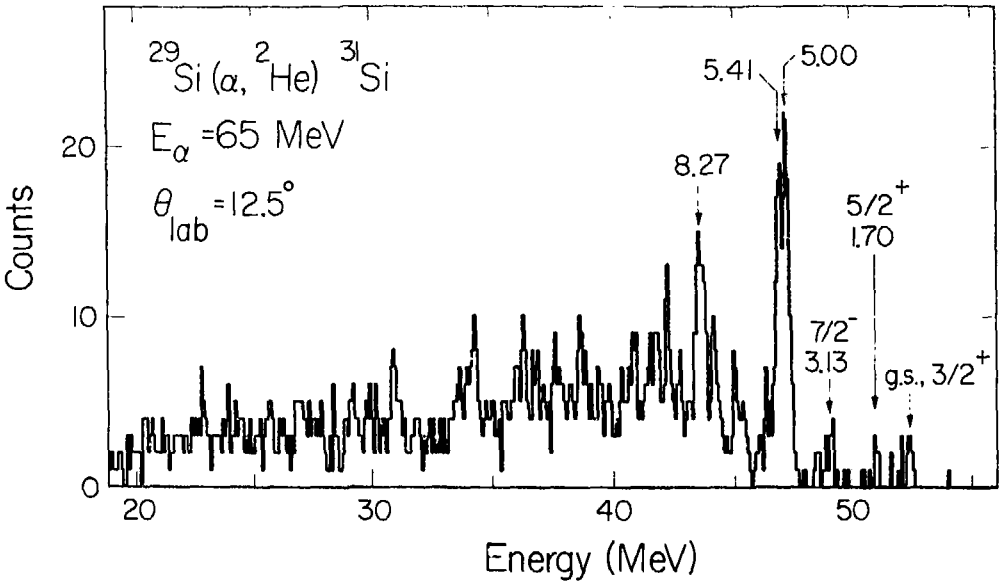

XBL 7711-11335

Fig. IV-13. ^{2}He energy spectrum from the ^{29}Si(α,^{2}He)^{31}Si reaction at E_α = 65 MeV and θ_{lab} = 12.5°.

^{24}Mg(α,^{2}He)^{26}Mg (Q_0 = -9.87 MeV)

Figure IV-14a presents a spectrum from this reaction of θ_{lab} = 12°. Besides moderate population of the known 4^+ state (En78) at 5.47 MeV, two previously unknown states at 8.62 and 11.23 MeV are strongly populated. From the systematics discussed in Sec. b, it follows that these two states are presumably populated by $(d_{3/2}f_{7/2})_5$ and $(f_{7/2})^2_6$ transitions, respectively.

^{22}Ne(α,^{2}He)^{24}Ne (Q_0 = -14.23 MeV)

Figure IV-14b shows a spectrum from this reaction at θ_{lab} = 13°. All states observed above the 2^+, 3.87-MeV level were previously unknown. ^{24}Ne states at 6.36 and 8.15 MeV and a broad level at 11.35 ± 0.15 MeV are strongly populated. In addition, a state at 9.88 MeV is observed with moderate strength. Although ^{22}Ne has the same neutron configuration as ^{24}Mg, the spectra of the final nuclei ^{24}Ne and ^{26}Mg are not as similar as has been previously observed in populating the pairs of isotones ^{28}Mg vs. ^{30}Si or ^{40}Ar vs. ^{42}Ca. This can perhaps be related to the fact that, unlike the ^{26}Mg, ^{28}Si, ^{38}Ar, and ^{40}Ca targets, those of ^{22}Ne and ^{24}Mg do not have closed neutron shells or subshells. As will be shown from the systematics (Sec. b), the state at 8.15 MeV in ^{24}Ne is probably of $(d_{3/2}f_{7/2})_5$ character and the broad state at 11.35 MeV is possibly of $(f_{7/2})_6$ character, with the latter suggestion being quite tentative. The state of 6.36 MeV cannot be

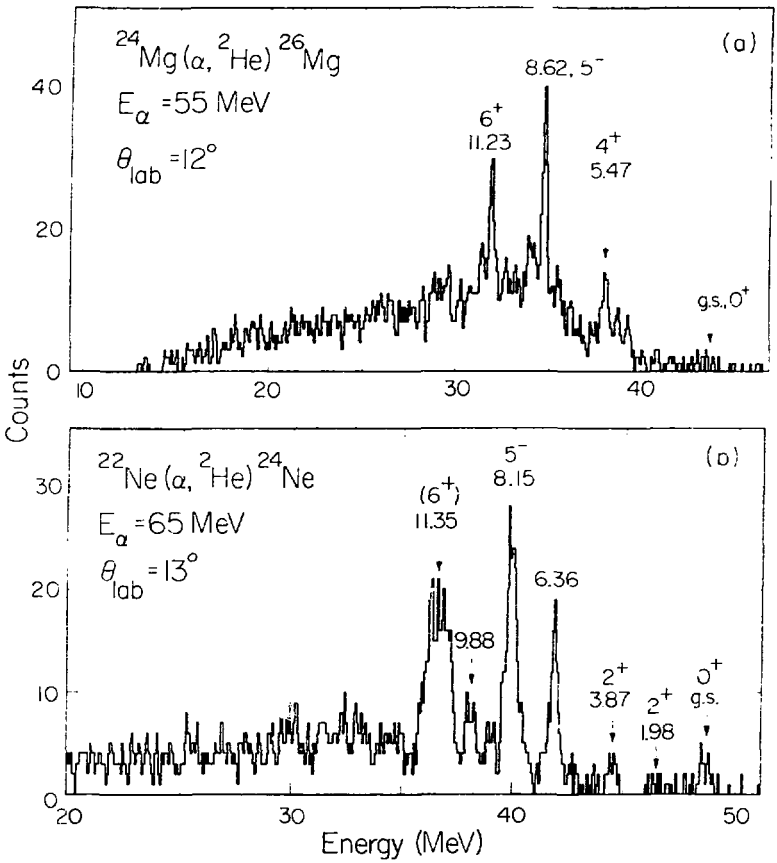

Fig. IV-14. ^{2}He energy spectra from the (α, ^{2}He) reaction on a) ^{24}Mg at E_α = 55 MeV and θ_{lab} = 12° and b) ^{22}Ne at E_α = 65 MeV and θ_{lab} = 13°.

assigned in the present study, it is either the counterpart of the 5.47 MeV state in ^{20}Ne or of $(s_{1/2}d_{3/2})_3$ character. In the latter case, the above [illegible] of an unassigned peak in the ^{20}Ne spectrum is possible.

$\underline{^{20}Ne(^{2}He,^{2}He)^{22}Ne}$ $(Q_0 = -11.17$ MeV)

A spectrum from this reaction at $\theta_{lab} = 12.5°$ is shown in Fig. IV-15a. In addition to the relatively strong population of a doublet at 9.19 and 9.44 MeV, many states are populated with moderate strength in this reaction. The systematics of the [illegible] states, [illegible] in Sec. b, indicates that one of the states of the doublet is likely to be of $(d_{5/2}f_{7/2})_5$ character, but a definite assignment is not justified.

$\underline{^{18}O(^{2}He,^{2}He)^{20}O}$ $(Q_0 = -10.74$ MeV)

A spectrum from this reaction is shown in Fig. IV-15b. In addition to the transitions to the known 0^+, 2^+ and 4^+ states (Aj72) at 0., 1.67 and 3.57 MeV, respectively, previously unknown states at 7.70, 8.78 and 10.2 ± 0.1 MeV are populated in ^{20}O. Although configurations of $(d_{5/2}d_{3/2})_4$ and $(d_{3/2}f_{7/2})_5$ are expected in this high excitation region, no assignments can be made in this limited survey. Although ^{20}O has the same neutron configuration as ^{22}Ne, the spectra from the $(\alpha,{}^{2}He)$ reaction populating these

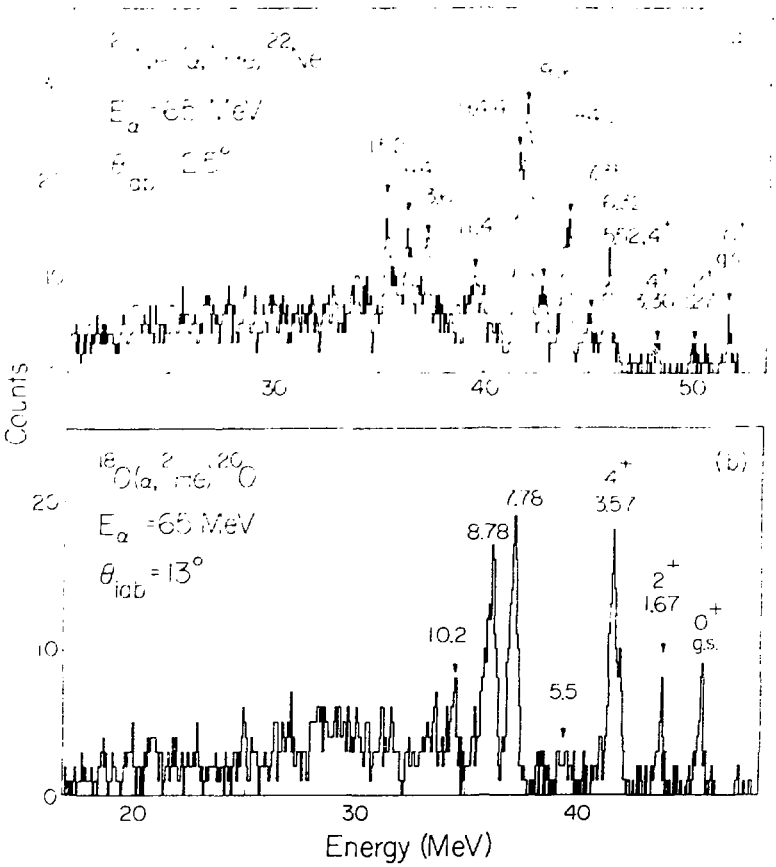

Fig. IV-15. ^{2}He energy spectra from the (α, ^{2}He) reaction at E_α = 65 MeV on a) ^{20}Ne at θ_{lab} = 12.5° and b) ^{18}O at θ_{lab} = 13°.

XBL 7711-11599

nuclei again lack the pronounced similarities observed in reactions producing isotones higher in the sd shell.

A summary of the excitation energies for the $(d_{3/2}f_{5/2})_{5^-}$ and $(f_{7/2})^2_{6^+}$ states observed in the $(\alpha, {}^2He)$ reactions is given in Table IV-3.

b. Shell-model calculations and systematics

Predicated on the observed selectivity of the $(\alpha, {}^2He)$ reaction, simple shell-model calculations have been carried out in order to interpret further the character of the strongly populated states. The $T_z = 0$ target nuclei from ^{24}Mg to ^{40}Ca were each assumed to be an inert core and the two neutrons were allowed to occupy the valence orbits in the 2sld and 1f2p shells.

The single-particle energies ε_j were taken to be the separation energies of the single particle levels in the $A_{core} + 1$ nucleus:

$$\varepsilon_j = E(A+1, J=j) - E(A) \qquad \text{(IV-14)}$$

where $A = A_{core}$. From the dominant appropriate ℓ transfers in single-nucleon transfer reactions (En78), the locations of the single-particle levels were determined.

The excitation energy of the 2n states were calculated according to

$$E_x(A+2, j_1 j_2 J) = \varepsilon_{j_1} + \varepsilon_{j_2} + \langle j_1 j_2 | V | j_1 j_2 \rangle_J + B_{2n}(A+2, g.s.), \qquad \text{(IV-15)}$$

where B_{2n} and $\langle j_1 j_2 | V | j_1 j_2 \rangle_J$ are the 2n binding energy and the two-body matrix element (TBME), respectively. The calculated

Table IV-3 Excitation energies for $(d_{3/2}f_{7/2})_{5^-}$ and $(f_{7/2})^2_{6^+}$ states observed in the $(\alpha,{}^2He)$ reactions.

Final Nucleus	Beam Energy (MeV)	$(d_{3/2}f_{7/2})_{5^-}$ E_x (MeV)	$(f_{7/2})^2_{6^+}$ E_x (MeV)
^{24}Ne	65	8.15	11.35
^{26}Mg	55	8.62	11.23
^{26}Mg	65	6.46	8.88
^{30}Si	65	7.04	8.95
^{34}S	65	5.69	8.45
^{38}Ar	65		6.41
^{40}Ar	65		3.47
^{42}Ca	55		3.19

TBME's of Kuo and Brown (Ku66) have been applied except for the $(0g_{7/2})^1(1f_{7/2})^3_{3,5}$ cases, where the values empirically evaluated by Arnd (Ar66) have been used, since they give much better fits to the known $J^\pi = 3^-$ and 5^- states. Those TBME's not listed by Kuo and Brown have been calculated from the modified surface delta interaction with the A = 37, 39 parameters listed in (Ma70).

When several configurations yielded states with the same spin J, the configuration interaction was taken into account by diagonalizing the Hamiltonian matrix

$$H_{ij} = (\varepsilon_{j_{1i}} + \varepsilon_{j_{2i}})\delta_{ij} + \langle j_{1i} j_{2i} | V | j_{1j} j_{2j} \rangle_J + \delta_{2n}(A+2,g.s.)\,\delta_{ij}$$

Due to the difference in single particle energies, there usually is a large gap in the energy between the second and the higher pure configurations. For this reason, in the present calculations these higher configurations were neglected, which reduced the calculation of the energy levels to simple 2 × 2 matrix diagonalizations.

Figure IV-16 compares the calculations for ^{30}Si, ^{34}S and ^{42}Ca with the energy spectra observed in the present study. Except for the energies of the g.s., which are very sensitive to the limitations of the present approach, the calculations are in good agreement with experiment, especially so for the ^{30}Si nucleus, and are additional support for the assignments suggested in the previous section.

Another shell-model approach is given in the Bansal-French (BF) weak-coupling method (Ba64, Za65, Be72, Sh74) for computing the energies of particle-hole states. In studies of the (α,d) reaction on

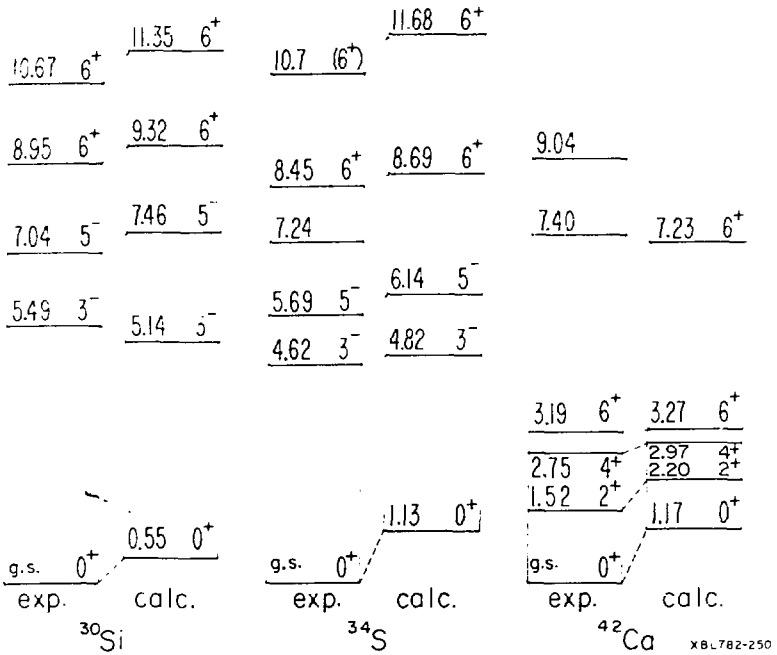

Fig. IV-16. Comparison of the calculated and experimental level schemes of ^{30}Si, ^{34}Si, and ^{42}Ca. Above the ground states, only the states observed in these experiments are presented.

many sd-shell nuclei (Ri66, Lu69, Na75, De76), a linear dependence of the binding energy B_{np} of the np pair in the observed $(f_{7/2})^2_7$ states versus the mass number of the final nucleus has been observed and successfully explained by the BF method. This method will be discussed below and the binding energies of the 2n states will be calculated and compared with the experimental data.

The total energy of a nucleus A_0+p-h with p particles and h holes relative to a closed shell nucleus A_0 is given by:

$$E(A_0+p-h) = E(A_0)+E(p)-E(h)+ \langle ph | V_{ph} | ph \rangle \quad , \qquad \text{(IV-17)}$$

where E(p) and E(h) are the energies of p particles and h holes relative to $E(A_0)$. In the model of Bansal and French, a weak interaction is assumed between the particles and holes such that the values of E(p) and E(h), which include the interactions of the particles and holes among themselves, can be obtained empirically from the binding energies of the nuclei A_0, A_0+p and A_0-h by

$$E(p) = E(A_0+p) - E(A_0) \qquad \text{(IV-18)}$$

$$E(h) = E(A_0) - E(A_0-h) \ . \qquad \text{(IV-19)}$$

In (IV-17) the last term represents the interaction energy between the particles and the holes which was assumed by Bansal and French to be of the following form:

$$\langle ph|V_{ph}|ph\rangle = -pha + b\,\vec{t}_p\cdot\vec{t}_h \quad , \qquad \text{(IV-20)}$$

where a is the two-body matrix element $\langle j_p j_h^{-1}|V_{12}|j_p j_h^{-1}\rangle_{JT}$ averaged over all allowed values of J and T, and b is the separation of the center of gravity of the T = 0 and T = 1 states.

By inserting (IV-16 to 20) in (IV-17), one obtains for the energy of the nucleus $A = A_0+p-h$

$$E(A,T,T_z) = E(A_0+p,T_p,T_{zp}) + E(A_0-h,T_h,T_{zh}) - E(A_0,0,0)$$

$$- pha + b\frac{1}{2}\left[T(T+1) - T_p(T_p+1) - T_h(T_h+1)\right] + \varepsilon_c \quad , \qquad \text{(IV-21)}$$

where ε_c is the Coulomb interaction energy between the particles and the holes, which was not included in V_{ph}.

The 2n binding energy B_{2n} of states with dominant $(f_{7/2})^2$ character in a nucleus A near the closed-shell nucleus ^{40}Ca can readily be obtained from (IV-21) using $E(A_0) = E(^{40}\text{Ca g.s.})$, $E(A_0+p) = E\left[^{42}\text{Ca}(f_{7/2})^2\right]$, $E(A_0-h) = E(A-2,\text{g.s. } 0^+)$, p = 2, h = 40-(A-2) and $\varepsilon_c = 0$, one then finds:

$$B_{2n}\left[A(f_{7/2})^2_6\right] = B_{2n}\left[^{42}\text{Ca}(f_{7/2})^2_6\right] + 2(42-A)a - b(T-1) \qquad \text{(IV-22)}$$

$$B_n\left[A(f_{7/2})^2_0\right] = B_{2n}\left[^{42}\text{Ca}(f_{7/2})^2_0\right] + 2(42-A)a - b(T-1) \qquad \text{(IV-23)}$$

In a similar fashion, both B_{2n} for states with $(d_{3/2}f_{7/2})_5$ character as well as the ln binding-energy B_n of $f_{7/2}$ single-particle states can be derived:

$$B_{2n}\left[A(d_{3/2}f_{7/2})_5\right] = B_{2n}\left[^{34}S(d_{3/2}f_{7/2})_5\right] + 2(34-A)a - b(T-1) \quad \text{(IV-24)}$$

$$B_n\left[A(f_{7/2})\right] = B_n\left[(^{41}Ca(f_{7/2})\right] + 1(41-A)a \quad \text{(IV-25)}$$

In Fig. IV-17, the experimental B_{2n} values of the $(f_{7/2})^2_6$ and $(d_{3/2}f_{7/2})_5$ states from the present study are plotted versus A of the final nucleus. In addition, the experimental B_{2n} values (Ma70) of states with the $(f_{7/2})^2$ configuration as well as the B_n values (Ma70) of $f_{7/2}$ single-neutron states relative to $J^{\pi} = 0^+$ nuclei are also indicated in Fig. IV-17. The solid lines represent B_{2n} and B_n calculated using the common values a= -0.30 MeV and b = 2.6 MeV.

The observed linear dependence of B_{2n} on A is well reproduced by the BF model. This indicates that a is essentially independent of A, as assumed in (IV-22 to 25). As Sherr et al. (Sh74) pointed out, this fact is remarkable and somewhat surprising, since a contains different particle-hole interactions depending on A. For the $(f_{7/2})^2$ states, for instance, in the case of ^{38}Ar a contains only $(f_{7/2}d^{-1}_{3/2})$ interactions, whereas, in ^{26}Mg in addition the $(f_{7/2}s^{-1}_{1/2})$ and $(f_{7/2}d^{-1}_{5/2})$ interactions are included. Although it is known

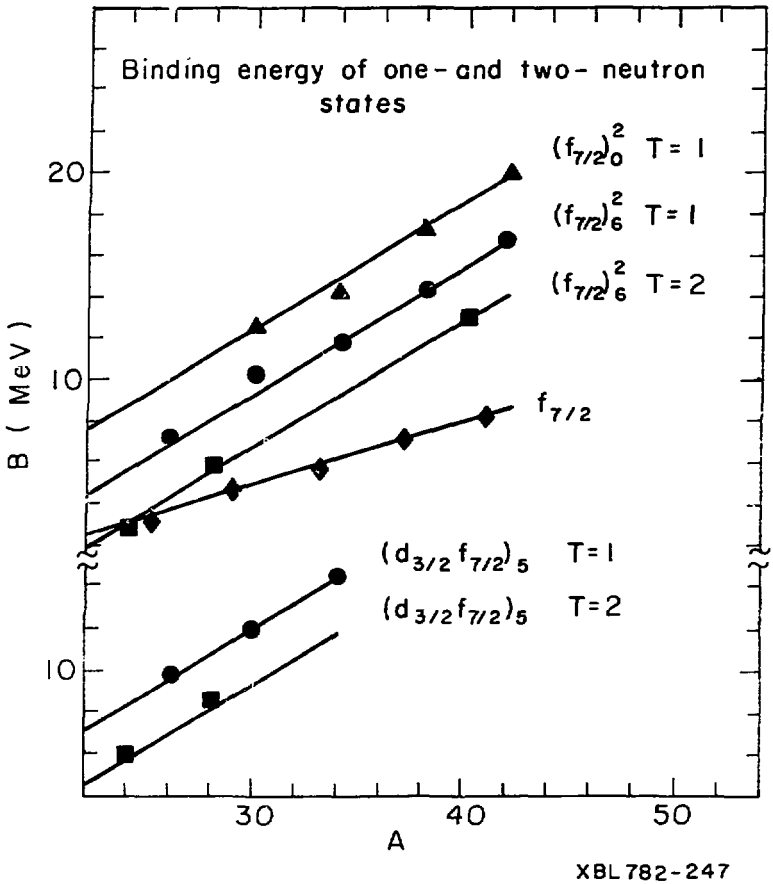

Fig. IV-17. Binding energies B for one- and two-neutron states possessing several different configurations as a function of the mass of the final nucleus A.

(Ku68) that these interaction energies differ substantially from one another, the averaging is believed to smooth out any differences.

The fact that the same value of a fits the states with $(f_{7/2})^2_0$ and $(f_{7/2})^2_6$ configurations is expected in the BF model, since they involve the same particle-hole interactions. The differences in energy of these two states is a result of the particle-particle interaction, which is included in E(p) [(IV-18)] and which does not affect the particle-hole interaction. On the other hand, one would expect that the value of a would differ for the $(f_{7/2})^2$ states vs. the $(d_{3/2}f_{7/2})$ states, since the latter also involve interactions of a $d_{3/2}$ particle with the various holes. The fact that the same value of a fits both configurations could be fortuitous or could be again the result of averaging. It is interesting to note that this value for a of -0.30 MeV has also been found in a similar analysis (Sh74) of the binding energies B_{np} of np states with $(f_{7/2})^2$ character. Sherr et al. (Sh74) also obtained b = 2.88 MeV which compares well with our value of b = 2 60 MeV. These values are in good agreement with those of Bansal and French (Ba64) and Zamick (Za65) who found a = -0.25 MeV, b = 2.9 MeV and a = -0.30 MeV, b = 2.90 MeV, respectively, for nuclei in the region of ^{40}Ca.

c. Angular distributions

No detailed angular distributions have been measured for the $(\alpha,{}^2He)$ reactions, except for the $^{12}C(\alpha,{}^2He)\,^{14}C$ reaction at E_α = 65 MeV. These results are presented in Fig. IV-13. Because these data were not collected in the event-mode, only ^2He energy

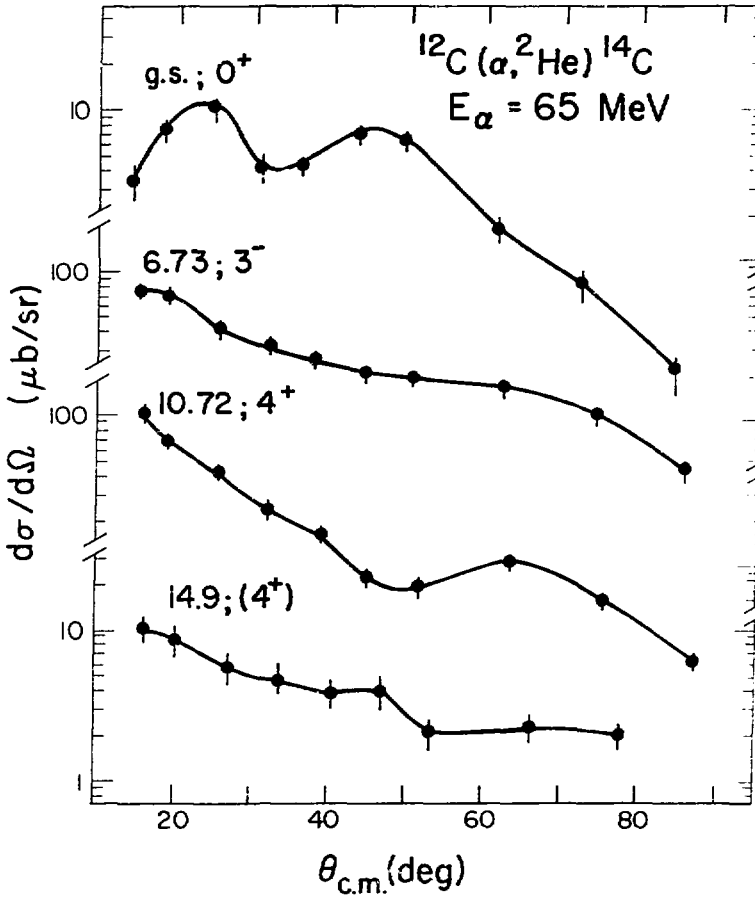

XBL 798-2739

Fig. IV-18. Angular distributions from the $^{12}C(\alpha,{}^{2}He)^{14}C$ reaction at E_α = 65 MeV for $0.4 < \varepsilon < 1.0$ MeV. Statistical error bars are shown. The solid curves are meant to guide the eye.

spectra, but no projected proton energy spectra are available. The differential cross sections were therefore calculated with the solid angle computation program SOLJAC (see Appendix). In a later experiment, the measurement of the $\theta_{lab} = 15^{o}$ data was repeated in the event-mode and cross sections were determined by integrating the projected spectra between $\varepsilon = 0.4$ and 1.0 MeV. The angular distributions from the old data were then scaled to the new measurement.

Some attempts have been made to fit the shape of these distributions with DWBA. However, no satisfactory agreement with the data was obtained. A more successful DWBA analysis has been reported for the $^{28}Si(\alpha,{}^{2}He)^{30}Si$ reaction (De77) and shows that the reaction mechanism can indeed be interpreted in terms of a direct two-nucleon transfer reaction theory.

5. The $(d,{}^{2}He)$ reaction

Investigation of the $(d,{}^{2}He)$ charge-exchange reaction is of particular interest. Such studies should be a useful complement to other charge-exchange reactions producing neutron-excess nuclei, such as the (n,p), $(t,{}^{3}He)$ and heavy-ion induced reactions, many of which have experimental problems associated with their general application. For example, high-energy neutron beams have poor energy resolution and low intensities, whereas triton beams are currently only available at moderate energies (<25 MeV). Though heavy-ion reactions (e.g.,$({}^{7}Li,{}^{7}Be)$) are being increasingly employed, the presence of bound excited states of the ejectile frequently complicates the interpretation of the spectra. Since intense high energy deuteron beams

are readily available and there are no bound states in ^{2}He, the (d,^{2}He) reaction was investigated for its promise as a charge-exchange reaction.

From the theoretical point of view, the (d,^{2}He) reaction differs from charge-exchange reactions induced by spin 1/2 projectiles, such as the (n,p) reaction, in that the latter reaction may proceed by both spin-flip (S = 1) and non-spin-flip (S = 0) transitions, whereas the (d,^{2}He) reaction is always restricted to spin-flip transitions. Thus, the (d,^{2}He) reaction is only governed by the $V_{11}(\vec{\sigma}\cdot\vec{\sigma})(\vec{\tau}\cdot\vec{\tau})$ part of the effective nuclear interaction, whereas in the (n,p) reaction in addition the $V_{01}(\vec{\tau}\cdot\vec{\tau})$ part can contribute to some transitions. Therefore, every state populated in the (d,^{2}He) reaction should also be seen in the corresponding (n,p) reaction; on the other hand, if transitions, which are observed strongly in the (n,p) reaction, are unobserved or only weakly observed in the (d,^{2}He) reaction, this may indicate that they are favored with S = 0 but unfavored with S = 1. Thus, by comparing the levels populated in the same final nucleus by these two reactions, one may learn something about the character of these final states.

Owing to the scarcity of high energy (n,p) data which could be used for comparative purposes, the (d,^{2}He) reaction was initially studied at E_d = 55 MeV on the T_z = 0 targets ^{6}Li, ^{10}B and ^{12}C producing T_z = 1 final nuclei, since in these cases the energy spectra can also be directly compared with those from reactions such as (p,n) which produce the T_z = -1 mirror nuclei.

a. Energy spectra

Figures IV-19 to 21 show representative spectra from the $(d,{}^2He)$ reaction at E_d = 55 MeV on targets of ^6Li, ^{10}B and ^{12}C. They will be discussed and compared with existing data from other charge-exchange reactions such as (n,p) and $(t,{}^3He)$. In addition, since these are $T_z = 0$ targets, spectra of the (p,n) and $({}^3He,t)$ reactions populating the mirror nuclei can also be compared to these $(d,{}^2He)$ results.

$^6Li(d,{}^2He)^6He$ (Q_0 = -4.95 MeV)

Although the ^6He nucleus (Aj74) has been studied with particle-transfer as well as charge-exchange reactions (examples of the latter are the $^6Li(n,p)^6He$ reaction at E_n = 14 MeV (Me72) and the $^6Li(t,{}^3He)^6He$ reation at E_t = 22 MeV (St71)), only two states have clearly been observed so far, namely the g.s., 0^+, and an excited state at 1.80 MeV with $J^\pi = (2)^+$. Weak evidence for possible broad states at 13.4, 15.3 and 23.2 MeV has been reported in some reactions (Aj74), but these states have not been seen in any charge-exchange reaction.

At 55 MeV bombarding energy, the $^6Li(d,{}^2He)^6He$ reaction enables one to observe an excitation range in ^6He up to 25 MeV, thereby permitting a broad search for highly excited levels. Data from this reaction have been taken at five lab angles between 17 and 40°. Figure IV-9 shows a representative ^2He energy spectrum measured at 17°. Only the g.s. transitions and a fairly weak

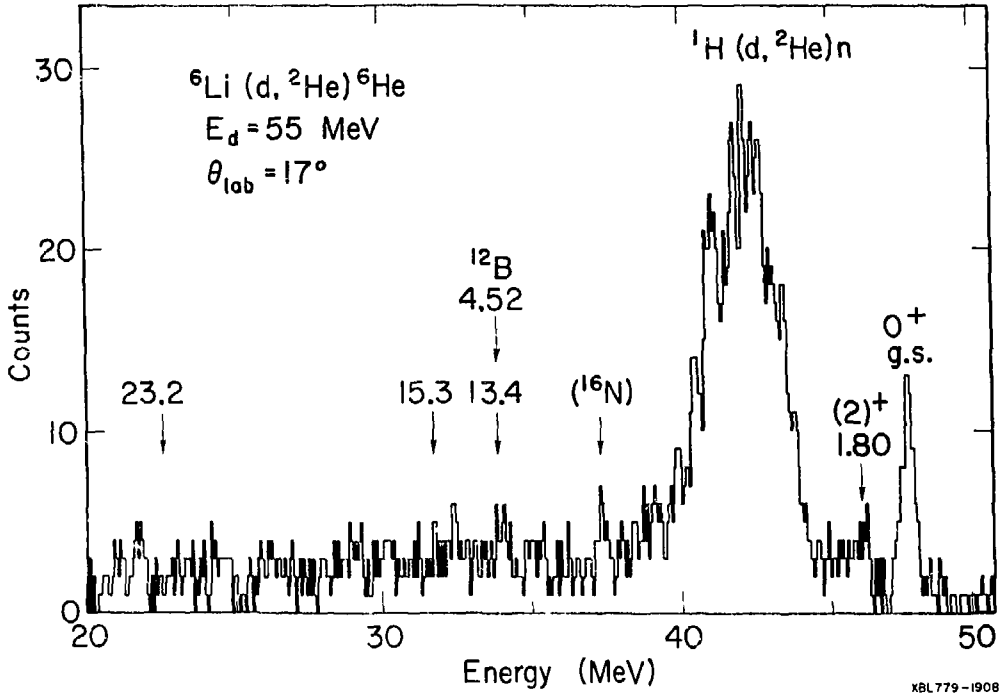

Fig. IV-19. ^{2}He energy spectrum from the ^{6}Li(d,^{2}He)^{6}He reaction at E_d = 55 MeV and θ_{lab} = 17°.

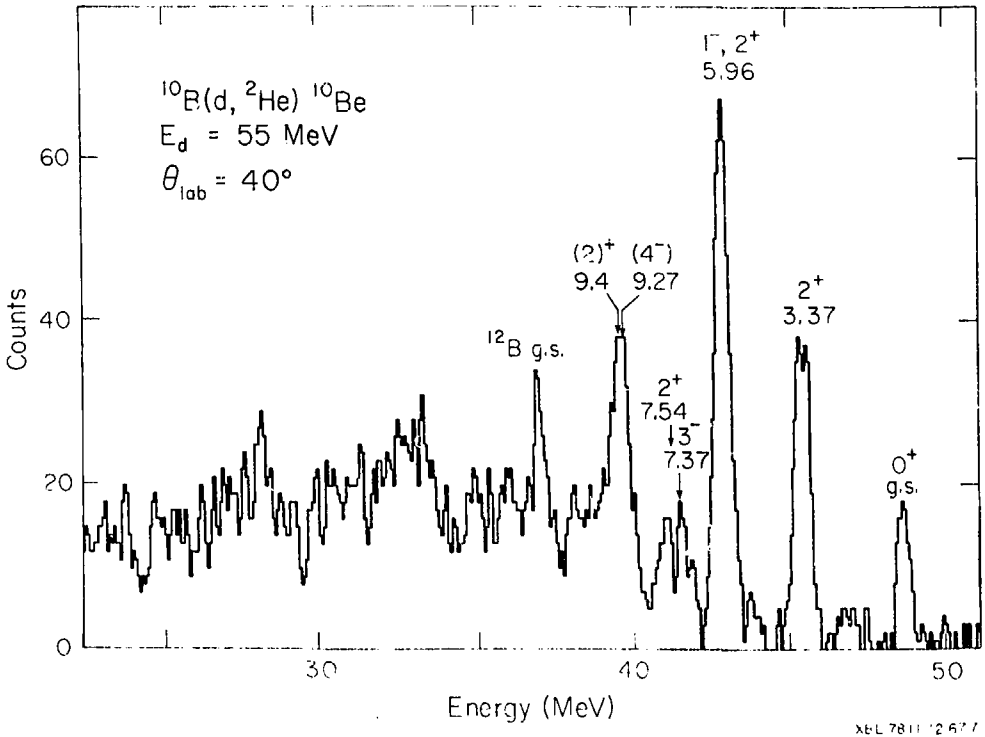

Fig. IV-20. ^{2}He energy spectrum from the $^{10}B(d,{}^2He)^{10}Be$ reaction at E_d = 55 MeV and θ_{lab} = 40°.

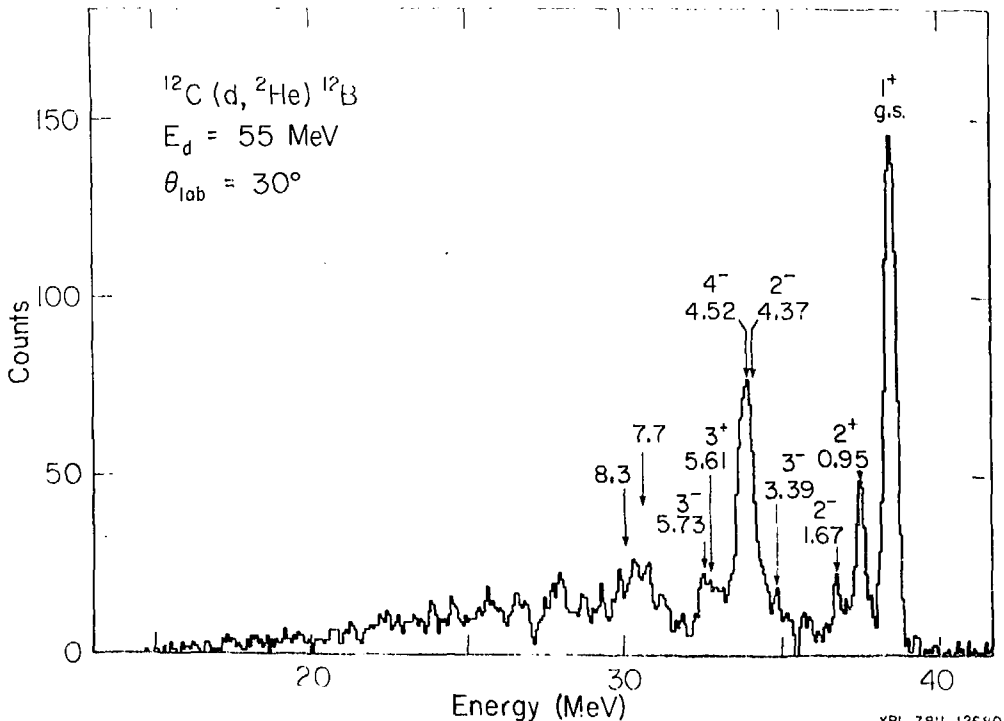

Fig. IV-21. ^{2}He energy spectrum from the $^{12}C(d,{}^{2}He)^{12}B$ reaction at E_d = 55 MeV and θ_{lab} = 30°.

transition to the 1.80 MeV state were observed. Although the large peak from the $^{1}H(d,^{2}He)n$ reaction obscures the ^{6}He excitation range from 4 to 8 MeV at this angle, at the other observed angles there is no evidence for ^{6}He levels in this excitation range. The arrows in Fig. IV-19 indicate the positions of possible transitions to ^{6}He levels which have been previously observed (Aj74) at 13.4, 15.3 and 23.2 MeV. No evidence was obtained for transitions to these states at this or other angles. Similarly to the above $(d,^{2}He)$ reaction, the (p,n) (Ba68) and $(^{3}He,t)$ (Gi72) mirror reactions on ^{6}Li only produce the g.s. and, more weakly, the 2.67-MeV, $(2)^{+}$ state of ^{6}Be with no evidence for any higher excited states.

$\underline{^{10}B(d,^{2}He)^{10}Be}$ $(Q_0 = -2.00$ MeV)

The level structure of ^{10}Be has been investigated with a variety of reactions, but no detailed study of this nucleus with a charge-exchange reaction has yet been reported. Data from the $^{10}B(d,^{2}He)^{10}Be$ reaction were obtained over a lab angular range from 17 to 50°. Figure IV-20 presents a spectrum from this reaction at 40°. Strong transitions to the g.s., 0^{+}, and to the known (Aj74) 2^{+} state at 3.37 MeV were observed. In addition, a strong peak was observed at E_x = 5.96 MeV which could be composed of a mixture of two known states, a 2^{+} state at 5.9583 MeV and a 1^{-} state at 5.9599 MeV. Based on results from investigations (An74) of the $^{9}Be(d,p)^{10}Be$ reactions, the 2^{+} state is likely to be the dominant component. Furthermore, there is some evidence for weak (and

normally unresolved) transitions to the 7.37-MeV, 3^- and 7.54-MeV, 2^+ states. The highest excitation energy in ^{10}Be at which a transition was observed was found at 9.34 ± 0.10 MeV. This peak is likely to be an unresolved doublet consisting of the 9.27-MeV, (4^-) and the 9.4-MeV, $(2)^+$ states.

Due to the lack of data from other charge exchange reactions producing ^{10}Be, the present spectra can only be compared with those from reactions populating the mirror nucleus ^{10}C; the latter results were obtained via the (p,n) reaction, which was investigated at E_p = 30 and 50 MeV (Ci70) and the (^{3}He,t) reaction, which was at $E_{^3He}$ = 30 MeV (Ma66a). In all these reactions, only the g.s., 0^+; 3.35-MeV, 2^+ state as well as a presumably 2^+ state at 7.2 MeV in ^{10}C have been observed, which are the analogs of the g.s., 0^+, 3.37-MeV, 2^+ and 5.96 MeV, 2^+ states in ^{10}Be as observed in the (d,^{2}He) reaction. Although a state at 9.34 MeV was populated with significant strength in the (d,^{2}He) reaction, its analog in ^{10}C has not yet been identified.

<u>^{12}C(d,^{2}He)^{12}B</u> (Q_0 = -14.61 MeV)

Figure IV-21 shows a ^{2}He energy spectrum from the ^{12}C(d,^{2}He)^{12}B reaction at θ_{lab} = 30°. At forward angles strong transitions were found to the g.s., 1^+ of ^{12}B. Furthermore, a strong peak was observed at E_x = 4.50 ± 0.07 MeV, which consists of unresolved transitions to known states (Aj75) at 4.52 and 4.37 MeV with J^π = 4^- and 2^-, respectively. In addition, population of the 0.95-MeV, 2^+

state was observed with moderate strength. The known states at 1.67 MeV, 2^- and 3.39 MeV, 3^- were only very weakly populated. Finally, in the spectra obtained at larger angles ($\theta_{lab} \sim 35^o$), evidence was found for a broad state at $E_x = 8.3 \pm 0.1$ MeV, which cannot be identified with any previously known state.

Similar ^{12}B spectra have been obtained in a study (Br77) of the $^{12}C(n,p)^{12}B$ reaction at $E_n = 56$ MeV. In addition to the transitions to the g.s., the 0.95 MeV state and the doublet at 4.4 MeV, a somewhat broad peak was observed at $E_x = 7.7 \pm 0.1$ MeV, particularly in the spectra taken at forward angles, with a strength comparable to that of the g.s. transition. Based on it observed energy and width, this state at 7.7 MeV is believed to be the analog of the giant dipole resonance in ^{12}C, which has also been observed in the $^{12}C(\pi^-,\gamma)^{12}B$ reaction (Bi70) at $E_x = 8.19 \pm 0.5$ MeV. It is interesting to note that this state does not significantly appear in the $(d,{}^2He)$ spectra at any angle, which seems to confirm that it is a pure L = 1, S = 0 (Goldhaber-Teller) state (Ke68). (The (n,p) reaction showed no evidence for transitions to the state observed at 8.3 MeV in the $(d,{}^2He)$ reaction).

No $(t,{}^3He)$ reaction on ^{12}C has been reported so far. The only other charge-exchange reaction on ^{12}C leading to ^{12}B was performed with the heavy ion reaction $({}^7Li,{}^7Be)$ at $E_{{}^7Li} = 52$ MeV (Ba73). Energy spectra obtained in this reaction are similar to those from the $(d,{}^2He)$ reaction, however, no states above $E_x = 6$ MeV could be observed.

The mirror nucleus ^{12}N has been the subject of several investigations with charge-exchange reactions such as the $^{12}C(p,n)^{12}N$ reaction at E_p = 30 and 50 MeV (Cl70) and the $^{12}C(^3He,t)^{12}N$ reaction at $E_{^3He}$ = 49.3 MeV (Ma76). The latter study could correlate most states in ^{12}N below 4 MeV with an analog state in ^{12}B with reasonable confidence. For the higher excited states, however, no such assignments could be made; this region does contain several candidates for states analogous to those observed in ^{12}B in the $(d,^2He)$ and (n,p) reactions, but additional experimentation is clearly necessary to make any such correlation.

b. Angular distributions, DWBA analysis

Since detailed structure calculations for the p-shell nuclei investigated herein have been done by Cohen and Kurath (Co65), it is possible to perform microscopic DWBA calculations for the $(d,^2He)$ reaction using these wave functions. For the angular distributions leading to the positive parity states of ^{10}Be and ^{12}B shown in Figs. IV-22 and 23, respectively, the DWBA calculations were carried out utilizing the Oregon State Coupled-Channel Code (StX) whose underlying formalism has been extensively discussed by Madsen (Ma75).

A characteristic feature of the $(d,^2He)$ reaction is that only the spin-isospin dependent part V_{11} $(\vec{\sigma}\cdot\vec{\sigma})(\vec{\tau}\cdot\vec{\tau})$ g(r) of the nucleon-nucleon interaction (II-43) contributes to the transitions. For the radial dependence g(r) of the potential, a Yukawa form with an inverse range of 1 fm^{-1} was used. The differential cross section is then an

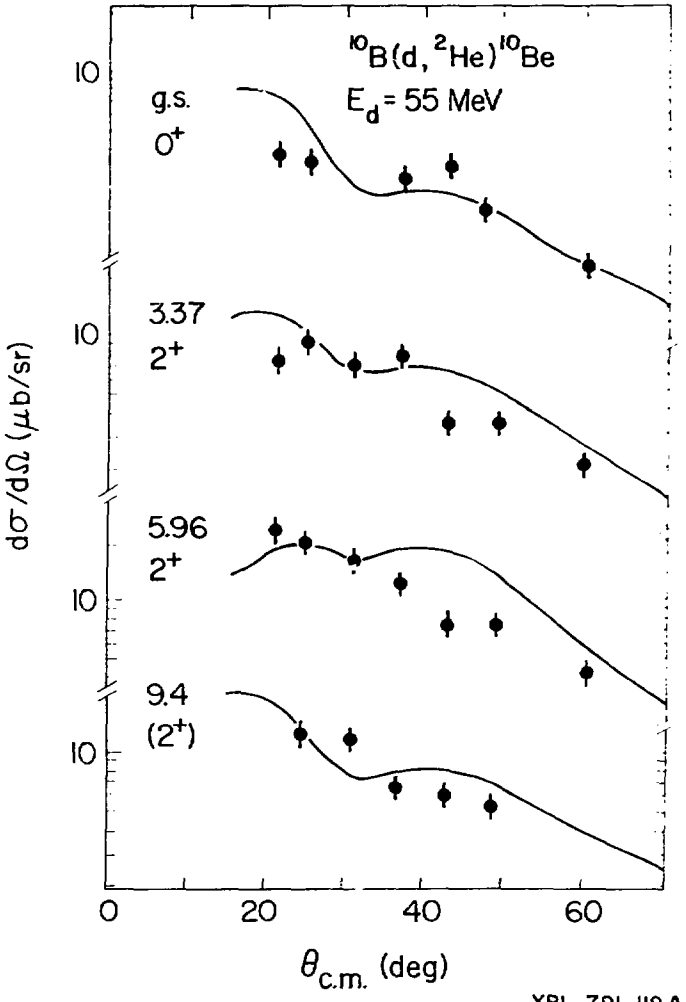

Fig. IV-22. Angular distributions from the $^{10}B(d,{}^2He)^{10}Be$ reaction at E_d = 55 MeV for $0.4 < \varepsilon < 1.0$ MeV. Statistical error bars are shown. The solid curves represent the results from microscopic DWBA calculations.

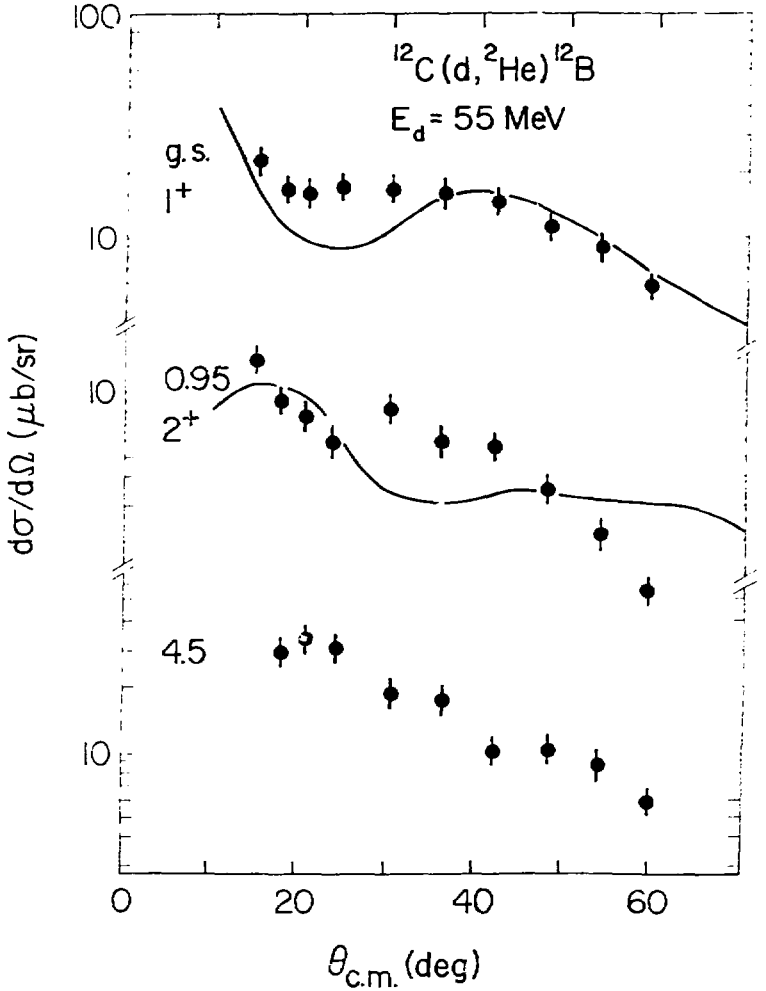

XBL 791-119 A

Fig. IV-23. Angular distributions from the $^{12}C(d,{}^{2}He)^{12}B$ reaction at E_d = 55 MeV for $0.4 < \varepsilon < 1.0$ MeV. Statistical error bars are shown. The solid curves represent the results from microscopic DWBA calculations.

incoherent sum over all allowed values of the orbital and total angular momentum transfer L and J and is given by

$$\frac{d\sigma}{d\Omega} = N\, V_{11}^2 \sum_{LJ} \sigma^{LJ}_{DWBA} \qquad \text{(IV-26)}$$

where V_{11} is the interaction strength, here taken to be 12 MeV, a typical value (Ma75) inferred from other reaction studies, and N is a normalization constant which contains all information on the projectile system such as the projectile spectroscopic amplitude and the effects of the spatial extent of the projectile on the interaction strength (We68). Furthermore, the normalization constant takes into account the fact that the experimental cross section does not comprise the entire ^{2}He g.s., but is limited to $0.4 < \varepsilon < 1.0$ MeV. Since intermediate-coupling wave functions were used for the target and residual nuclei, each term σ^{LJ}_{DWBA} in (IV-26) is a coherent sum over all possible values of the single-particle total angular-momentum quantum numbers j_1 and j_2 of the initial and final nucleus, respectively, with orbital angular-momentum quantum numbers $\ell_1 = \ell_2 = 1$. These contributions were weighted by the spectroscopic amplitudes S (II-44), which were evaluated by Kurath (Ku78) for the target nuclei ^{10}B and ^{12}C and are listed in Table IV-4.

The single-particle energies of the $p_{3/2}$ and $p_{1/2}$ neutrons and protons were assumed to be the same for the ^{10}B, ^{10}Be, ^{12}C and ^{12}B nuclei. In order to obtain values that are independent of the residual interaction, the $p_{1/2}$ single-particle energies for a neutron $E(\nu p_{1/2})$ and a proton $E(\pi p_{1/2})$ were determined from the

Table IV-4 Spectroscopic Amplitudes $S(JJ_iJ_f;101;j_1j_2)$ (Ku78)

j_2j_1		3/2	3/2		1/2	3/2	3/2	1/2	1/2	1/2
J		3	2	1	2	1	2	1	1	
J_i^π					i) A = 10, $J_i^\pi = 3^+$					
0^+	a	.4136								
2^+	a	-.5364	.4411	-.1351	.2358	.3681	-.0809	-.1390	.0236	
	b	.3414	-.1096	.2623	-.1966	.6506	.1191	.0083	-.0312	
	c	.0356	-.3775	.3797	.2308	-.0018	-.1080	.3036	.0386	
	d	-.2996	-.0581	-.0501	.3889	-.1922	-.0192	-.1513	.1323	
					ii) A = 12, $J_i^\pi = 0^+$					
1^+	a			.0539		.4881		.2399	.0412	
2^+	a		-.0429		-.4808		.0800			

binding-energy differences between $^{12}C(g.s.,0^+)$ and $^{13}C(g.s.,1/2^-)$ and between $^{12}C(g.s.,0^+)$ and $^{13}N(g.s.,1/2^-)$, respectively. The values for $E(p_{3/2})$ and $E(p_{3/2})$ were then obtained from the difference between the $p_{3/2}$ and $p_{1/2}$ single-particle energies as used by Cohen and Kurath (Co65). The bound-state wave functions were calculated in the usual way with a real Woods-Saxon well with R = 2.86 fm, a = 0.65 fm and spin-orbit potential $V_{s.o.}$ = 6 MeV. The well depth was adjusted to give the single-particle energies.

The optical model potential parameters to generate the distorted waves were taken from a study (Hi68) of elastic deuteron scattering from ^{12}C at 52 MeV. For the real part a volume Woods-Saxon potential with a well depth V = 71.8 MeV, r_V = 1.25 fm and a_V = 0.7 fm was used, whereas the absorptive imaginary part consisted of a surface Woods-Saxon potential with W = 11.0 MeV, r_W = 1.25 fm and a_W = 0.7 fm. The same parameter set was used for the entrance and exit channels.

Results from these DWBA calculations of the $(d,^2He)$ reaction on ^{10}B and ^{12}C are shown as solid curves in Figs. IV-22 and 23. Each distribution has been individually normalized to the data with the value of the normalization constant N listed in Table IV-5 along with the allowed L and J transfer quantum numbers and the label of the spectroscopic amplitudes (Table IV-4) used in the calculations.

For the $^{10}B(d,^2He)^{10}Be$ reaction, the shapes of the theoretical angular distributions are in reasonable agreement with the data. The calculated distributions to the 3.37, 5.96 and 9.4 MeV states, which were all assumed to have $J^\pi = 2^+$ and were obtained

Table IV-5 Summary of the values for the normalization constant N extracted from a DWBA analysis using the spectroscopic amplitudes listed in Table IV-4.

Reaction	E_x	J_f^{π}	L	J	N
$^{10}B(d,{}^2He)^{10}Be$	g.s.	0^+a	2	3	0.45
	3.37	2^+a	0	1	0.35
			2	1,2,3	
	5.96	2^+b	0	1	0.37
			2	1,2,3	
	9.4	2^+d	0	1	1.90
			2	1,2,3	
$^{12}C(d,{}^2He)^{12}B$	g.s.	1^+a	0,2	[illegible]	0.70
	0.95	2^+a	2	2	0.59

with the spectroscopic amplitudes 2^+a, b and d, respectively, (Table IV-4), are similar in shape except for that to the 5.96 MeV state at forward angles; this variation is probably due to different relative contributions from L = 0 and 2 transitions. With regard to the extracted value of the normalization constant N, only that for the 9.4 MeV state differs significantly from the others. Its large value could be a result of a substantial unknown contribution to the data from the unresolved 4^- state at 9.27 MeV. This is consistent with the results from studies (An74) of the $^9Be(d,p)^{10}Be$ reaction which populates the 9.27-MeV and 9.4-MeV states with comparable strength. Since the value of N for the 5.96-MeV, 2^+ state does not deviate significantly from that of the g.s. and first excited state, the contribution to the experimental cross section from the 1^- state, which lies only 16 keV higher, seems to be quite small, again in agreement with the findings of $^9Be(d,p)^{10}Be$ reaction studies (An74). Calculations were also carried out using the spectroscopic amplitudes 2^+c. They yielded a distribution similar to that of the 2^+a set but with a magnitude smaller by a factor of about 15. Since a known 2^+ state is observed with weak strength at 7.54 MeV, it is likely that the spectroscopic amplitudes 2^+c correspond to this state.

Figure IV-23 shows the results of the microscopic DWBA analysis for the $^{12}C(d,^2He)^{12}B$ reaction leading to the g.s., 1^+ and the 0.95-MeV, 2^+ state. Due to the lack of spectroscopic amplitudes, no calculations were performed for the transitions to the negative parity

states, which contain sd-shell configurations. For the g.s. transition, the shape of the calculated angular distribution is in acceptable agreement with the data. The experimental cross section is about five times larger than that of the $^{10}B(d,^{2}He)^{10}Be$ (g.s.) transition. Although the theory predicts correctly a larger value, it is by only a factor of about three. Agreement between the experimental and the calculated distributions is poorer for the pure L = 2 transition to the 0.95-MeV, 2^{+} state of ^{12}B. Whereas the experimental distribution falls off rapidly at backward angles, the DWBA calculations predict a distribution that is quite flat between $\theta_{c.m.}$ = 30° and 70°.

This successful description of the angular distributions of the $(d,^{2}He)$ reaction on targets of ^{10}B and ^{12}C indicates that the assumed direct one-step charge-exchange reaction mechanism is consistent with the data and indicates the potential usefulness of this reaction as a spectroscopic tool. However, preliminary calculations have indicated that the tensor force could be of some importance. Furthermore, exchange effects and multi-step processes such as α-^{3}He-^{2}He may have to be considered as well, before a complete understanding of the mechanism of the $(d,^{2}He)$ reaction can be obtained.

E. Reactions Producing $^{4}He^{*}$

It is well known that ^{4}He does not possess any bound excited states. Since all excited states (α^{*}) lie above the p-t threshold at E_{x} = 19.8 MeV, it is possible to detect α^{*} particles by means

of a coincidence measurement of the breakup products p and t. Using the same detection system that was employed to detect ^{2}He (Fig. III-2), p - t coincidence events can be observed with relative energies corresponding to ^{4}He excitation energies between about 20 and 25 MeV. In this region, there are three relatively well established states (Fi73), namely the 20.1, 0^+; 21.1, 0^-; and 22.1-MeV, 2^- states all with T = 0. Whereas the negative parity states, which also lie above the n-^{3}He threshold at 20.6 MeV, are broad and overlap with each other, the first 0^+ excited state is quite narrow ((Fi73) quotes Γ = 270 keV).

The fact that the 0^+ state can experimentally be resolved from the higher lying states, makes an investigation of reactions producing ^{4}He in this state (as an outgoing particle) particularly attractive. Furthermore, it is possible to quantitatively measure $\alpha^*(0^+)$ by way of detecting the breakup products p and t since this decay channel is the only important one open for its de-excitation (γ decay to the g.s. is forbidden for $0^+ \rightarrow 0^+$ transitions. The radiative width Γ_{rad} = 1.1 meV as deduced from the ^{4}He(e,e') reaction has been attributed to internal pair production (Fr68)).

Section I discusses the structure of the excited states of ^{4}He below 25 MeV. Data from the (α,α^*) reaction will be presented in Sec. 2 together with a interpretation of the reaction mechanism in terms of the direct-reaction theory. In Sec. 3, results from a measurement of the $(^3\text{He},\alpha^*)$ reaction will be given and the implications regarding the structure of the $\alpha^*(0^+)$ state will be discussed.

1. Structure of $^4He^*$ states below 25 MeV

Only three excited states below E_x = 25 MeV in ^4He have been established so far (Fi73): the 20.1-MeV, 0^+; 21.1-MeV, 0^-; and 22.1-MeV, 2^- states. The structure of the negative parity states is quite simple (De66). They belong to the configuration $(1s^{-1}1p)$ $^3P_{0,1,2}$. In contrast, the structure of the 0^+ state is more complicated. Its positive parity requires that the excitation of this state proceeds either by promotion of a single nucleon from the 1s shell to the 2s shell, which lies two shells higher, or by promotion of two 1s nucleons into the next higher lying 1p shell. The total wave function of this state is therefore composed of a 1 particle-1 hole (1p-1h) and a 2 particle-2 hole (2p-2h) component. It has long been known (El55) that the linear combination that eliminates spurious c.m. motion is

$$\psi(0^+) = \sqrt{\frac{3}{4}}\ \phi(1p\text{-}1h) + \sqrt{\frac{1}{4}}\ \phi(2p\text{-}2h) \quad . \qquad \text{(IV-27)}$$

Assuming a harmonic oscillator potential, the unperturbed energy of this state is $2\hbar\omega$, but the actual energy is lowered considerably by the residual particle-hole interaction. Using the wave function (IV-27) and $\hbar\omega$ = 16 MeV Vashakidze and Mamasakhlisov (Va67) found a value of 11.28 MeV for the residual interaction and, thus an excitation energy of 20.72 MeV which is in good agreement with the experimental value of 20.1 MeV. According to (IV-27) this state possesses 75% 1p-1h and 25% 2p-2h character. Random-phase approximation calculations with purely central (Sz70) and realistic forces (Sz72) produce

essentially the same result. However, it was found (Sz70) that calculations of the form factor of inelastic electron scattering from ^{4}He underestimate the magnitude considerably if such wave functions are used. Agreement with the data could only be obtained by lowering the 1p-1h component in the wave function from 75% to about 27%. In view of this discrepancy, is is therefore desirable to obtain further experimental data on this state.

2. The (α,α^*) reaction

A study of the (α,α^*) reaction is of particular interest since the reaction mechanism is relatively uncomplicated. No transfer of mass or charge takes place during the reaction. Inelastic scattering is the only relevant process. If the target nucleus is left in its g.s., the scattering process only involves inelastic excitation of the α particle. In the case where the target nucleus is also excited, one is dealing with the interesting case of double inelastic scattering. The (α,α^*) reaction is expected to populate the same states in the residual nucleus as the (α,α') reaction, namely preferentially the collective states. For a target nucleus with $J^\pi = 0^+$, the selection rules demand that only states with natural parity, i.e., states for which $\pi = (-1)^J$, be populated in a direct inelastic scattering process. (Population of unnatural parity states can only proceed through compound nucleus formation, spin-orbit interaction, non-simultaneous multiple-phonon excitation or direct exchange process (Ei62)). Of course, the same selection rules apply also to the spin and parity of states populated in the α particle itself. Except for

the first excited state at 20.1 MeV, 0^+, all known excited states of ^{4}He below 25 MeV possess unnatural parity and should therefore not be populated.

a. *Projected energy spectrum*

In order to determine what states in the α particle are populated in the (α,pt) reaction a projected energy spectrum $d^3\sigma/d\Omega_\alpha d\Omega_2 d\Omega_p$ was generated from the data of a measurement of the $^{12}C(\alpha,pt)^{12}C$ reaction of E_α = 65 MeV using the narrow collimator geometry C (Table III-1) and is displayed in Fig. IV-24a. It can clearly be seen that the reaction proceeds only through the 0^+ state with no evidence for transitions through the 0^- and 2^- states consistent with a direct inelastic scattering mechanism.

Since the 0^+ state is so well separated from all other excited states, it is possible to fit the shape of the spectrum with FSI calculations. There has been some speculation in the past that the 20.1-MeV, 0^+ state could be another candidate for an antibound state since it meets, like the singlet state of the di-nucleon system, the conditions for such a state (see Sec. IV.A.1): the p and t are in a relative S-state close to the threshold. However detailed phase shift analyses of Meyerhof and McElearney (Me6) and Sarit and Sergeev (Sa71) have shown that this state is best described as a Breit-Wigner type resonance.

According to the FSI theory (Sec. II.B.3), the shape of the projected spectrum should be proportional to the square of the scattering function (II-49) just as in the case of ^{2}He (Sec. IV.1.2)

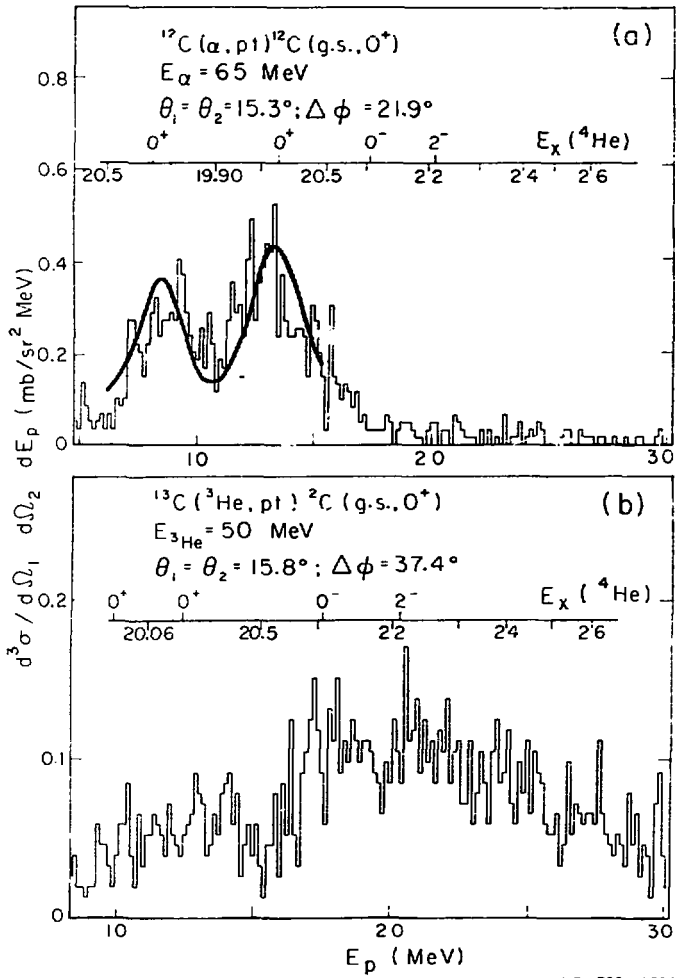

Fig. IV-24. Projected proton energy spectra from a) the $^{12}C(\alpha,pt)^{12}C(g.s.,0^+)$ reaction at E_α = 65 MeV and b) the $^{13}C(^3He,pt)^{12}C(g.s.,0^+)$ reaction at $E_{^3He}$ = 50 MeV.

however, the energy dependence of the phase shift δ_0 is not parameterized in the effective range approximation, but is derived from the R-matrix theory (La58) first given by Breit and Wigner

$$\delta_0 = \tan^{-1}\left(\frac{\Gamma_p/2}{\varepsilon_0+\Delta-\varepsilon}\right) - \tan^{-1}\left(\frac{F_0}{G_0}\right) \qquad \text{(IV-28)}$$

where Γ_p is the level width, ε_0 the resonance energy and Δ the level shift. The (energy dependent) level width is defined as

$$\Gamma_p = 2\,\gamma_p^2\,P \qquad \text{(IV-29)}$$

where γ_p^2 is the reduced proton width and the penetration factor is

$$P = \frac{ak}{(F_0^2 + G_0^2)} \qquad \text{(IV-30)}$$

where a is the channel radius. The (energy dependent) level shift which also takes into account the nearby n-^{3}He channel and thus contains a reduced neutron width γ_n^2, has been defined by Werntz (We64). Four parameters (γ_p^2, γ_n^2, ε_0, a) determine this resonance. Using a set of values from (Me65): γ_p^2 = 3.35 MeV, γ_n^2 = 1.74 MeV, ε_0 = 0.64 MeV, a = 3.3 fm the shape of the resonance was calculated for ε < 0.76 MeV and is shown as the solid curve normalized to the data in Fig. IV-24a. Other parameter sets quoted in (We62, We64, Me65) resulted in equally good fits to the data.

This projected energy spectrum and the good agreement of the FSI calculations with the data not only indicate that the $^{12}C(\alpha,pt)^{12}C$ reaction proceeds as an $(\alpha,\alpha^*(0^+))$ reaction, but also confirm the assumption (Sec. II.A.1) that there is no significant contribution to the data from other possible reaction mechanisms such as $^{12}C(\alpha,p)^{15}N^*(t)^{12}C$ and $^{12}C(\alpha,t)^{13}N^*(p)^{12}C$.

b. Energy spectrum

An α^*-energy spectrum from the reaction $^{12}C(\alpha,\alpha^*)^{12}C$ at E_α = 65 MeV is shown in Fig. IV-25. Apart from reactions leaving the target nucleus in its g.s., transitions were observed to the well-known collective states at 4.44 MeV, 2^+ and 9.64 MeV, 3^-. In addition, the 7.63-MeV, 0^+ state was weakly populated. This transition involves a monopole transition in both the projectile and the target nuclei.

c. Angular distributions, DWBA analysis

For the $^{12}C(\alpha,\alpha^*)^{12}C$ reaction at E_α = 65 MeV, angular distributions were measured over an angular range θ_{lab} = 15 to 70° and are shown for the g.s., 0^+; 4.44-MeV, 2^+; and 9.64-MeV, 3^- states in Fig. IV-26. Like the $^{12}C(\alpha,{}^2He)^{14}C$ reaction (Sec. IV.A.4.c), the differential cross sections were determined using the program SOLJAC. The distributions were then scaled to the cross section of the θ_{lab} = 15° data which was obtained by integrating the projected spectrum (Fig. IV-24a) between ε = 0.09 and 0.80 MeV.

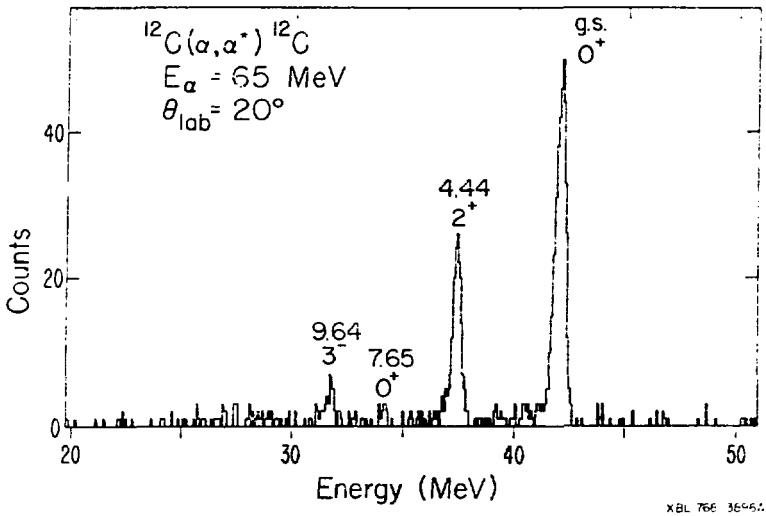

Fig. IV-25. α^* energy spectrum from the ^{12}C $(\alpha,\alpha^*(20.1,0^+))^{12}C$ reaction at E_α = 65 MeV and θ_{lab} = 20°.

The distributions of the 0^+ and 2^+ states exhibit the oscillations characteristic of elastic and inelastic scattering. It is interesting to note that as in the (α,α') reaction (Ha66) the oscillations of the distribution of the 2^+ state is out of phase with that of the g.s. transition. This is consistent with Blair's phase rule (Bl59) which states that angular distributions for scattering to states with the same (different) parity as the g.s. oscillate out of phase (in phase) with respect to the g.s. distribution. The distribution of the 3^- state which should oscillate in phase with that of the g.s. is structureless similar to the finding of (α,α') reaction studies (Ha66).

Theoretical prediction of the shape of the distributions for the transitions which only excites the α particle but not the target nucleus, is best performed in the framework of the microscopic DWBA theory of inelastic scattering (Sec. II.B.2.b). If the 20.1-MeV, 0^+ state is thought of as having a $(1s^{-1}2s)$ configuration, the reaction mechanism can be pictured as promotion of a 1s nucleon to the 2s orbit. No spin or isospin change takes place during the reaction, thus only the (non-exchange) part V_{00} of the effective interaction (II-43) contributes.

The optical-model potential parameters used in the calculations were taken from (Mo79). For the entrance channel: V = 186.1 MeV, r_V = 1.36 fm, a_V = 0.60 fm, W = 53.6 MeV, r_W = 1.20 fm, a_W = 0.71 fm, and for the exit channel; V = 145 MeV, r_V = 1.59, a_V = 0.55 fm, W = 29.5 MeV, r_W = 1.18 fm a_W = 0.5 fm. In the

usual way, a Woods-Saxon well with $R = 1.20$ fm and $a = 0.65$ fm was used to generate the initial and final bound state wave functions. The radial dependence of the interaction potential was taken to be of Yukawa form with a range of 1 fm. The result of the calculation normalized to the data is shown as dashed curve in Fig. IV-26. Excellent agreement with the experiment indicates that the assumed reaction mechanism is consistent with the data. Calculations of transitions that involve excitation of the projectile as well the target nucleus, are more complicated and cannot be performed with standard reaction programs. Some attempts have been made by Kamermans (F.79). Only poor agreement with the data was obtained and more theoretical studies are required.

3. The $(^3He, \pi^*)$ reaction

The pickup reaction $(^3He, \pi^*)$ is less selective in populating excited states in the π particle than the (π, π^*) reaction. Whereas in the latter reaction population of the 21.1-MeV, 0^- and 22.1-MeV, 2^- states is precluded, in the $(^3He, \pi^*)$ reaction these states can be populated by depositing the transferred neutron into the 1p shell.

A comparison of the $(^3He, \pi^*(0^-))$ reaction with the $(^3He, \pi)$ reaction is of particular interest. In the first reaction, the pick-up neutron is transferred into the 2s orbit, whereas in the second one the neutron goes into the 1s shell of the ^4He. Since in both reactions the final particles are in a $J^\pi = 0^+$, $T = 0$ state, identical selection rules apply. The main difference between these reactions

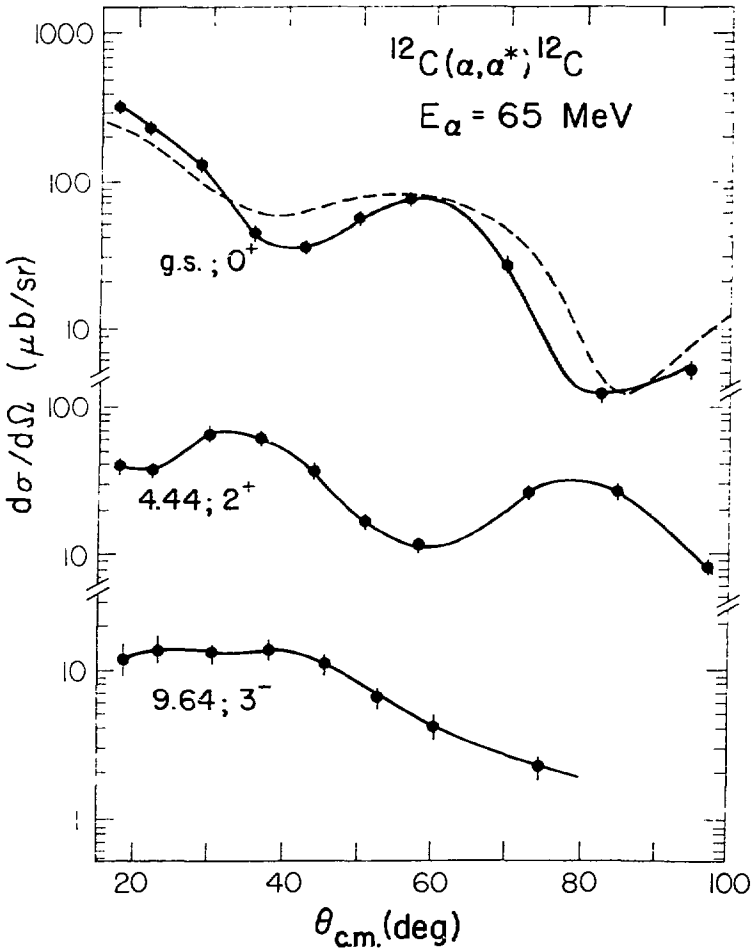

XBL 798-2741

Fig. IV-26. Angular distributions from the $^{12}C(\alpha,\alpha^*(20.1,0^+))^{12}C$ reaction at E_α = 65 MeV. Statistical error bars are shown. The solid curves are meant to guide the eye. The dashed line represents the results from a microscopic DWBA calculation.

lies in the fact that the Q values of the (^{3}He,$\alpha^*(0^+)$) reactions are about 20 MeV smaller than those of the corresponding (^{3}He,α) reactions. This should affect the relative strengths of the states populated in the residual nuclei. The structural difference between α and $\alpha^*(0^+)$ affects a given transition insofar as the absolute magnitude of the cross section is directly proportional to the single-nucleon spectroscopic factor of the α and α^* states according to (II-36). If absolute (^{3}He,$\alpha^*(0^+)$) cross sections are measured, a DWBA analysis can in principle yield a value for the spectroscopic factor S_{α^*} of the $\alpha^*(0^+)$ state. This quantity is of interest since it directly relates to the 1p-1h component in the wave function (IV-27).

a. Projected energy spectrum

Figure IV-24b shows a projected proton energy spectrum from the ^{13}C(^{3}He,pt)^{12}C(g.s.) reaction measured at $E_{^3He}$ = 50 MeV. Since in this measurement the large collimator geometry B was used, the minimum ^{4}He excitation energy that can be identified is 20.06 MeV. It is apparent that only a small fraction of the transitions goes through the first excited 0^+ state which is just separated from the peaks from the transitions through the broad and unresolved 0^- and 2^- states that constitute the main part of the cross section.

b. Energy spectra

Energy spectra were measured for the (^{3}He,α) and (^{3}He,α^*) reactions on targets of ^{9}Be (800 μg/cm^2) and ^{12}C (natural, 215 μg/cm^2) at $E_{^3He}$ = 60 MeV and on ^{13}C(80% enriched, 230

$\mu g/cm^2$) at a bombarding energy of 50 MeV and are shown in Figs. IV-27 to 29. The ($^3He,\alpha^*$) notation implies including transitions through <u>all</u> observable excited states of ^4He. Figure IV-29c presents in addition a spectrum from the $^{13}C(^3He,\alpha^*(0^+))^{12}C$ reaction alone.

All transitions observed in these spectra involve small ΔL transfers; in most cases a neutron is picked up from a p orbital. According to the angular momentum matching condition (IV-13), optimum cross section is therefore obtained for transitions with Q values such that the angular momentum mismatch ΔL (IV-12) is small. In these reactions, this conditions is met for $Q \approx 0$ MeV.

The effect of the matching conditions is clearly borne out in the spectra shown in Fig. IV-27. For the $^9Be(^3He,\alpha)^8Be$ reaction, Q_0 = 18.92 MeV which results in mismatched transitions near the g.s. of ^8Be and thus reduced cross sections. On the other hand, since Q_0 = -1.18 MeV for the ($^3He,\alpha^*$) reaction on ^9Be, the g.s. transitions are well matched and the transitions to the excited states of ^8Be are mismatched and reduced in yield.

Comparing the spectra obtained from the reactions on ^{12}C (Fig. IV-28) shows considerable similarity because $Q_0(^3He,\alpha)$ = 1.86 MeV. For the spectra from the ^{13}C target (Fig. IV-29) the same statements are true as for the ^9Be target, since $Q_0(^3He,\alpha)$ is also quite positive (15.63 MeV). Comparing Fig. IV-29b and c no difference in the relative population of states in ^{12}C can be observed in the spectra from the ($^3He,\alpha^*$) and ($^3He,\alpha^*(0^+)$) reactions.

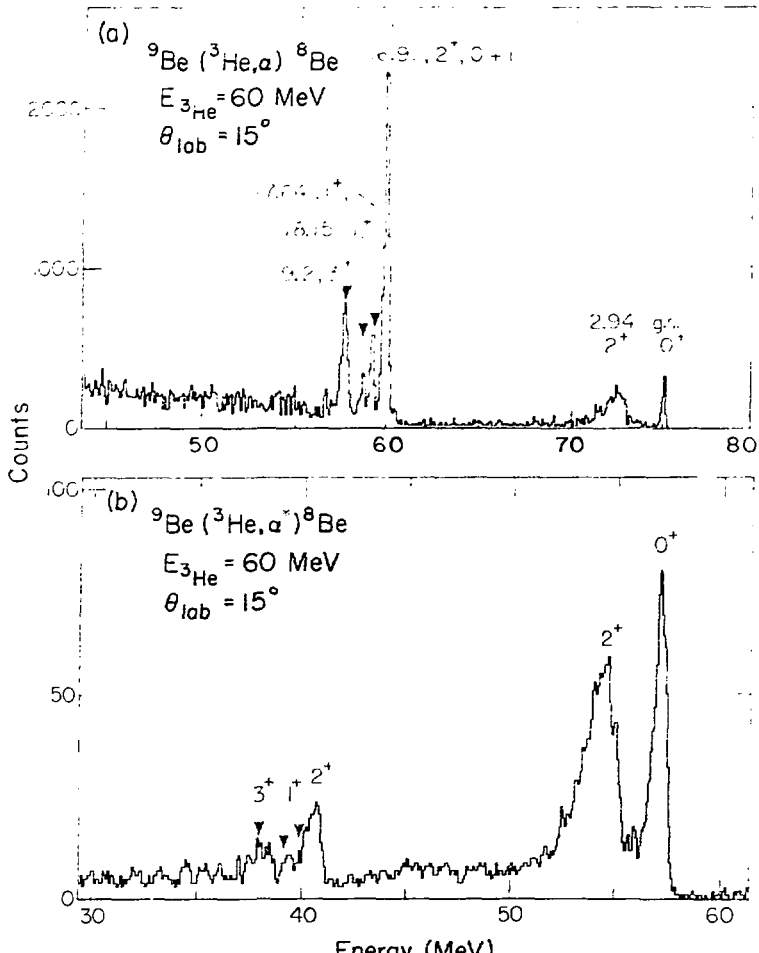

XBL 781 2349

Fig. IV-27. Energy spectra from a) the ^{9}Be(^{3}He,α)^{8}Be reaction and b) the ^{9}Be(^{3}He,α*)^{8}Be reaction at $E_{^3He}$ = 60 MeV and θ_{lab} = 15°.

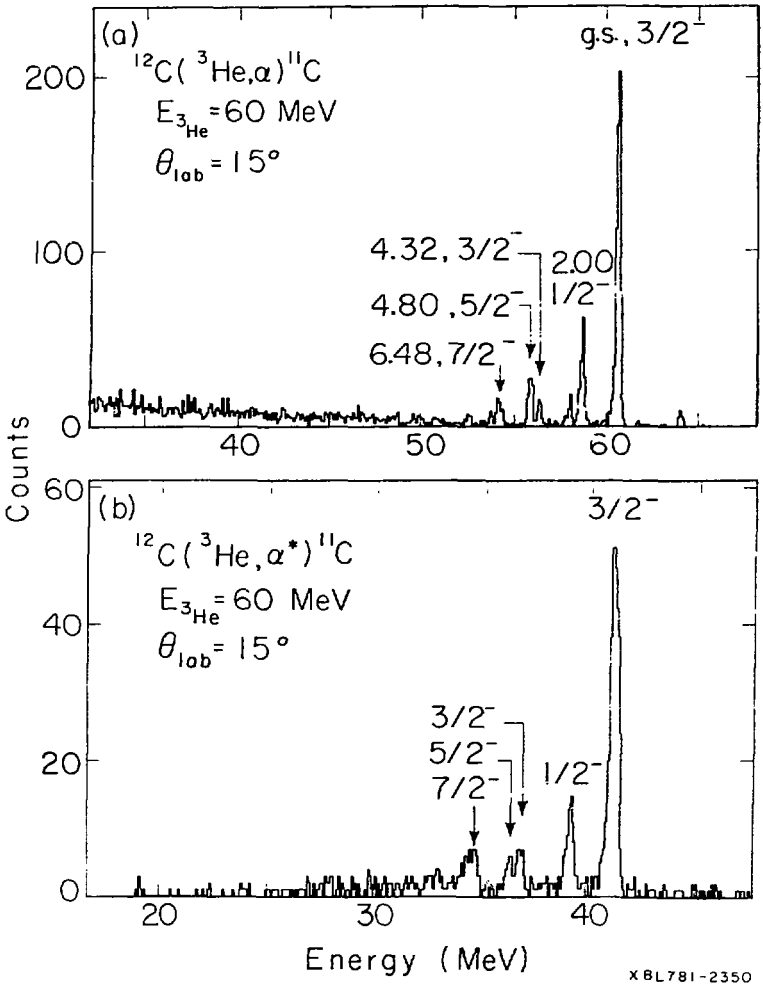

Fig. IV-28. Energy spectra from the a) (^{3}He,α) and b) (^{3}He,α*) reactions on ^{12}C at $E_{^3He}$ = 60 MeV and θ_{lab} = 15°.

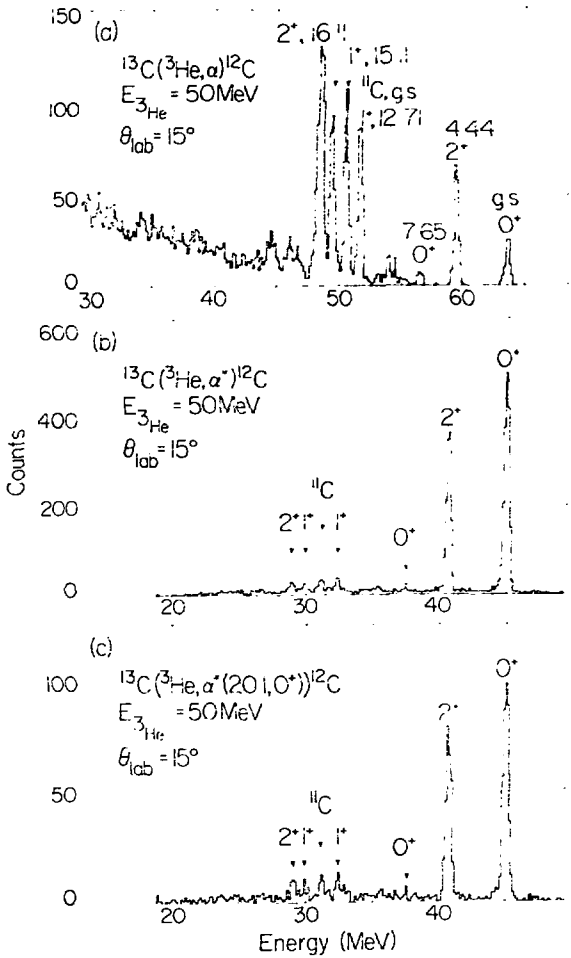

Fig. IV-29. Energy spectra from the a) (^{3}He,α), b) (^{3}He,α^*), and c) (^{3}He,α^*(20.1,0$^+$)) reactions on ^{13}C at $E_{^3He}$ = 50 MeV and θ_{lab} = 15°.

In all these spectra, the (^{3}He,α) and (^{3}He,α^*) reactions populate the same states in the residual nuclei for a given target as is expected if both reactions proceed as a direct neutron pickup process.

c. Angular distributions, DWBA analysis

Angular distributions for the (^{3}He,α) and (^{3}He,$\alpha^*(0^+)$) reactions on ^{13}C were measured at a bombarding energy of 50 MeV and are shown in Figs. IV-30 and 31. The (^{3}He,α^*) cross sections were obtained by integrating the projected proton energy spectra such as the one shown in Fig. IV-24b between ε = 0.3 and 0.8 MeV which corresponds to $E_x(^4\text{He})$ = 20.1 to 20.6 MeV. The necessary correction for the unobserved part of the data (E_x < 20.1 MeV) was obtained using the spectrum from the (α,α^*) reaction (Fig. IV-24a). This spectrum was first integrated between ε = 0.08 and 0.8 MeV and then between ε = 0.3 and 0.8 MeV. The ratio of these two cross sections then served as a correction factor. Absolute cross sections determined in this way are estimated to be accurate to about ±40%. More reliable values could be obtained from an experiment using the narrow collimator geometry C. However, the reduction of the solid angles and thus the coincidence efficiency makes such a measurement essentially unfeasible. A more practical detection system would involve a large solid angle geometry and position-sensitive detectors.

A DWBA analysis of the angular distributions from the (^{3}He,α) and (^{3}He,$\alpha^*(0^+)$) reactions has been performed in the hope to obtain spectroscopic information on the $\alpha^*(0^+)$ state. According

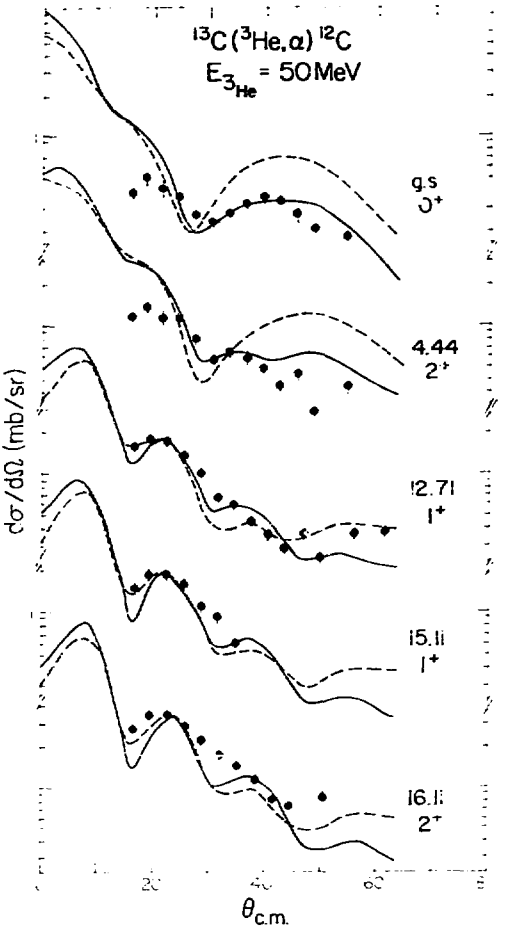

Fig. IV-30. Angular distributions from the $^{13}C(^3He,\alpha)^{12}C$ reaction at $E_{^3He}$ = 50 MeV. Statistical error bars are shown. The solid, dashed curves represent the results from ETA and ZR DWBA calculations, respectively.

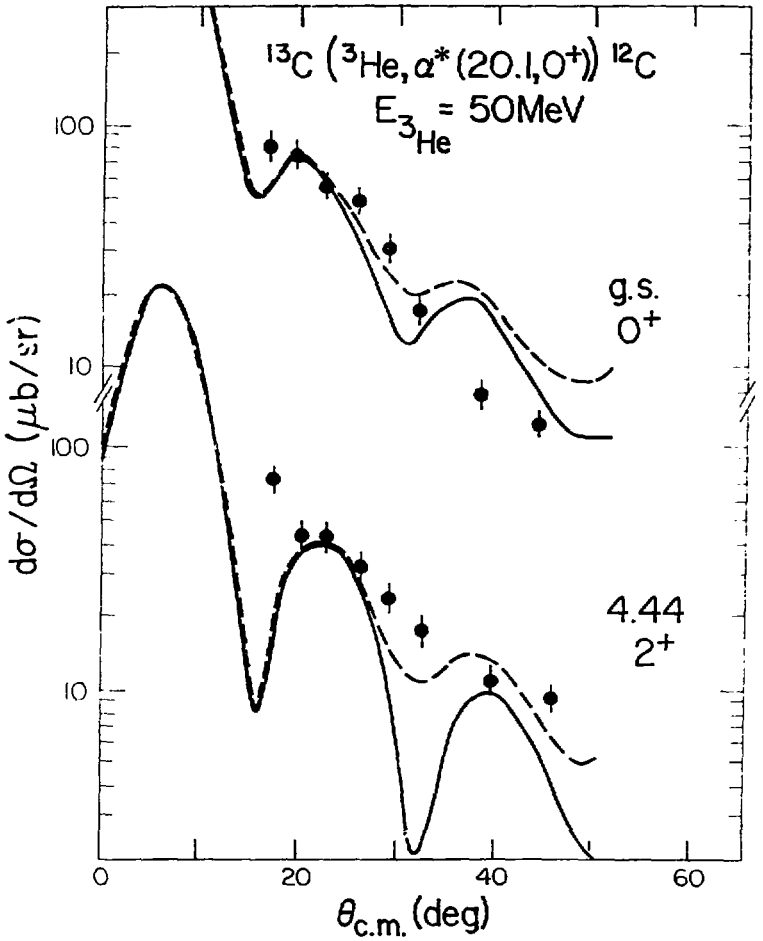

XBL-798-2740

Fig. IV-31. Angular distributions from the $^{13}C(^{3}He,\alpha^{*}(20.1,0^{+}))$ ^{12}C reaction at $E_{^3He}$ = 50 MeV. Statistical error bars are shown. The solid and dashed curves represent the results from EFR and ZR DWBA calculations, respectively.

to (II-36), in EFR DWBA the projectile spectroscopic factor S_a can be directly determined if the target spectroscopic factor S_B is known. Thus, the following procedure was chosen: first the $(^3He,\alpha)$ data were analyzed to find the absolute target S-factors S_B using a theoretical value for S_α. The extracted values of S_B served then to determine S_α^* from an analysis of the $(^3He,\alpha^*(0^+))$ data.

The EFR DWBA calculations of the $^{13}C(^3He,\alpha)^{12}C$ reaction were performed using optical model parameters for the entrance channel taken from a study of 50 MeV ^3He elastic scattering on ^{12}C (Ga69): $V = 160$ MeV, $r_V = 1.4$ fm, $a_V = 0.572$ fm, $W = 20.31$ MeV, $r_W = 1.7$ fm, $a_W = 0.537$ fm. For the exit channel, the parameters were taken from an analysis of 56 MeV α scattering on ^{12}C (Ga69): $V = 216.6$ MeV, $r_V = 1.3$ fm, $a_V = 0.58$ fm, $W = 28.05$ MeV, $r_W = 1.5$ fm, $a_W = 0.32$ fm. The target bound-state wave functions were generated with a real Woods-Saxon potential with $R = 1.25 \cdot 12^{1/3}$ fm and $a = 0.65$ fm. For the projectile bound state, a geometry $R = 1.86$ fm and $a = 0.65$ fm was used.

The results of the calculations are shown as solid lines in Fig. IV-30. (For comparison purposes, this figure also gives the results from ZR DWBA calculations which are represented by dashed lines). Each curve was individually normalized to the data with the target spectroscopic factors listed in Table IV-6 using $C^2S_\alpha = 2$ as calculated from (II-28). Also given are the S-factors obtained from a DWBA analysis of the data taken at $E_{^3He} = 60$ MeV as well as the theoretical values of Cohen and Kurath (Co65). Furthermore, relative

Table IV-6 Theoretical and experimental absolute and relative (to 12.71-MeV, 1^+ state) spectroscopic factors for five states in ^{12}C which are populated in pickup reactions.

			Theory[a]		(p,d)[b]	Experiment (^3He,d)					
						50 MeV		60 MeV		ave.	
	E_x	J^π,T	$S_{abs.}$	$S_{rel.}$	$S_{rel.}$	$S_{abs.}$	$S_{rel.}$	$S_{abs.}$	$S_{rel.}$	$S_{abs.}$	$S_{rel.}$
^{12}C	g.s	$0^+,0$	0.61	0.93	2.38	1.22	1.84	0.95	1.61	1.09	1.79
	4.44	$2^+,0$	1.12	1.70	2.88	1.28	2.03	1.15	1.95	1.22	2.00
	12.71	$1^+,0$	0.66	1.00	1.00	0.63	1.00	0.59	1.00	0.61	1.00
	15.11	$1^+,0$	0.60	0.91	0.83	0.58	1.38	0.57	0.97	0.55	1.00
	16.11	$2^+,1$	1.01	1.53	1.64	1.27	2.31	1.01	1.71	1.14	1.87

[a] (Co65)

[b] (Sc70)

experimental S-factors from an analysis of the $^{13}C(p,d)^{12}C$ reaction (Sc70) are listed in Table IV-6. All relative S-factors have been normalized to the 12.71-MeV, 1^+ state. Good agreement exists between the experimental and theoretical absolute and relative S-factors except for the g.s. and 4.44-MeV state. It seems that for these two states, the theoretically predicted values are too small. On the other hand, the experimental S-factors are somewhat uncertain; transitions in the $(^3He,\alpha)$ reaction leading to these states suffer from angular momentum mismatch which makes their calculated cross sections and particularly their absolute magnitude very sensitive to variations of the parameters that go into the DWBA.

In the DWBA analysis of the $^{13}C(^3He,\alpha^*(0^+))^{12}C$ reaction, the same optical model and bound state parameters have been employed and the results are shown as solid curves in Fig. IV-31. Whereas the experimental distributions exponentially fall off with increasing $\theta_{c.m.}$ and are structureless, the EFR as well as the ZR DWBA calculations, which are shown as dashed curves, oscillate and only reproduce the general trend of the data. This discrepancy could indicate that the reaction mechanism differs from that assumed in the present analysis.

Normalization of the calculations to the data using average experimental target S-factors (Table IV-6) yielded $C^2S_{\alpha^*} = 0.14$ for the g.s. and 0.12 for the 4.44-MeV state. Unfortunately, the uncertainty in these S-factors is quite considerable since their determination is based on $(d\sigma/d\Omega)_{exp}$, S_B, and σ_{DWBA}. The uncertainty in the

experimental cross section and the target S-factors has been discussed above. As for the theoretical cross section, it too suffers from substantial uncertainty. Although the $(^3He,\alpha^*(0^+))$ transitions are well matched, the absolute magnitude of the predicted cross section is quite sensitive to parameter variations. Considering all these uncertainties, the error on the average value $C^2S_\alpha^* = 0.13$ is at least 50%. Based on the jj coupling shell model, one finds from (II-28) a theoretical value $C^2S_\alpha^* = 0.5$ assuming a pure $(1s^{-1}2s)$ configuration. According to (IV-27), the 0^+ state has only 75% 1p-1h character which reduces the value of $C^2S_\alpha^*$ to 0.38. The experimental S-factor is thus about three times smaller than the theoretical one. This indicates that the 1p-1h component of the wave function is smaller than that assumed in (IV-27) which is consistent with the result obtained from (e,e') form factor calculations.

V. Summary and Conclusions

A detection system has been developed which is capable of measuring the unbound outgoing reaction products ^{2}He and α^* by way of detecting in coincidence the two breakup particles p + p and p + t, respectively. This system has been employed to investigate in detail the reactions (^{3}He,^{2}He), (α,^{2}He), (d,^{2}He), (α,α^*), and (^{3}He,α^*) in order to explore their potential usefulness as a spectroscopic tools as well as to obtain an understanding of the mechanism of reactions that produce unbound particles in their final states.

For the three reactions that produce ^{2}He, the (^{3}He,^{2}He), (α,^{2}He), and (d,^{2}He) reactions, projected proton energy spectra were generated in order to establish that one is dealing with ^{2}He and not just two uncorrelated protons. These spectra indeed showed the characteristic enhancement of the cross section at small relative pp energies which arises from the final-state interaction between two protons in the $^1S_0$ state of ^{2}He, and which is well reproduced by the theory of Watson and Migdal. Angular distributions from the (^{3}He,^{2}He) reaction on targets of ^{12}C and ^{13}C at an incident energy of 50 MeV were analyzed with standard DWBA calculations. Excellent agreement with the data provided further justification for treating ^{2}He as a quasi-bound nucleus. The (α,^{2}He) reaction was then studied on 16 targets between ^{12}C and ^{40}Ca at E_α = 65 and 55 MeV for its promise as potential spectroscopic tool to investigate high-spin 2n states in light nuclei. In this survey, it was found

that the $(\alpha,{}^2He)$ reaction indeed preferentially populated in p-shell nuclei states with $(d_{5/2})^2_{4^+}$ configurations and in sd-shell nuclei states with dominant configurations $(d_{3/2}f_{7/2})_{5^-}$ and $(f_{7/2})^2_{6^+}$. A linear A dependence of the binding energies of the 5^- and 6^+ states was observed which was explained by the theory of Bansal and French. A more complicated process that forms ${}^2He$ as an outgoing particle, the $(d,{}^2He)$ reaction, was measured at E_d = 55 MeV on targets of ${}^6Li$, ${}^{10}B$, and ${}^{12}C$ and compared with other charge-exchange reactions, such as the (n,p) and $(t,{}^3He)$ reactions. Whereas the latter two reactions may proceed by both non-spin-flip and spin-flip processes, the $(d,{}^2He)$ reaction is more restricted, since only spin-flip transitions are possible; the $(d,{}^2He)$ reaction is therefore a useful complement to the reactions induced by spin 1/2 projectiles. Angular distributions from the $(d,{}^2He)$ reaction were found to be in good agreement with microscopic DWBA calculations, which indicates that its mechanism is consistent with that of a direct charge-exchange process.

The detection system employed here permitted a measurement of α^* states up to E_x = 25 MeV. In this region, there are three known excited states, the 20.1-MeV, 0^+ state and the broad 21.1-MeV, 0^- and 22.1-MeV, 2^- states. In the ${}^{12}C(\alpha,\alpha^*){}^{12}C$ reaction at E_α = 65 MeV, only the natural parity state at 20.1 MeV in α^* was populated as is expected for a direct inelastic scattering process. Further evidence for an inelastic scattering mechanism was obtained from the result that both the states excited in the residual nucleus

as well as the oscillatory character of the resultant angular distributions were similar to those observed in the standard (α,α') reaction. Whereas the $(\alpha, {}^{*})$ reaction only populated the 20.1-MeV, 0^+ state in α^*, the $({}^3He,\alpha^*)$ reaction was found also to populate strongly the higher lying 0^- and 2^- states. A comparison of the energy spectra measured at $E_{{}^3He}$ = 60 MeV on targets of ^9Be, ^{12}C, [illegible], ^{13}C with those from the normal $({}^3He,\alpha)$ reaction showed that both reactions populated the same states in the residual nuclei but with different relative strengths due to the Q-value dependence of the reaction cross section. An EFR DWBA analysis of the $^{12}C({}^3He,\alpha)$ and $^{13}C({}^3He,\alpha^*(20.1,0^+))$ reactions leading to the g.s. and 4.44-MeV, 2^+ states in ^{12}C was used to extract spectroscopic information on the 20.1-MeV, 0^+ state of ^4He.

Extension of the experimental technique employed here to the detection of other unbound particles (Ro73) is straightforward. The present system can be used without modification to study reactions that produce nuclei such as $^5Li^*(16.66,\ 3/2^+) \rightarrow d + {}^3He$, $^6Li^*(2.185,\ 3^+) \rightarrow d + \alpha$ and $^7Li^*(4.633,\ 7/2^-) \rightarrow t + \alpha$. However, in order to improve the energy resolution, it would be desirable to use position-sensitive detectors that permit a reduction of the kinematic broadening without loss of coincidence efficiency.

Appendix. Solid angle computation program SOLJAC

The program SOLJAC calculates for the reaction $T(P,(1+2)^*)3$ the lab solid angle $d\Omega$ into which the unstable particle $(1+2)^*$ is emitted with a lab energy E_{1+2} before it breaks up with a fixed breakup energy into the particles 1 and 2. Their lab energies E_1 and E_2 are measured with counters whose lab solid angles are $d\Omega_1$ and $d\Omega_2$, respectively.

For particles that break up with no relative angular momentum, the c.m. cross section is according to (II-10) given by

$$\frac{d\sigma}{d\Omega_{3-12}} = \frac{4\pi}{J_{12}} \frac{d\sigma}{dE_1} \frac{d^2\sigma}{d\Omega_1 d\Omega_2} \tag{A-1}$$

where $d\ /dE_1$ is obtained by differentiating (II-7) which yields

$$\frac{d\sigma}{dE_1} = \left| \frac{1}{m_1+m_2} \left(m_2+m_1 \frac{dE_2}{dE_1} - \frac{\sqrt{m_1 m_2}\ (E_2+E_1 dE_2/dE_1)\cos\theta_{12}}{\sqrt{E_1 E_2}} \right) \right| \tag{A-2}$$

where dE_2/dE_1 is given in (Oh65).

Conversion of (A-1) to the lab system is most conveniently performed by using the fact that for large values of m_T and m_3 the values of the c.m. variables approach those of the lab variables. In the limit of $m_T \to \infty$ and thus, also $m_3 \to \infty$, the two systems become indentical:

$$\frac{d\sigma}{d\Omega} = \lim_{m_3 \to \infty} \frac{d\sigma}{d\Omega_{3-12}} \tag{A-3}$$

$$= 4\pi \frac{d^2\sigma}{d\Omega_1 d\Omega_2} \lim_{m_3 \to \infty} \frac{1}{J_{12}} \frac{d\varepsilon}{dE_1} \tag{A-4}$$

$$= 4\pi \, F \frac{d^2\sigma}{d\Omega_1 d\Omega_2} \tag{A-5}$$

where

$$F = \lim_{m_3 \to \infty} \frac{1}{J_{12}} \frac{d\varepsilon}{dE_1} \tag{A-6}$$

$$= \lim_{m_3 \to \infty} \frac{1}{J_{12}} \lim_{m_3 \to \infty} \frac{d\varepsilon}{dE_1} \quad . \tag{A-7}$$

Using (II-9) one finds

$$\lim_{m_3 \to \infty} \frac{1}{J_{12}} = \left(\frac{E_{1+2}\,\varepsilon}{E_1 E_2} \right)^{1/2} \quad . \tag{A-8}$$

Since

$$\lim_{m_3 \to \infty} \frac{dE_2}{dE_1} = -1 \tag{A-9}$$

one obtains using (A-2)

$$\lim_{m_3 \to \infty} \frac{d\varepsilon}{dE_1} = \frac{1}{m_1 + m_2} \left| \left(m_2 - m_1 - \frac{\sqrt{m_1 m_2}(E_2 - E_1) \cos\theta_{12}}{\sqrt{E_1 E_2}} \right) \right| \tag{A-10}$$

and the final result

$$F = \left| \frac{1}{m_1+m_2} \left(m_2 - m_1 - \frac{\sqrt{m_1 m_2}(E_2 - E_1) \cos \theta_{12}}{\sqrt{E_1 E_2}} \right) \cdot \left(\frac{E_{1+2}\epsilon}{E_1 E_2} \right)^{1/2} \right| \quad . \qquad \text{(A-11)}$$

The program SOLJAC first calculates F -- given values for E_{1+2}, ϵ, m_1, m_2, and counter geometry the angle separation θ_{12} between the centers of $d\Omega_1$ and $d\Omega_2$. Then, E_1 and E_2 are computed using (II-7) and

$$E_{1+2} = E_1 + E_2 - \epsilon . \qquad \text{(A-12)}$$

This requires a solution of the quadratic equation

$$a\, E_1^2 + b\, E_1 + c = 0 \qquad \text{(A-13)}$$

where

$$a = (m_2 - m_1)^2 + 4\, m_1 m_2 \cos^2\theta_{12} \qquad \text{(A-14)}$$

$$b = 2d(m_1 - m_2) - 4(E_{1+2} + \epsilon) m_1 m_2 \cos^2\theta_{12} \qquad \text{(A-15)}$$

$$c = d^2 \qquad \text{(A-16)}$$

$$d = (m_1 + m_2)\,\epsilon - m_1\,(E_{1+2} + \epsilon) \qquad \text{(A-17)}$$

The solutions of (A-13) are

$$E_1^{\cdot} = \frac{-b \pm \sqrt{b^2-4ac}}{2a} \tag{A-18}$$

and

$$E_2^{\cdot} = E_{1+2}^{+} - E_1^{\cdot} \quad . \tag{A-19}$$

Equation (A-18) possesses (real) solutions only if $b^2 \geq 4ac$. This puts a limit on the maximum possible value of θ_{12} which is determined from the condition $b^2 = 4ac$ and is given by

$$\theta_{12}^{max} = \sin^{-1}\left[\frac{m_1+m_2}{E_{1+2}^{+}} \left(\frac{E_{1+2}^{+}}{m_1 m_2}\right)^{1/2}\right] \quad . \tag{A-20}$$

For both solutions of E_1 and E_2, F is calculated and summed up provided the data contain contributions from both of them (<u>two</u> peaks in the projected energy spectrum $d^3\sigma/d\Omega_1 d\Omega_2 dE_1$). The lab cross section and solid angle are then given by

$$\frac{d\sigma}{d\Omega} = 4\pi F \frac{d^2\Omega}{d\Omega_1 d\Omega_2} \tag{A-21}$$

and

$$d\Omega = \frac{1}{4\pi F} d\Omega_1 d\Omega_2 . \tag{A-22}$$

In the case of large solid angles, $d\Omega_1$ and $d\Omega_2$ are divided into smaller ones:

$$d\Omega_1^i = d\Omega_1/m \tag{A-23}$$

$$d\Omega_2^j = d\Omega_2/n \tag{A-24}$$

For each combination ij the program determines θ_{12}^{ij}. If $\theta_{12}^{ij} \leq \theta_{12}^{max}$, $E_1^i \cdot$, $E_2^j \cdot$, and F_{ij} are calculated, otherwise $F_{ij} = 0$.
The average cross section is then

$$\frac{d\sigma}{d\Omega} = \frac{4\pi}{M^2} \sum_{i=1}^{m} \sum_{j=1}^{n} F_{ij} \frac{d^2\sigma}{d\Omega_1^i d\Omega_2^j} \quad . \tag{A-25}$$

where M is the number of combinations ij for which $\theta_{12}^{ij} \leq \theta_{12}^{max}$.
The average lab solid angle is then given by

$$d\Omega = M^2 \Big/ \left(4\pi \sum_{i=1}^{m} \sum_{j=1}^{n} F_{ij} \frac{1}{d\Omega_1^i d\Omega_2^j}\right) \quad . \tag{A-26}$$

If $m_1 = m_2$, then $d\Omega$ is multiplied by two. If the breakup energy does not have a fixed value but follows a distribution $f(\varepsilon)$ (decay from a broad state), then $d\Omega$ is calculated as a weighted average

$$d\Omega = \frac{\int f(\varepsilon)\ d\Omega(\varepsilon)\ d\varepsilon}{\int f(\varepsilon)\ d\varepsilon} \quad . \tag{A-27}$$

Acknowledgements

I would like to express may appreciation to:

My research advisor, Prof. Joseph Cerny, for his encouragement and support throughout this work;

Dr. Gordon Wozniak for introducing me to the world of unbound particles, for his help in passing my orals and his interest in all aspects of this work;

Dr. Rainer Jahn, my principal coworker, for making these experiments a success and for countless conversations;

Dr. Rob de Meijer for an inspiring collaboration and his hospitality during a visit at the KVI Groningen;

The staff members of Building 88, Dr. H. E. Conzett for teaching me the most important aspects of few-nucleon systems, and Dr. Dave Scott for numerous discussions;

Dr. Virginia Brown and Prof. Vic Madsen for helpful discussions and assistance in performing the microscopic DWBA calculations;

The post-docs and visiting staff members Drs. Nick Jelley, Dan Ashery, Gary KeKelis, Hugh Evans, Juha Äystö, Ralph von Dincklage, and Alan Shotter for their advice and expertise.

The past and present fellow graduate students Gordon Wozniak, Ken Wilcox, Bob Weisenmiller, Dave Vieira, Dennis Moltz, Brian Jeltema, Roger Parry, Jan Wouters, Alden Bice and Mike Cable;

My office mates (in chronological order) Dr. K. Yagi, Dennis Moltz, Serafina Santa Maria, Dr. Rainer Jahn, and Alden Bice, whose company made working in a window'less office much more pleasant;

Roy Burton for his help in designing much of the equipment used in this work, Jack Walton for fabricating the solid-state detectors, Claude Ellsworth for providing the targets and the cyclotron crew for good beams;

Carol Adams, our cheerful secretary, for her excellent typing and re-typing of all those manuscripts with which I had to struggle;

My family whose confidence helped me overcome the initial difficulties I encountered in this country;

Josefina for her love and her understanding that the life of a graduate student is full of sacrifices;

The Kantonale Kommission für Studienbeiträge, Zurich, for giving me the opportunity to come here.

This work was supported by the Nuclear Science Division of the U. S. Department of Energy under Contract No. W-7405-ENG-48.

(An74) R. E. Anderson et al., Nucl, Phys. A236, 77 (1974).

(An74a) N. Anjas-Weiss et al., Phys. Rep. 12C, 201 (1974).

(Aj72) F. Ajzenberg-Selove, Nucl. Phys. A190, 1 (1972).

(Aj74) F. Ajzenberg-Selove, Nucl. Phys. A227, 1 (1974).

(Aj75) F. Ajzenberg-Selove, Nucl. Phys. A248, 1 (1975).

(Aj76) F. Ajzenberg-Selove, Nucl. Phys. A268, 1 (1976).

(Aj77) F. Ajzenberg-Selove, Nucl. Phys. A281, 1 (1977).

(Au64) N. Austern et al., Phys. Rev. 133, B3 (1964).

(Au70) N. Austern, Direct Nuclear Reaction Theory, (Wiley, New York, 1970).

(Ba64) R. K. Bansal and J. B. French, Phys. Lett. 11, 145 (1964).

(Ba66) R. H. Bassel, Phys. Rev. 149, 791 (1966).

(Ba68) C. J. Batty et al., Nucl. Phys. A120, 297 (1968).

(Ba69) G. C. Ball and J. Cerny, Phys. Rev. 177, 1466 (1969).

(Ba71) I. Y. Barit and V. A. Sergeev, Yad. Fiz. 13, 1230 (1971) (Sov. J. Nucl. Phys. 13, 708 (1971)).

(Ba73) G. C. Ball et al., Phys. Rev. Lett. 31, 395 (1973).

(Be72) G. F. Bertsch, The Practitioner's Shell Model (North-Holland, Amsterdam, 1972).

(Bi70) J. A. Bistirlich et al., Phys. Rev. Lett. 25, 689 (1970).

(Bl59) J. S. Blair, Phys. Rev. 115, 928 (1959).

(Br77) F. P. Brady, Crocker Nuclear Laboratory Report No. UCD CN... 190, 55 (1977), (unpublished).

(Bu72) J. P. Burq et al., Nucl. Phys. A179, 371 (1972).

(Ce75) J. Cerny, ed., Nuclear Spectroscopy and Reactions, (Academic, New York, 1975).

(Cl70) A. S. Clough et al., Nucl. Phys. A143, 385 (1970).

(Co64) H. E. Conzett et al., Phys. Rev. Lett. 13, 625 (1964).

(Co65) S. Cohen and D. Kurath, Nucl. Phys. 73, 1 (1965).

(Cr73) D. J. Crozier et al., Phys. Lett. 46B, 169 (1973).

(Da78) S. K. Datta, G. P. A. Berg and P. A. Quin, Nucl. Phys. A312, 1 (1978).

(De66) A. de Shalit and J. D. Walecka, Phys. Rev. 147, 763 (1966).

(De73) R. M. DeVries, Phys. Rev. C 8, 951 (1973).

(De76) R. M. DelVecchio, R. T. Kouzes, and R. Sherr, Nucl. Phys. A265, 220 (1976).

(De77) R. J. de Meijer et al., Phys. Rev. C 16, 2442 (1977).

(Dr76) M. A. van Driel et al., Nucl. Phys. A272, 466 (1976).

(Ei62) W. W. Eidson and J. G. Cramer, Phys. Rev. Lett. 9, 497 (1962).

(El55) J. P. Elliott and T. H. R. Skyrme, Proc. Roy. Soc. A232, 561 (1955).

(En69) G. A. P. Engelbertink and P. W. M. Glaudemans, Nucl. Phys. A123, 225 (1969).

(En78) P. M. Endt and C. van der Leun, Nucl. Phys. A310, 1 (1978).

(Er66) F. C. Erné, Nucl. Phys. 84, 91 (1966).

(Fi73) S. Fiarman and W. E. Meyerhof, Nucl. Phys. A206, 1 (1973).

(Fl75) E. R. Flynn et al., Nucl. Phys. A246, 117 (1975).

(Fr60) J. B. French, in Nuclear Spectroscopy, Part B, ed. F. Ajzenberg-Selove, (Academic, New York, 1960).

(Fr68) R. F. Frosch et al., Nucl. Phys. A110, 657 (1968).

(Ga69) P. Gaillard et al., Nucl. Phys. A131, 353 (1969).

(Gi64) J. Gillespie, Final-State Interactions, (Holden-Day, San Francisco, 1964).

(Gi72) R. W. Givens, M. K. Brussel, and A. I. Yavin, Nucl. Phys. A187, 490 (1972).

(Go64) F. S. Goulding, D. A. Landis, J. Cerny, and R. H. Pehl, Nucl. Instrum. Methods 31, 1 (1964).

(Ha60) E. W. Hamburger and J. R. Cameron, Phys. Rev. 117, 781 (1960).

(Ha66) B. G. Harvey et al., Phys. Rev. 146, 712 (1966).

(Ha78) M. Hamm and K. Nagatani, Phys. Rev. C 17, 586 (1978).

(He67) E. M. Henley and C. E. Lacy, Phys. Rev. 160, 835 (1967).

(He69) E. M. Henley, in Isospin in Nuclear Physics, ed. D. H. Wilkinson, (North-Holland, Amsterdam, 1969) p. 15.

(Hi68) F. Hinterberger et al., Nucl. Phys. A111, 265 (1968).

(Ja70) D. F. Jackson, Nuclear Reactions, (Methuen, London, 1970).

(Ja76a) R. Jahn, G. J. Wozniak, D. P. Stahel, and J. Cerny, Phys. Rev. Lett., 37, 812 (1976).

(Ja76b) R. Jahn, D. P. Stahel, G. J. Wozniak, J. Cerny, and H. P. Morsch, Phys. Lett. 65B, 339 (1976).

(Ja76c) U. Janetzki et al., Nucl. Phys. A267, 285 (1976).

(Ja78) R. Jahn, D. P. Stahel, G. J. Wozniak, R. J. de Meijer, and J. Cerny, Phys. Rev. C 18, 9 (1978).

(Je75) N. A. Jelley, J. Cerny, D. P. Stahel, and K. H. Wilcox, Phys. Rev. C 11, 2049 (1975).

(Ka69) I. Kanestrøm and H. Koren, Nucl. Phys. A129, 527 (1969).

(Ka79) R. Kamermans et al. Nucl. Phys. A314, 37 (1979).

(Ke68) F. J. Kelly and H. Überall, Phys. Rev. 175, 1235 (1968).

(Ko76) J. Kolata et al., Phys. Rev. C 13, 1944 (1976).

(Ku66) T. T. S. Kuo and G. E. Brown, Nucl. Phys. 85, 40 (1966).

(Ku74) P. D. Kunz, DWBA Program DWUCK4, 1974 (unpublished).

(Ku78) D. Kurath, private communication (1978).

(La58) A. M. Lane and R. G. Thomas, Revs. Mod. Phys. 30, 257 (1958).

(Lu69) C. C. Lu, M. S. Zisman, and B. G. Harvey, Phys. REv. 186, 1086 (1969).

(Ma60) M. H. Macfarlane and J. B. French, Rev. Mod. Phys. 32, 567 (1960).

(Ma66) V. A. Madsen, Nucl. Phys. 80, 177 (1966).

(Ma66a) N. Mangelson et al., Nucl. Phys. 88, 137 (1966).

(Ma70) S. Maripuu and G. A. Hokken, Nucl. Phys. A141, 481 (1970).

(Ma71) C. C. Maples, LBL-253 (Ph.D. Thesis), 1971.

(Ma75) V. A. Madsen, in (Ce75), Part D, p. 249.

(Ma76) C. F. Maguire et al., Phys. Rev. C 13, 933 (1976).

(Mc55) J. N. McGruer, E. K. Warburton, and R. S. Bender, Phys. Rev. 100, 235 (1955).

(Mc70) J. S. McCarthy et al., Phys. Rev. Lett. 25, 884 (1970).

(Me65) W. E. Meyerhof and J. N. McElearney, Nucl. Phys. 74, 533 (1965).

(Me72) F. Merchez, R. Bouchez, and A. I. Yavin, Nucl. Phys. A182, 428 (1972).

(Mi55) A. B. Migdal, Zh. Eksp. Teor. Fiz. 28, 3 (1955), (Sov. Phys. JETP 1, 2 (1955)).

(Mo78) S. Mordechai et al., J. Phys. G 4, 407 (1978).

(Mo79) H. P. Morsch and P. Decowski, Phys. Lett. 82B, 1 (1979).

(Na75) H. Nann et al., Phys. Lett 60B, 32 (1975).

(Nu59) H. M. Nussenzveig, Nucl. Phys. 11, 499 (1959).

(Oh65) G. G. Ohlsen, Nucl. Instrum. Methods 37, 240 (1965).

(Ph64) R. J. N. Phillips, Nucl. Phys. 53, 650 (1964).

(Ri66) E. Rivet, R. H. Pehl, J. Cerny, and B. G. Harvey, Phys. Rev. 141, 1021 (1966).

(Ro73) D. Robson, Nucl. Phys. A204, 523 (1973).

(Sc70) D. K. Scott et al., Nucl. Phys. A141, 497 (1970).

(Sch67) J. P. Schiffer et al., Phys. Rev. 164, 1274 (1967).

(Sh74) R. Sherr, R. Kouzes, and R. DelVecchio Phys. Lett 52B, 401 (1974).

(Sl71) R. J. Slobodrian, Rep. Prog. Phys. 34, 175 (1971).

(St71) R. H. Stokes and P. G. Young, Phys. Rev. C 3, 984 (1971).

(St77) D. P. Stahel, G. J. Wozniak, M. S. Zisman, B. D. Jeltema, and J. Cerny, Phys. Rev. C 16, 1456 (1977).

(St79) D. P. Stahel, R. Jahn, G. J. Wozniak, and J. Cerny, Phys. Rev. C (in press).

(StX) M. J. Stomp, F. A. Schmittroth, and V. A. Madsen, Oregon State University, Nuclear Physics Group Technical Report (unpublished).

(Sz70) P. P. Szydlik, Phys. Rev. C 1, 146 (1970).

(Sz72) P. P. Szydlik, T. R. Borysowicz, and R. F. Wagner, Phys. Rev. C 6, 1902 (1972).

(Ta72) J. R. Taylor, Scattering Theory, (Wiley, New York, 1972).

(Tr63) W. W. True, Phys. Rev. 130, 1530 (1963).

(Va67) I. Sh. Vashakidze and V. I. Mamasakhlisov, Yad. Fiz. 6, 732 (1967), (Sov. J. Nucl. Phys. 6, 532 (1968)).

(Wa52) K. M. Watson, Phys. Rev. 88, 1163 (1952).

(We62) C. Werntz, Phys. Rev. 128, 1336 (1962).

(We64) C. Werntz, Phys. Rev. 133, B19 (1964).

(We68) J. J. Wesolowski et al., Phys. Rev. 169, 878 (1968).

(Wo76) G. J. Wozniak, D. P. Stahel, J. Cerny, and N. A. Jelley, Phys. Rev. C 14, 815 (1976).

(Za65) L. Zamick, Phys. Lett. 19, 580 (1965).